A NOVEL COMPUTER VISION-BASED FRAMEWORK FOR SUPERVISED CLASSIFICATION OF ENERGY OUTBREAK PHENOMENA

Sumaya Abusaleh

Under the Supervision of Dr. Ausif Mahmood and Dr. Khaled M. Elleithy

DISSERTATION

SUBMITTED IN PARTIAL FULFILMENT OF THE REQUIREMENTS

FOR THE DEGREE OF DOCTOR OF PHILOSOPHY IN COMPUTER SCIENCE

AND ENGINEERING

THE SCHOOL OF ENGINEERING

UNIVERSITY OF BRIDGEPORT
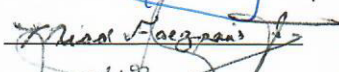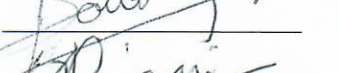
CONNECTICUT

December 2017

A NOVEL COMPUTER VISION-BASED FRAMEWORK

FOR SUPERVISED CLASSIFICATION OF ENERGY

OUTBREAK PHENOMENA

Sumaya Abusaleh

Under the Supervision of Dr. Ausif Mahmood and
Dr. Khaled M. Elleithy

Approvals

Committee Members

Name	Signature	Date
Dr. Ausif Mahmood	*Ausy Mahmood*	12/17/2017
Dr. Khaled M. Elleithy	*K.Elly*	12/17/17
Dr. Miad Faezipour	*Miad Faezpour*	12,17,2017
Dr. Sarosh Patel	*Dowo*	09/19/2018
Dr. Syed Rizvi	*Rizvi*	12/17/2017

Ph.D. Program Coordinator

Dr. Khaled M. Elleithy   *K.Elly*   1/18/18

Chairman, Computer Science and Engineering Department

Dr. Ausif Mahmood   *Ausy Mahmood*   12/17/2017

Dean, School of Engineering

Dr. Tarek M. Sobh   *T. Sobh*   1/18/2018

A NOVEL COMPUTER VISION-BASED FRAMEWORK FOR SUPERVISED CLASSIFICATION OF ENERGY OUTBREAK PHENOMENA

A NOVEL COMPUTER VISION-BASED FRAMEWORK FOR SUPERVISED CLASSIFICATION OF ENERGY OUTBREAK PHENOMENA

ABSTRACT

Today, there is a need to implement a proper design of an adequate surveillance system that detects and categorizes explosion phenomena in order to identify the explosion risk to reduce its impact through mitigation and preparedness. This dissertation introduces state-of-the-art classification of explosion phenomena through pattern recognition techniques on color images. Consequently, we present a novel taxonomy for explosion phenomena. In particular, we demonstrate different aspects of volcanic eruptions and nuclear explosions of the proposed taxonomy that include scientific formation, real examples, existing monitoring methodologies, and their limitations. In addition, we propose a novel framework designed to categorize explosion phenomena against non-explosion phenomena. Moreover, a new dataset, Volcanic and Nuclear Explosions (VNEX), was collected. The totality of VNEX is $10,654$ samples, and it includes the following patterns: pyroclastic density currents, lava fountains, lava and tephra fallout, nuclear explosions, wildfires, fireworks, and sky clouds.

In order to achieve high reliability in the proposed explosion classification framework, we propose to employ various feature extraction approaches. Thus, we calculated the intensity levels to extract the texture features. Moreover, we utilize the YC_bC_r color model to calculate the amplitude features. We also employ the Radix-2 Fast Fourier Transform to compute the frequency features. Furthermore, we use the uniform local binary patterns technique to compute the histogram features. Additionally, these discriminative features were combined into a single input vector that provides valuable insight of the images, and then fed into the following classification techniques: Euclidian distance, correlation, k-nearest neighbors, one-against-one multiclass support vector machines with different kernels, and the multilayer perceptron model. Evaluation results show the design of the proposed framework is effective and robust. Furthermore, a trade-off between the computation time and the classification rate was achieved.

DEDICATION

To all mankind, who deserve to live in peace, harmony, and to be equipped with

knowledge that will lead to the development of a better future for humanity.

ACKNOWLEDGEMENTS

In the name of Allah, the Most Gracious, the Most Merciful. Praise be to Allah who paved the way for me to complete this work successfully. Without His grace and blessings, this dissertation would not have been possible.

I am indebted to my loving family for their tremendous support, unconditional love, understanding, encouragement, and patience during my doctoral studies.

I am grateful to my dissertation adviser Professor Ausif Mahmood and co-adviser Professor Khaled Elleithy for their support, knowledge, guidance, and leadership throughout the course of my dissertation. They taught me how to overcome the challenges I faced during the progress of my work with a positive attitude.

I would like to express my appreciation to my dissertation committee members: Dr. Miad Faezipour, Dr. Sarosh Patel, and Dr. Syed Rizvi for their valuable time and feedback.

Finally, I would like to thank my friends who have made the Ph.D. chapter of my life a thrilling and unforgettable experience. They continue to always believe in me, recognize my strengths, motivate me to work with a passion to get the job done, and encourage me to never give up on my dreams.

ACRONYMS

C   Correlation

C_b Chrominance blue

CMOS   Complementary Metal-Oxide-Semiconductor

CO_2 Carbon dioxide

C_r Chrominance red

ED   Euclidean distance

EDM   Electronic Distance Meter

EMP   Electromagnetic pulse

ESB   Enterprise Service Bus

F   Fireworks

FOV   Field of View

fps   Frames per second

GIS   Geographical Information System

GPS   Global Positioning System

GUI   Graphical User Interface

HF   High frequency

IDE   Integrated Development Environment

InSAR	Interferometric Synthetic Aperture Radar
IRIS	Incorporated Research Institutions for Seismology
JPEG	Joint Photographic Experts Group
KNN	K-Nearest Neighbors
LF	Lava Fountains
LiDAR	Light Detection and Ranging
LT	Lava and tephra fallout
MODIS	Moderate Resolution Imaging Spectroradiometer
MPL	Multilayer perceptron model
MSE	Mean Square Error
NC	Nuclear explosions
PCA	Principal Component Analysis
QP	Quadratic problem
Radix-2 FFT	Radix-2 Fast Fourier Transform
RBF	Radial Basis Function
RGB	Red, Green, and Blue
SC	Sky clouds
SGD	Stochastic Gradient Descent
SMO	Sequential Minimal Optimization
SOA	Service-Oriented Architecture
SVM	Support Vector Machine
TA	Transportable Array

TIR	Thermal Infrared Radiation
TRCV	Training Combiner Vector
TTCV	Testing Combiner Vector
UAV	Unmanned Aerial Vehicles
ULBP	Uniform Local Binary Patterns
USGS	U.S. Geological Survey
VLF	Very low frequency
VNEX	Volcanic and Nuclear Explosions
Voldorad	Volcano Doppler Radar
WiFi	IEEE 802.11g/n
WF	Wildfires
Y	Luminance

TABLE OF CONTENTS

LIST OF TABLES

LIST OF FIGURES

CHAPTER 1: INRTODUCTION

Explosion phenomena today are considered a significant concern that needs to be detected and analyzed with a prompt response in order to benefit military and civilians. In this section, we explore the explosion problem and scope, and we illustrate the motivation behind this research. In addition, we outline the contributions of the proposed research.

1.1 Research Problem and Scope

This dissertation presents state-of-the-art explosion classification through pattern recognition techniques on color images including feature extraction approaches and classification techniques. Consequently, color images are taken within the visible light spectrum range of approximately 400-700nm wavelength. These processed color images are 2-dimensional arrays of pixels with each pixel having RGB components.

We define the explosion term as a rapid increase in volume, and a release of kinetic energy or potential energy. Kinetic energy includes radiant, electrical, or thermal energy, while potential energy includes nuclear or chemical energy. The explosion generates a blast pressure wave or shock wave, high temperature, release of gases, and loud sounds caused by the incidents that are associated with the occurrence of each explosion phenomena [1].

An explosion can be a natural disaster such as a volcanic eruption [2]. On the other hand, it can be a critical man-made disaster such as a nuclear explosion [3,4]. In addition, an explosion may happen when chemicals, substances, and gases are exposed to heat,

improperly stored and treated, or kept in an unstable state such as a refinery explosion, an industrial explosion, and others [5].

We present in this dissertation a novel taxonomy of the explosion phenomena with an emphasis on natural explosions (e.g. volcanic eruptions) and man-made explosions (e.g. nuclear explosions).

Consequently, we propose the design of a novel computer vision-based classification system with an associated framework for some of explosion phenomena namely: volcanic eruptions that include pyroclastic density currents, lava fountains, and lava and tephra fallout. Additionally, our framework addresses nuclear explosion phenomena that form a mushroom-shaped cloud, against some of non-explosion phenomena namely: wildfires, fireworks, and sky clouds.

Supervised learning is used to map the input frames to the desired outputs and divide the space into regions or categories. The objectives of employing feature extraction approaches and classification techniques in the proposed framework are twofold. First, we compute features which have the most relevant information that characterize explosion phenomena from the input image data that will result in reducing the computational cost. This factor is often considered as the challenge to perform the desired classification task of any application. Second, we employ multiple classification techniques to categorize those phenomena and evaluate their performance of the developed system.

In this context, we describe each image using multiple feature extraction approaches including: texture features by utilizing intensity levels, amplitude features by applying YC_bC_r color model, frequency features by exploiting Radix-2 Fast Fourier Transform (Radix-2 FFT) algorithm, and histogram features by employing Uniform Local

Binary Patterns (ULBP) technique. The Principal Component Analysis (PCA) technique is then applied on each feature class to calculate the most significant 100 eigenvectors and the corresponding eigenvalues. Furthermore, these discriminative features are collectively encapsulated into a single vector of 400 length.

In order to achieve high reliability of the explosion detection and classification system, we propose developing a system that has the following characteristics: First, an explosion event is represented by different feature sets or classes. These discriminative features computed using our proposed research methodology are invariant in terms of translation, illumination, rotation, and scale. Second, images are processed by multiple types of analysis such as texture analysis, spatial (spectral) analysis, frequency analysis, and histogram analysis. Third, our research methodology provides different views or interpretations for the same scene of an explosion or non-explosion phenomena, and finally, combining texture, amplitude, frequency, and histogram features provides a valuable insight into the images under consideration in this research.

Furthermore, these features were fed into several multiclass classification methods. As a result, the one-against-one multiclass SVM with degree 3 polynomial kernel tackled the problem at hand producing the highest classification rate. This classification model uses the Sequential Minimal Optimization (SMO) learning algorithm.

Towards the supervised classification goal, there was a need for a large dataset. However, there is a lack of public datasets on explosion phenomena under consideration in this dissertation. Therefore, we had to collect our own dataset. The new dataset includes $10,654$ samples.

In addition, satellite remote sensing instruments that are installed to monitor volcanic eruptions have limitations in terms of the transmission time. For example, the Moderate Resolution Imaging Spectroradiometer (MODIS) retrieves ash clouds images within a lengthy time frame of fifteen to thirty minutes [6]. In view of this, our proposed technical solution categorizes an explosion image in a timely manner as compared to MODIS satellite remote sensing instrument.

Table 1.1 summarizes the problems related to the classification of explosion phenomena the dissertation explores associated with the solutions the dissertation provides.

Table 1.1 Summary of problems and solutions related to explosion classification.

Problem	Solution
There is no comprehensive taxonomy for the domain of explosion phenomena.	We propose a novel taxonomy of explosion phenomena.
Explosion classification is an unsolved problem in the pattern recognition field on color images.	We propose a framework design including feature extraction approaches and classification techniques.
A proper explosion patterns' representation does not exist.	We represent an explosion event using different feature sets including texture, amplitude, frequency, and histogram features.
Selection of the suitable feature extraction methodologies.	We compute image intensity levels, YC_bC_r color model, Radix-2 Fast Fourier Transform, Uniform Local Binary Patterns, and Principal Component Analysis.
Selection of the classifier design and learning.	We apply the one-against-one multiclass SVM with degree 3 polynomial kernel. It uses the Sequential Minimal Optimization (SMO) learning algorithm.
No public dataset on explosion phenomena is available.	We collect a new dataset of color images that includes $10,654$ samples.
Lengthy time frame for detecting and transmitting explosion images using satellite systems.	We achieve a reasonable execution time using the proposed research methodology.

1.2 Motivation behind the Research

Today, the emphasis on the risk identification as the first and critical step of the risk management process is arising. Hence, the development of technology as well as science will lead to saving lives and properties when they are linked to reliable automatic early warning systems and effective evacuation procedures.

In a large explosive volcanic eruption at which a volcano vents pyroclastic flows and surges, and depending on the location of the volcanic eruption, its consequences can be experienced globally or by an entire hemisphere. Additionally, detecting an explosive volcanic eruption will lead to protecting citizens not only from primary effects of Pyroclastic Density Currents (PDCs) that are among the deadliest disasters for populations living around the volcano, but also from the secondary effects of volcanic eruptions that may trigger under proper conditions lahar, tsunami, and fires. Furthermore, locating the eruption cloud downwind is a necessity because it is crucial to aviation safety [7,8].

In addition, unlike some natural disasters such as fires, hurricanes, tsunami, earthquakes, and tornadoes where people can rebuild and repair structure in the location of the phenomenon, lava ejected from an effusive eruption buries agricultural lands, homes, and crops in its path where people are rarely able to use land buried by lava flows and fountains [9].

Moreover, installing a system to classify the event as a nuclear explosion will support military forces to gain battlefield awareness for the future as well as improve battlefield tactics.

In a broad sense, ordinary explosions [3] of the proposed taxonomy including natural gas, dust, petroleum, industrial, residential, and refinery explosions typically can cause property damage and potential loss of life. Consequently, heat and flying debris associated with these explosions may cause injuries, burns, and even death for individuals who are within the explosion radius [5]. Moreover, inhalation of smoke, chemicals, fumes, and dust resulting from an explosion cause symptoms, diagnosis, and intoxication for people. As important as it is in practice, deploying a classification system that can identify the event as an explosion at early stages will be valuable, and will play a significant role by providing rapid emergency alert not only to notify people about threats to their safety once an unexpected explosion event has occurred, but also to help community organizations and directors provide assessment for civilians and explosion victims in a minimal time.

Furthermore, because of the limitations of the current surveillance techniques for explosion phenomena [6, 10-15], the need arises for maintaining the progress of developing new technical solutions that can perform a collaborative effort with the existing monitoring systems to identify imminent explosion hazards. In this context, the motivation behind designing our classification system are fourfold. (1) Encounters diminishing of the explosion phenomena, (2) mitigation of the explosions' effect to save lives and properties, (3) defining physical properties of explosions that can be measured using RGB color

images, and (4) designing a technical solution that can detect and categorize explosion phenomena in a timely manner.

1.3 Contributions of the Proposed Research

In this dissertation, we present state-of-the-art pattern classification for explosion phenomena. As a result, this in-depth study depicts a new trend to rethink about how to cope with the challenges and constraints that govern the design, implementation, evaluation, and optimization of technical solutions for categorizing explosion phenomena using pattern recognition techniques. Contributions of this dissertations are as follows:

(1) We propose a taxonomy for the main types of explosion phenomena. Key characteristics of the taxonomy include an explosion category, classification criteria, sub-categories, and a brief description.

(2) We seek knowledge about the science behind volcanic eruptions and nuclear explosions of the proposed taxonomy in terms of how they occur through real examples. Subsequently, understanding the science has led to define different patterns of explosion phenomena from image processing point of view. Furthermore, the focus on these two categories of the proposed taxonomy among others was due to our ability of collecting images of these phenomena for conducting experiments.

(3) We collect a new dataset of color images called VNEX that includes four patterns of explosion phenomena: pyroclastic density currents, lava fountains, lava and tephra fallout, and nuclear explosions, against three patterns of non-explosion phenomena: wildfires, fireworks, and sky clouds. The totality of VNEX is $10,654$ samples. In view

of this, using a large training set, a better approximation of the features that define the patterns are obtained. Hence, the classifiers will have a high generalization capability to perform precisely on new samples. Moreover, using a large testing set will result in getting a high confidence in the anticipated error rate. In fact, the error rate of any supervised classification system is anticipated by all obtainable images that are usually divided into training and testing sets.

(4) We contribute the design and implementation of a novel computer vision-based framework for explosion phenomena using pattern recognition techniques including feature extraction approaches and classification techniques. In order to achieve high reliability in the proposed explosion classification system, we calculated the intensity levels to extract the texture features. Moreover, we utilize the YC_bC_r color model to calculate the amplitude features. We also employ the Radix-2 Fast Fourier Transform to compute the frequency features. Furthermore, we use the uniform local binary patterns technique to compute the histogram features. Then, principle component analysis algorithm is applied on each feature class to calculate the most 100 significant eigenvectors and eigenvalues. These features were combined into a single input vector that provides valuable insight of the images, and then fed into several classification techniques.

(5) We evaluate the effectiveness of the proposed features extraction methodology on the target application domain and provide a comparison between numerous multiclass classification techniques in terms of the classification rate. These methods are Euclidean distance, correlation, K-Nearest Neighbors (KNN), the multilayer perceptron model (MPL), and the one-against-one approach for multiclass Support

Vector Machines (SVMs) with various kernels including: linear, polynomials of different degrees, Radial Basis Function (RBF), and sigmoid.

(6) We assess our proposed methodology on three different testing sets. The first is the testing samples of VNEX dataset that includes $5,327$ color images. The second testing set consists of 980 frames of video sequences that we downloaded from the YouTube website, where each class comprises 140 frames that were retrieved by the system from computer folders for evaluation. These videos were taken in real outdoor environments for the seven scenarios of the respective defined classes. The third testing set consist of 980 frames of the same YouTube video sequences. However, in this case the frames were captured using a drone in a real-time indoor environment, because we do not have access to explosion zones.

(7) We calculate the classified versus misclassified samples of the testing sets under evaluation, confusion matrices of classifiers that produced the highest accuracy, and the execution time for testing an input image using our research methodology.

CHAPTER 2: EXPLOSION TAXONOMY

After exploring the domain of explosion phenomena, we propose to introduce a comprehensive novel taxonomy that includes main types of explosion phenomena. Consequently, the explosion problem domain includes the following main categories and subcategories: (1) volcanic eruptions that can be either explosive or effusive eruptions [2]; (2) nuclear explosions that have five sub-categories as follows: high altitude nuclear explosion (outer space detonation), atmospheric nuclear explosion (air burst), surface nuclear explosion, deep underground nuclear explosion, and shallow underwater nuclear explosion [4]; (3) dust explosions [16]; (4) natural gas explosions [5]; (5) petroleum explosions that can be either pipeline explosions or tank explosions [5]; (6) industrial explosions that include four subcategories as follows: chemical explosions, pipeline explosions, plant explosions, and warehouse fires [5]; (7) residential gas explosions that include the following three sub-categories: boiler and furnace explosions, appliance explosions, and wiring explosions [5]; and (8) refinery explosions [5,17].

Figure 2.1 represents the proposed explosion taxonomy, and Table 2.1 illustrates the details of the proposed taxonomy that include an explosion category, classification criteria, sub-categories, and a brief description.

This dissertation will only focus through the experiments on identifying and classifying the volcanic eruptions (natural explosions) and nuclear explosions (man-made explosions) because of the lack of images of other explosions categories of the proposed taxonomy.
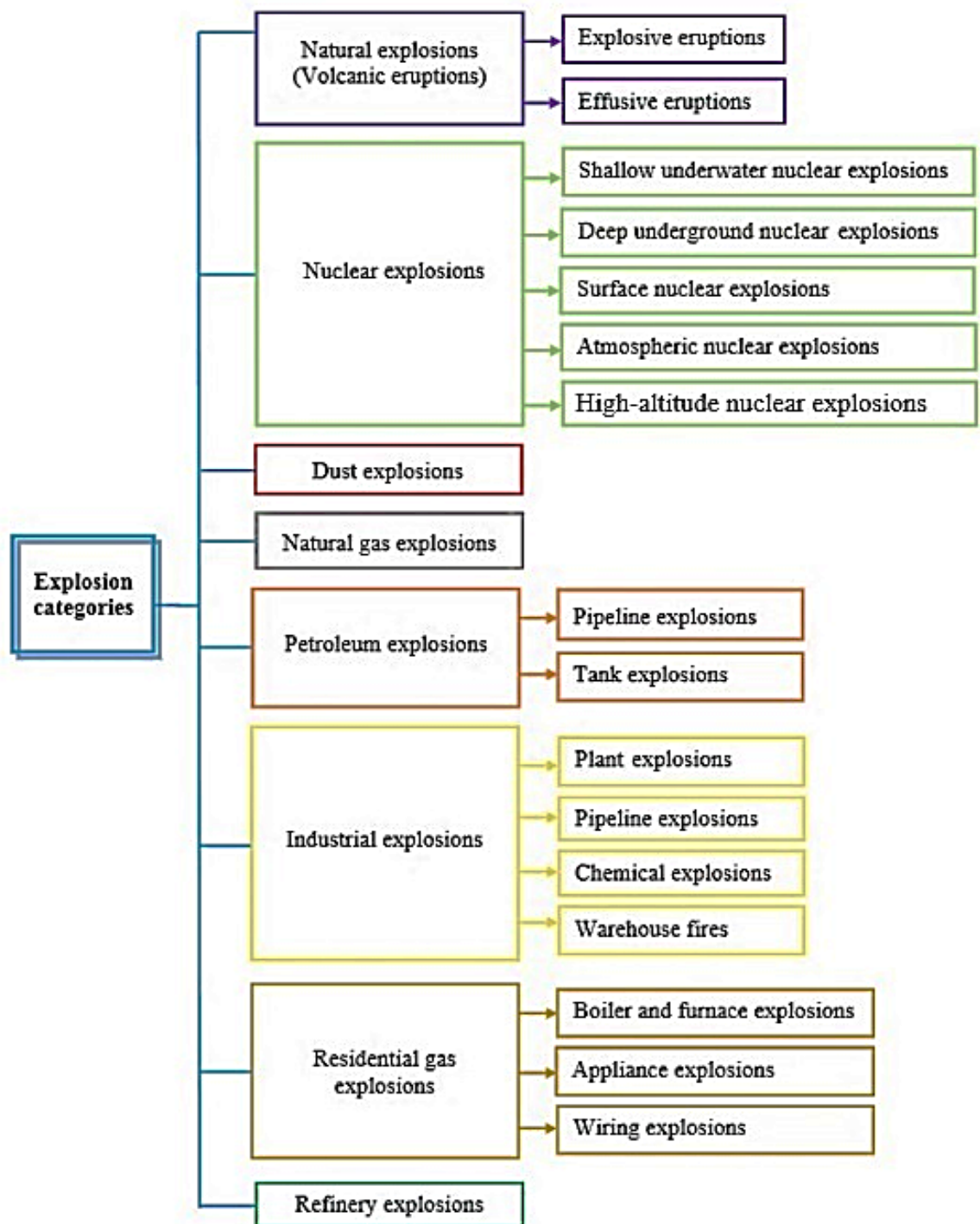
Figure 2.1 Proposed explosion taxonomy.

Table 2.1 Classification criteria of the proposed taxonomy.

Explosion category	Classification criteria	Sub-categories	Brief description
Volcanic eruptions	Explosive style	Explosive (violent)	The eruption produces pyroclastic density currents that are typically the most dangerous of all volcanic phenomena [2].
		Effusive (quiet)	The eruption generates lava fountains and flows that steadily ejected from the volcano onto the ground [2].
Nuclear explosions	Location of the point of burst in relation to ground zero	Shallow underwater	The nuclear explosion is conducted under the surface of the water [4].
		Deep underground	The nuclear weapons are detonated at varying depths under the Earth's surface [4].
		Surface	A surface explosion occurs either at the actual surface of the land or water, or slightly above [4].
		Atmospheric (air burst)	A nuclear weapon is detonated in the air/ atmosphere using balloons, towers, barges, or dropped from an airplane at an altitude below 100,000 feet, and above the Earth's surface at a height where the fireball, at its maximum growth, does not touch the surface of the Earth [4].
		High-altitude (outer space)	A nuclear explosion takes place above altitudes of 30 km (100,000 feet) [4].
Natural gas explosions	Energy resource	N/A	Gas is typically pumped out of the ground directly into a central processing unit, then processed into different gases, transported to destinations, and distributed to retail centers and homes. Throughout this long process, a devastating explosion may occur due to a variety of reasons including: (1) leaks as a result of broken seals, loose valves, and improperly maintained pipes, (2) dangerous transportation, (3) manufacturing error, and (4) dangerous storage [5].
Dust explosions	Dispersion of powdered combustible materials	N/A	Explosion occurs by five factors including: (1) oxygen, (2) heat, (3) fuel (dust), (4) sufficient quantity and concentration of the dust particles' dispersion, and (5) confinement. The resultant pressure rises and it could generate an explosion. Further, dust that may explode include: (1) natural organic materials (e.g. sugar, coal, and grains), (2) synthetic organic material (e.g. plastic, and pesticides), (3) metals (e.g. zinc, aluminum, and iron), and (4) any unstable oxide [16].
Petroleum explosions	Energy resource based on the mean of transport from the source of drilling.	Pipeline	Crude oil is transported over long distances to processing plants via pipelines once it is pumped from the ground. Failure to inspect and maintain these pipelines will result in an explosion. Petroleum contains a large amount of paraffin wax that may build up and cause lack of oil flow, and this may increase the pressure in the pipeline. If the pipeline bursts near a spark or a flame, an explosion will occur [5].
		Tank	Petroleum is stored in tanks before and after it is processed. There are several faults that may cause a petroleum tank to explode including: (1) leaks, (2) dangerous transportation, (3) poor maintenance/installation, and (4) manufacturing defect [5].

Industrial explosions	Manufacturing task	Chemical	Chemical explosions may occur because of the following actions regardless of the safety measures in place: (1) dangerous chemical reactions, (2) smoking near dangerous chemicals, (3) improperly maintained boilers, and (4) equipment malfunction [5].
		Pipeline	Pipelines transport liquid and gases from the plant for hundreds of miles. Usually, pipes do not come in lengths long enough to cover the entire distance needed. Therefore, they are made from segments. Explosions occur because of multiple main reasons including: (1) owners' negligence to have pipelines inspected to ensure the softy of plant workers, and (2) faults which include: weak welds, excessive pressure, improper construction, and faults in the seams where the segments are connected. Theses faults may allow combustible substances to leak, that in turn may come into contact with a spark and cause the substance to explode [5].
		Plant	Plant explosions may occur because of some reasons such as: (1) if heavy machinery was not well-maintained and expected, (2) failure to utilize reasonable care in handling combustible substances, (3) faulty electrical systems, (4) unsafe work conditions, and (5) chemical spills [5].
		Warehouse	Most industrial plants utilize warehouses to store chemicals and materials necessary to carry out their functions. Warehouse fires lead to explosions, and they occur because of negligent actions which include: (1) smoking near flammable liquids, (2) carelessly transporting potentially combustible substances, and (3) stacking reactive substances close together [5].
Residential gas explosions	Utility that provides a residential service	Boiler and furnace	Explosions occur because of matter's out of the homeowner's control which include: (1) installation errors, (2) design defects, and (3) maintenance errors [5].
		Appliance	Explosions happen because of the following causes: (1) poorly designed or manufactured, (2) improperly maintained and repaired, and (3) improperly installed [5].
		Wiring	Homes are equipped with a network of wires to transfer electricity into homes from the power grid. If faulty wiring come into contact with natural gas, an explosion will happen [5].
Refinery explosions	Production facility for crude oil	N/A	Large quantities of flammable gases can be produced during several cases including: (1) undetected leaks in the operating equipment, (2) from upset conditions in the normal refinery operations, (3) from startups and emergency shutdowns, and (4) during scheduled maintenance activities of the refinery. Today, the flaring safety technique is being required for the control of gaseous combustible emission from refinery sources. However, the flare system itself can present an explosion potential of a flare [5,17].

CHAPTER 3: THE ART OF READING EXPLOSION VERSUS NON-EXPLOSION PHENOMENA

In this section, we present the science behind the volcanic eruptions (natural explosions) and nuclear explosions (man-made explosions) in terms of how they normally occur. In this context, we describe different physical properties of these phenomena that, in turn, have led to interpret the patterns of color images from image processing point of view. Consequently, color images are taken within the visible light spectrum range of approximately 400-700nm wavelength. These processed color images are 2-dimensional arrays of pixels with each pixel having RGB components.

3.1 Volcanic Eruptions

A volcano is a spectacular event in the life of the Earth, and it is proof that the Earth is alive, active, and ever-changing. Thus, it is the Earth's natural mechanism of cooling off and releasing internal pressure and heat, which in turn causes rocks to melt and produce magma that is allowed to escape from the magma chamber through a vent in the Earth's crust. Therefore, as magma moves up, it loses dissolved gas and bubbles form in it. This is a driving force behind eruptions [2,18,19].

The violence of volcanic eruptions is controlled by two factors including silica content and gas content. As the silica content of magma is increases, the magma gets more viscous and it becomes stickier. Consequently, the stickier the magma is, the more viscous the magma, and the more violent the generated eruption will be, and it becomes more

difficult for the gas to escape from magma that is highly viscous. The gas content of the magma is the second factor. Hence, the more gas, the more violent the eruption will be, while the less gas, the less violent the eruption will be [2].

Based on the eruptive style of the volcano and materials ejected during the eruption, three patterns types of a volcanic eruption scene can be defined including: (1) patterns of pyroclastic density currents, (2) patterns of lava fountains, and (3) patterns of lava and tephra fallout. Consequently, the description of each phenomenon is given as follows:

3.1.1 Patterns of Pyroclastic Density Currents

Pyroclastic Density Currents (PDCs) phenomena are usually the most destructive and deadly of all types of volcanic phenomena [8]. PDCs are mixtures of hot gases associated with pyroclastic materials that flow over the ground under the effect of gravity. The PDC phenomenon may generate from different mechanisms [1, 20-24]. For example, gravitational collapse of domes (Figure 3.1a) [25], partial column collapse (Figure 3.1b) [26], dome explosions (Figure 3.1c) [27], overpressure at the vent (Figure 3.1d) [28], steam-driven eruption column (Figure 3.1e) [29], lateral blast (Figure 3.1f) [30], boiling-over (Figure 3.1g) [31], and continuous column collapse (Figure 3.1h) [31].

Furthermore, the PDC phenomenon can be either a short-lived or relatively long-lived. The short-lived PDC is considered highly unsteady phenomenon, whereas the relatively long-lived PDC is considered sustained unsteady to quasi-steady phenomenon. The duration of both the transient current (short-lived) and sustained current (long-lived) rely on the volumetric flow rate as well as the total flow volume, influencing the behavior

of the PDCs phenomena [22]. Figure 3.1a-f represent mechanisms of short-lived PDCs. In contrast, Figure 3.1g and Figure 3.1h represent mechanisms of long-lived PDCs.

From image processing point of view, PDCs patterns have color property that can be white (e.g., Figure 3.1e), or brown/brownish (e.g., Figure 3.1d), or dark colors ranging from gray to black shades (e.g., Figures 3.1f, g), have non-luminous dense cloud shapes, and have multiple manifestation (shapes) including: vertical column, laterally spread, avalanches that are generated by lava dome and moving downslope of the volcano, and some volcanic eruptions can produce natural mushroom clouds under the gravity force.

(a)   (b)   (c)   (d)

(e)   (f)   (g)   (h)
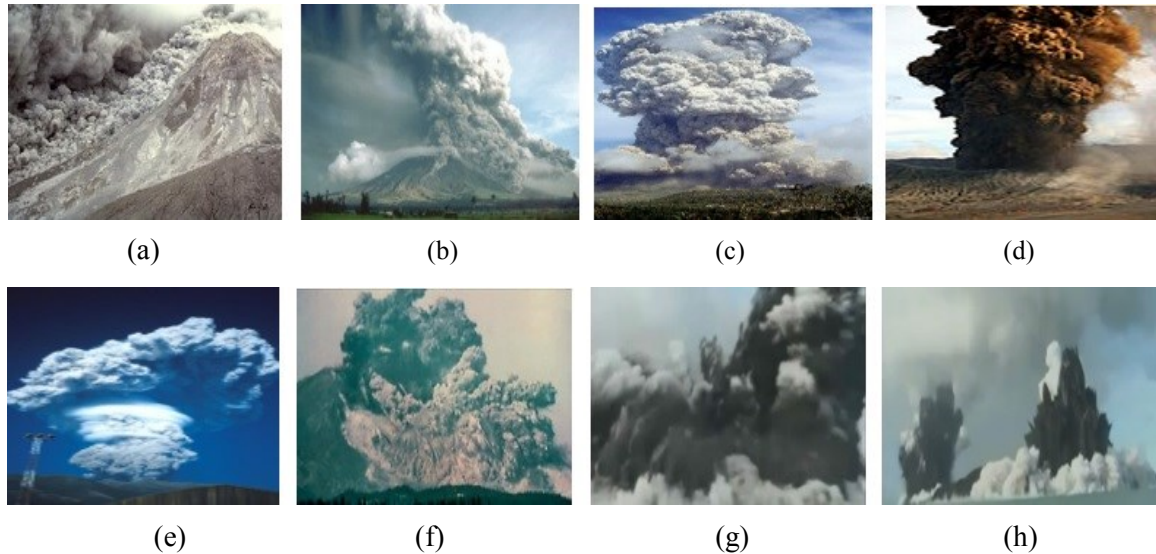
Figure 3.1 Patterns of PDCs. (a) The volcanic eruption of Soufriere Hills in Montserrat occurred on January 16, 1997 (photo credit: Richard Heard, Montserrat Volcano Observatory) [25]; (b) Mayon volcano occurred on September 23, 1984 (photo credit: Nicolas Lardot, Wikimedia Commons website) [26]; (c) Soufriere Hills volcano, Montserrat (photo credit: Barry Voight, National Science Foundation website - date of the image is unknown) [27]; (d) Bromo volcano, East Java, Indonesia, occurred on 8 June, 2004 (photo credit: D. Wijayanto, Tom Pfeiffer/ www.VolcanoDiscovery.com) [28]; (e) The eruption of Guagua Pichincha volcano, west of the capital Quito, Ecuador occurred on October 7, 1999 (photo credit: U.S. Geological Survey, Department of the Interior) [29]; (f) Mt. St. Helens volcano, Washington State, USA, occurred on May 18, 1980 (photo credit: U.S. Geological Survey, Department of the Interior) [30]; (g) The Tonga undersea volcanic eruption occurred on March 18, 2009 (photo credit: YouTube website) [31]; (h) The photo description and credit as per Figure 3.1g [31].

3.1.2 Patterns of Lava Fountains

Effusive eruptions such as shield volcanoes and fissure volcanoes produce lava that is magma rises towards the surface of the Earth, and flows out of the volcano as a viscous liquid. Typically, lava fountains and flows are varied and have multiple physical properties including [32]: (1) thickness, (2) length, (3) shape, and (4) width which depends on the following factors: lava type that is being erupted, discharge, slope of the ground where the lava travels, and the eruption duration. For example, Figure 3.2a shows Kamoamoa eruption in Kilauea, Hawaii, on March 5, 2011 [33], and Figure 3.2b displays the Kilauea's East Rift Zone (Puʻu ʻŌʻō) eruption on September 1983 [34].

<div align="center">(a)   (b)</div>

Figure 3.2 Patterns of lava fountains. (a) Fissure volcano: Kamoamoa eruption, Kilauea, Hawaii, on March 5, 2011 [33] (photo credit: U.S. Geological Survey, Department of the Interior); (b) The outpouring of lava fountains from the active shield volcano of Kilauea's East Rift Zone (Puʻu ʻŌʻō) on September 1983 (photo credit: U.S. Geological Survey, Department of the Interior) [34].

Lava fountains patterns have two properties from image processing point of view. First, a luminous glowing region. Second, the color of the lava during the eruption [1]. Accordingly, the color of the lava is based on its temperature. For example, it is stated in [35] that lava may glow white at approximately 1150 ºC, golden yellow when its

temperature nearly 1090 ºC, orange at about 900 ºC, bright cherry red at almost 700 ºC, dull red when its temperature around 600 ºC, or has the lowest visible red color at approximately 475 ºC. As a matter of fact, the hotter the object, the brighter the light emitted will be. This process is called incandescence where the heat energy is turning into light energy.

3.1.3 Patterns of Lava and Tephra Fallout

During an explosive or effusive eruption, a pattern can be formed when both the lava and tephra fallout are emitted directly from a volcano [1]. Tephra can be defined as a generic phrase for the accumulation of any airborne pyroclastic materials, for instance, fine ash, coarse ash, lapilli (cinders), Pele's hair, Pele's tears, blocks, bombs, and others. These materials are different in terms of type, size, shape, and condition when ejected from a volcanic vent [36].

Furthermore, Figure 3.3a depicts a volcanic fissure at which lava fountains of 100-400m high and massive billowing volcanic ash clouds expelled near the Montagnola summit on July 24, 2001 [37]. Figure 3.3b represents lava and tephra fallout generated from the Eruption of Pu'u 'Ö'ö, Kilauea, Hawaii, in 1984. Tephra fallout, in this example, is a combination of cinder, Pele's hair, and Pele's tears [38]. Figure 3.3c demonstrates lava and tephra fallout generated from the explosive eruption of Eyjafjallajökull in the island of Iceland that occurred on April 14, 2010 [39]. Figure 3.3d illustrates the effusive eruption (basaltic volcanism) of Mt. Etna, Sicily, Italy which occurred in November 2002 [40].

(a)   (b)   (c)   (d)
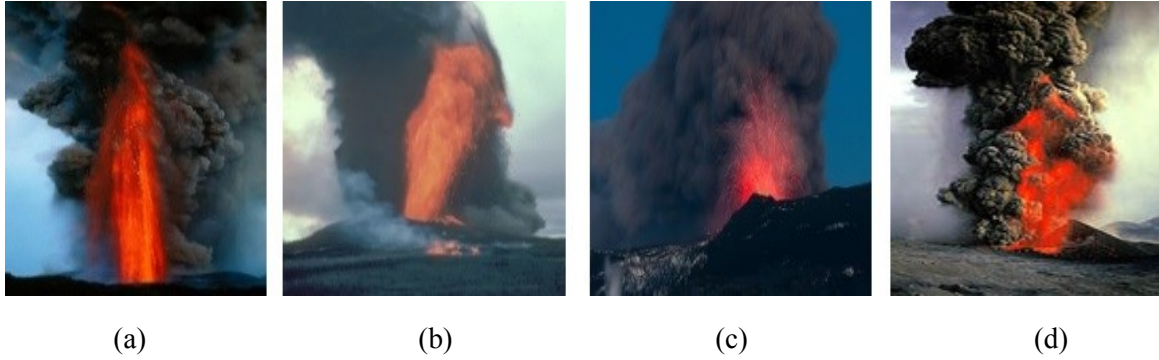
Figure 3.3 Patterns of lava and tephra fallout. (a) Lava fountains and massive billowing volcanic ash clouds expelled near the Montagnola summit of Etna volcano which occurred on July 24, 2001 (photo credit: Tom Pfeiffer/ www.VolcanoDiscovery.com) [37]; (b) lava and tephra fallout generated from the Puʻu ʻŌʻō eruption, Kilauea, Hawaii, in 1984 (photo credit: U.S. Geological Survey, Department of the Interior) [38]; (c) Explosive eruption of Eyjafjallajökull in the island of Iceland occurred on April 14, 2010 (photo credit: David Karnå, Wikimedia Commons website) [39]; (d) Effusive eruption (basaltic volcanism) of Mt. Etna, Sicily, Italy, occurred in November 2002 (photo credit: Tom Pfeiffer/ www.VolcanoDiscovery.com) [40].

From image processing point of view, lava and tephra patterns have the following properties. (1) A luminous glowing region that represents the lava, (2) a non-luminous region that represents the tephra fallout, (3) the color of the lava that relates to its temperature, and (4) the color of the tephra that depends on the pyroclastic materials types that are being emitted during an explosive or effusive eruption [1]. For example, the tephra fallout can be either dark colored pyroclastic of basaltic to andesitic scoria or light colored pyroclastic of felsic pumice and ash [41].

3.2 Nuclear Explosions

A nuclear explosion is defined as an explosion for which the energy is released by a nuclear transformation, either by fission or fusion [4]. Typically, nuclear explosions are classified based on the location of the point of burst in relation to ground zero [1]. Hence,

nuclear explosions have the following five subcategories. (1) high altitude nuclear explosion (outer space detonation), (2) atmospheric nuclear explosion (air burst), (3) surface nuclear explosion, (4) deep underground nuclear explosion, and (5) shallow underwater nuclear explosion. In contrast, we propose to classify nuclear explosions based on the shape characteristic from image processing point of view. Thus, we define two patterns. (1) a mushroom-shaped cloud that is typically formed by the following types of nuclear explosions: atmospheric, surface, deep underground, and shallow underwater, and (2) an artificial aurora view associated with an ionized region that is formed by the space (high-altitude) explosion. A brief description behind the scientific formation of both nuclear explosion patterns is given in this section.

3.2.1 Patterns of Mushroom-Shaped Clouds

The formation of a nuclear mushroom-shaped cloud can be described through an example of a shallow underwater explosion, the Baker test that was conducted at Bikini Lagoon in 1946 [42]. At the beginning of the explosion, the water near the explosion was illuminated by the fireball formation. However, the water waves caused distortion on the surface of the lagoon that prevented a clear view of the fireball. The hot gas bubble underwater initiates a shock wave. Intersection of the shock wave with the surface produces a slick that is a ring of darkened water that is rapidly expanding, while the reflection of the water shock wave at the surface causes a crack. A crack is a white circular patch behind the dark region. Then, a spray dome (a column of broken water and spray) is thrown up over the point of burst. The sides of the spray dome become steeper when the water rises.

20

The disturbance created by the underwater burst causes a series of waves to move outward from the center of the explosion across the surface of the lagoon, where the test was conducted. The water flowed into the cavity as the pressure of the bubble was released that caused the water to be thrown up as a hollow cylinder, or chimney of spray, called the "column/plume." The radioactive contents of the bubble were vented through the hollow column and formed a cauliflower-shaped cloud at the top in a shallow underwater explosion that concealed part of the upper portion of the column. The cloud contained some of the fission products, weapon residues, and a large amount of water in droplet form [42]. Figure 3.4 depicts the mushroom-shaped cloud of the underwater Baker nuclear explosion [43].

Figure 3.4 Mushroom-shaped cloud of the underwater Baker nuclear explosion in 1946 (photo courtesy of National Nuclear Security Administration/ Nevada Field Office) [43].

From image processing viewpoint, nuclear explosions patterns have the following five properties. First, the color property where the initial color of the mushroom cloud of a nuclear expulsion is red/reddish. When the fireball cools, water condensation leads to the white color characteristic of the explosion cloud [4], and secondly, growth of the nuclear mushroom-shaped cloud, where it keeps rising until it reaches its maximum height. Third, the shape which can be either mushroom-shaped cloud, or artificial aurora display with ionized region in case of space explosions. Fourth, the luminous region of the image at which a luminous fireball can be viewed as flash or light from hundreds of miles away for about 10s, and then it is no longer luminous. Thus, the non-luminous growing cloud appears for approximately 1−14 minutes, and fifth, the orientation where the mushroom-shaped cloud has a single orientation.

3.2.2 Patterns of the Artificial Aurora Display with an Ionized Region

The display of the artificial aurora with an ionized region is due to the effect of the electromagnetic pulse (EMP) of the high-altitude nuclear explosion from outer space. EMP effect can be described as follows [4]: a photon has an energy of several million electron volts that is a typical energy for gamma radiation emitted by a high-altitude nuclear explosion. When photons interact with atoms of the air in the atmosphere (nitrogen and oxygen), large parts of its energy will be transferred to the electrons on atoms. As a result of this collision process, gamma rays have reduced energy, while the electrons have accelerated and are thus stripped from atoms, producing an extensive ionized region called

a "deposition region" where the electron currents are formed. This is known as the Compton Effect. A charged particle (electrons) in the magnetic field of the Earth will describe a circular motion. In order to maintain a circular motion or helical path, the electrons must continually accelerate inward toward the circle's center. The acceleration is due to the continual charge in the direction of the electron velocity, and it produces electromagnetic radiation known as synchrotron radiation. These effects make up an EMP. However, this representation is not possible for other kinds of explosion phenomena. Figure 3.5 represents the artificial aurora with deposition region formed by Starfish space explosion in 1962 [44].

Figure 3.5 Starfish artificial aurora with deposition region as seen from an aircraft in 1962 (photo credit: Gregory Walker, Trinity Atomic Web Site) [44].

This dissertation will only focus through the experiments on identifying and classifying the nuclear explosions that form the mushroom-shaped cloud because of the lack of images of the high-altitude explosions.

3.3 Non-Explosion Phenomena

In this section, we propose to define three patterns of non-explosion phenomena from image processing point of view against the aforementioned patterns of explosion phenomena that were defined in sections 3.1 and 3.2. Consequently, non-explosion patterns include: wildfires, fireworks, and sky clouds. The aim of adding these patterns to the framework is to evaluate the reliability and the robustness of the strategy adopted in this dissertation.

3.3.1 Patterns of Wildfires

Wildfires patterns from image processing point of view contain a non-luminous region, a luminous region, or both. The luminous region that usually appears in the scene of a wildfire is related to the flame that is produced during the flaming phase of the combustion process, and its color variation depends on the type of the material being burned, how hot it's burning, and the amount of oxygen that is available to turn all the carbon into Carbon dioxide (CO_2). The flame color of the wildfires typically glows red transmitting to orange, then to yellow. On the other hand, the non-luminous region of a wildfire scene is related to the smoke that is generated during the smoldering phase of the combustion process. This smoke tends to reflect the light making the smoke appears white. Likewise, tree trunks and big branches may have large amounts of moisture that are prone to smolder and emit steam that turns the smoke white. In addition, a black soot of fine particles is formed and released into the air during the hot burning of the dry underbrush. Thus, the smoke may appear black in a wildfire scene [1,45].

3.3.2 Patterns of Fireworks

Fireworks patterns from image processing point of view have the following properties. First, a black background because they are typically displayed in the night. Second, they have multiple ignitable shapes such as: glitter, spinner, tail, willow, brocade, stars, and others. Third, they have different colors that are related to the type of the metal salt which produces a light that travels at a specific wavelength [46-48].

3.3.3 Patterns of Sky Clouds

Clouds patterns from image processing point of view have different shapes. For example, high-level clouds include Cirrus that have wispy and feathery shape, Cirrostratus have relatively transparent form of a widespread veil-like layer, and Cirrocumulus that are layered clouds performed with small cumuliform lumpiness, and have rippled shapes, whereas mid-level clouds include Altostratus that possess a flat and uniform type texture, Altocumulus that are heap-like clouds, and Nimbostratus that have dark, thick, and lumpy layer. Furthermore, low-level clouds include Stratus that are dull gray clouds that developed horizontally, and Cumulus that are the stereotypical fluffy clouds that developed vertically, Stratocumulus that are small lumpy clouds, and Cumulonimbus that are tall and fluffy. In addition, color of the clouds is the second property. When all different colors of light hit a water droplet or ice crystal of the cloud that has an average size of about 10 micrometers. They scatter equally into colors of rainbow; then they combine to produce a white light. Hence, clouds typically appear white [49,50].

CHAPTER 4: LITERATURE SURVEY

In this section, we explore existing literature that addresses various approaches for detection and categorization of nuclear explosions and volcanic eruptions. Moreover, we provide examples of the current programs for monitoring these phenomena in the United States. In addition, we highlight the limitations of the existing surveillance systems for explosions.

4.1 Existing Literature on Monitoring Volcanic Eruptions and Nuclear Explosions

Roth and Guritz [51] developed a system to predict and to display volcanic ash cloud movements utilizing meteorological data and eruption parameters for input. The model can predict the volcanic ash particle density in the atmosphere as a time function. Eruption parameters for the model include: the volcano's geographical location, time, the eruption duration, the plume's altitude, the particle density, and the distribution of the particle density.

Ando [52] conducted experiments to remove the interfering signals of temperature and pressure from the output of continuously running spring gravity meters. Hence, more accurate results can be achieved using high sensitive instruments in a harsh environment to monitor an active volcano such as the Mt. Etna volcano located in Italy. Furthermore, Ando monitored the physical behavior of lava flow by measuring two components of the cooling process of lava flow that included conductive and radiant heat transfers.

Nugroho and Winarko [53] built a conceptual surveillance system for volcanic eruptions by integrating the Geographical Information System (GIS) and the concept of Service-Oriented Architecture (SOA) using Enterprise Service Bus software (ESB). This system may improve the job performance of geologists and volcanologists when volcanoes occur in order to mitigate the volcanoes' impact.

Werner-Allen *et al.* [54] deployed a small wireless sensor array for three days at the Tungurahua volcano in Ecuador in 2004. Three Mica2 motes equipped with microphones were installed to detect infrasonic signals (low frequency acoustic) that were produced from the erupting volcano. In addition, an event detector was developed to trigger the transmission of data automatically as soon as multiple nodes received a well-correlated signal. This technique was evaluated based on bandwidth usage, reduced energy, and detection accuracy of infrasonic signals.

Likewise, Werner-Allen *et al.* [55] deployed a sensor network of 16 nodes for 19 days on the Reventador volcano in Ecuador. Moteiv TMote Sky platform of the wireless sensor network was used. Each node was equipped with a seismometer and a microphone to gather seismic and acoustic data of the volcanic eruption activity. Data were transmitted through a multi-hop path to a gateway node which, in turn, is connected to a long-distance FreeWave modem that provides a radio connectivity with a laptop. Additionally, a GPS receiver was used for time synchronization.

Tan *et al.* [56] proposed a real-time quality-driven technique to detect volcanic earthquakes. Two sensing algorithms were developed: (1) the Bayesian detection approach that used the joint statistical model of the seismic signal energy as well as the frequency spectrum, and (2) a sensor selection algorithm. Furthermore, a two-phase earthquake onset

time estimation technique was developed. Lastly, these algorithms were implemented on a 24 TelosB motes testbed, and then experiments were conducted based on traces of real data gathered for five and a half months from the Mt. St. Helens volcano, which contained over 128 important earthquake events.

In addition to the wireless sensor-based techniques used to detect seismic and acoustic data of volcanic eruptions, several computer vision-based techniques were used to monitor volcanic eruptions. In this view, Jinguuji and Ehara [57] proposed a remote sensing system by employing satellite images to compute the volcanic ash. This system is based on a physical model of volcanic ash motion. The model was tested on the Kuju volcanic eruption in Japan that occurred in 1995.

In the Lawrence Livermore National Laboratory [58], researchers presented the use of radar images taken from satellites that used the InSAR technique to monitor the Earth's surface from space. Researchers analyze these images to detect very small subsurface changes caused by underground nuclear explosions, and volcanic hazards. In addition, these researchers run simulations to characterize deformations.

Andò and Pecora [59] presented a new measurement tool that performed a real-time automatic thermographic analysis that used frames acquired by a thermal camera for volcanic activities of Mt. Etna and Stromboli in Italy. After the processing of a frame sequence, various information was provided that includes: the typology of the eruption, aspect, aspect ratio, maximum height, maximum width, and the duration of the analyzed sequence.

Langer et al. [60] classified volcanic tremor data at Mt. Etna in Italy based on supervised and unsupervised pattern classification techniques. Supervised classification

was applied on an image dataset of four target categories namely: post-eruptive, eruptive, pre-eruptive, and lava fountain (effusive eruption). The totality of their dataset was 425 samples. Furthermore, the power feature was measured in frequency intervals, then a multilayer perceptron technique (MPL) and support vector machine approach (SVM) were employed for classification. During the testing scheme, the output label was either '1' for the class, or '0' for all other classes. The SVM achieved an accuracy of 94.8%, and the MLP achieved an accuracy of 81.9%. On the other hand, unsupervised categorization was attained by employing self-organizing maps and cluster analysis approaches.

Iyer *et al.* [61] introduced a detection system for volcanic eruptions based on infrasonic signals. These signals contain information regarding the volcano's intensity that provides an approximation of ash column height. Consequently, unique cepstral-based features were extracted from the infrasonic signature of the volcano, and then fed into a radial basis function neural network to distinguish eruptive activity among these three volcanoes including: Kasatochi located in Alaska, Tungurahua located in Ecuador, and Mt. St. Helens located in USA. Consequently, a total number of $25,356$ infrasonic data was obtained from the global infrasonic monitoring network dataset, and the waveform of each class was divided into 20 segments. Volcanic eruptions, based on the height of the ash column, were classified into the following classes: Strombolian, Vulcanian, Subplinian, and Plinian. As a result, a classification rate of 97% was achieved.

Also, Picchiani *et al.* [62] employed a single layer neural network to classify ash, or non-ash, and to retrieve the ash mass. Moreover, five datasets of MODIS images in the TIR spectral range were gathered in the 2001, 2002, and 2006 from the Mt. Etna volcanic eruptions. Each dataset includes $810,000$ samples. The architecture of the neural network

included: the input space of three MODIS channels: CH28, CH31, and CH32, as well as a single hidden layer, and a single output layer. Results showed that approximately 90% accuracy was achieved.

Additionally, Marzano *et al.* [63] utilized a ground-based microwave weather radar system to perform the detection (dynamical monitoring) of a volcanic ash cloud, a quantitative retrieval of a volcanic ash cloud, concentration, and fall rate. The quantitative information was based on three classes: lapilli, coarse ash, and fine ash. As a result, in Plinian and sub-Plinian volcanic eruptions cases, ash particles can be characterized through modeling results and experimental results.

Similarly, Boccia *et al.* [64] introduced a ground-based remote sensing system for volcanoes using the L-band microstrip array. The developed antenna is part of the Volcano Doppler Radar (Voldorad). The system retrieves the mass data and the velocity. The proposed array configuration was designed via shortened rectangular patch antennas (microstrip radiators with improved directivity). Hence, the Voldorad antenna was integrated with the radar for the remote sensing of the summit eruptions of Mt. Etna [64].

Aside from the discussion of volcanic eruptions monitoring found in the literature, several researchers studied many techniques to monitor nuclear explosions.

Dickinson and Tamarkin [15] explored several approaches to retrieve detection, location, and time information about nuclear explosions that are conducted in the atmosphere and in space (high-altitude). These approaches include: (1) acoustic; (2) debris sampling; (3) radio flash or electromagnetic pulse (EMP); (4) satellites which use instruments to measure radiation from a nuclear detonation, such as X-rays, gamma-rays, and neutrons; (5) atmospheric fluorescence; (6) radio techniques that include: very low

frequency (VLF), low frequency (LF), high frequency (HF), radio sounders, cosmic noise (Riometer); (7) magnetic telluric; and (8) sunlight resonance scatter from debris.

Additionally, Lindgen [65] provided criteria on how to identify and detect seismic waves of underground nuclear explosions versus earthquakes.

4.2 Programs for Monitoring Volcanic Eruptions and Nuclear Explosions in the U.S.

Current literature addresses how the U.S. Geological Survey (USGS) monitors volcanic eruption phenomena [10, 66-69]. Figure 4.1 depicts the volcanic monitoring techniques that are employed by the USGS Volcano Hazards Program as follows: (1) detecting volcanic tremor (harmonic tremor); (2) hydrologic monitoring; (3) gas emission; (4) temperature measurements using thermocouples, Thermal Infrared Radiation (TIR) video cameras, and infrared satellite sensors; (5) satellite remote sensing such as Moderate Resolution Imaging Spectroradiometer (MODIS); and (6) monitoring volcano ground deformation by using: Electronic Distance Meter (EDM), Tiltmeter, Global Positioning System (GPS), and Interferometric Synthetic Aperture Radar (InSAR) images.
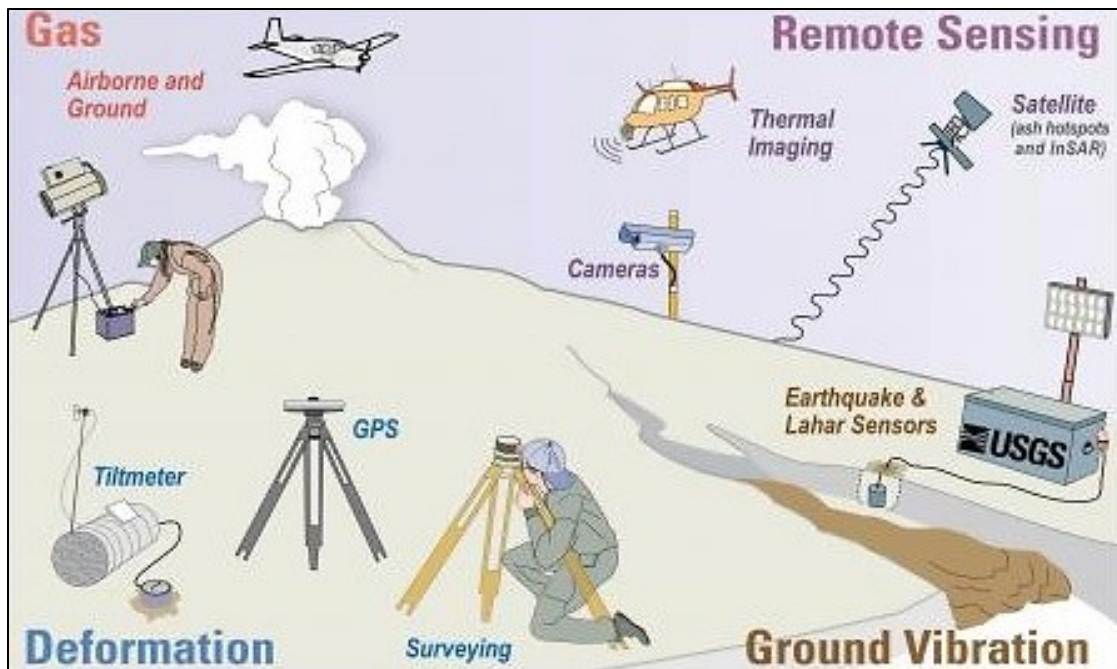
Figure 4.1 Volcanic monitoring techniques that are employed by the USGS Volcano Hazards Program (photo credit: U.S. Geological Survey, Department of the Interior) [68].

In addition to the programs that are currently applied by USGS to monitor volcanic eruptions, the EarthScope USArray program deploys a dense network of seismographic stations across United States. USArray consists of 400 broadband stations in a Transportable Array (TA) in a grid of locations with approximately 70 km spacing. Data that are acquired and analyzed from TA will lead to detection of abnormal seismic events such as an underground nuclear explosion [70]. Figure 4.2 illustrates the TA [71].
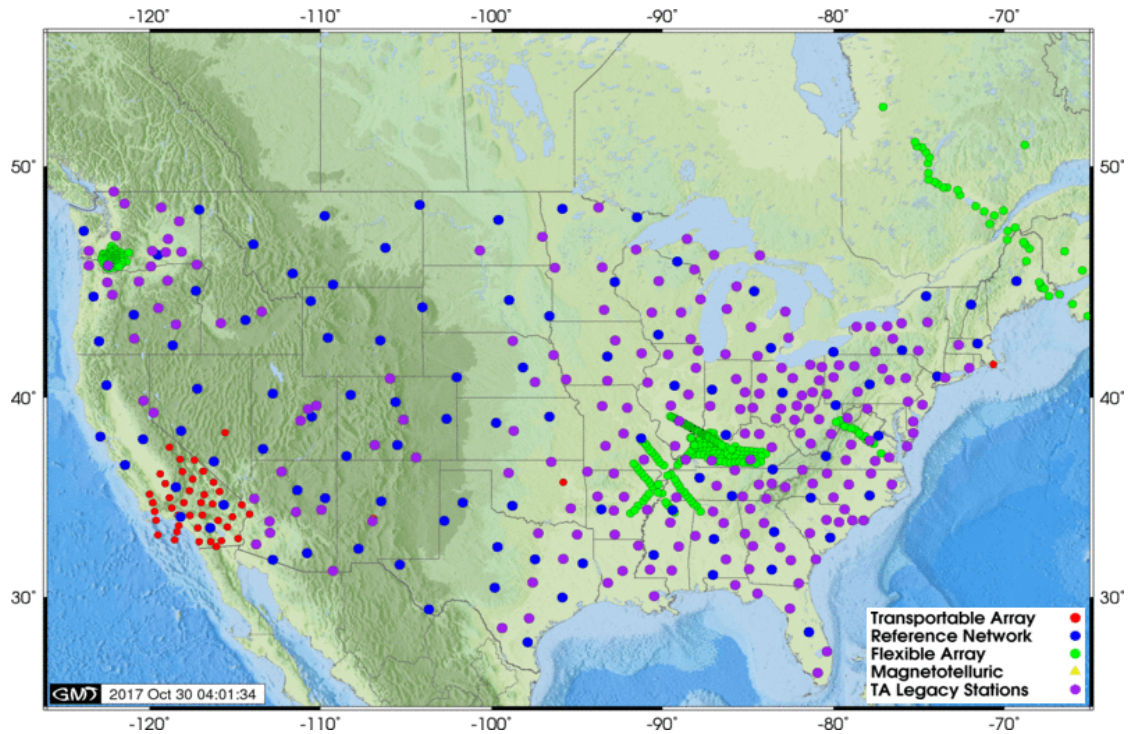
Figure 4.2 Transportable Array (photo credit: IRIS Data Management Center, EarthScope, and National Science Foundation) [71].

4.3 Limitations of the Existing Surveillance Systems for

Explosions

Current systems that are installed for monitoring volcanic eruptions have limitations in temperature measurements, detection of ash clouds, detection of ground deformation, and transmission time of satellite systems. For example, the thermocouple probe that is used for measuring the lava temperature cannot be applied to difficult volcano locations. Since volcanologist can only perform the direct temperature measurements within the vicinity of a volcano, safe conditions must exist. Temperature measurements can also be made from a distance with cameras that measure thermal infrared radiation

(TIR). However, TIR cameras can be completely or partially obscured by volcanic thick clouds (PDCs). Moreover, existing infrared satellite sensors capture only lava images of large areas with low resolution that limit the retrieval of fine-scale details from the volcanic thermal features [10].

Another limitation occurs when ground-based microwave radar systems are employed to measure volcanic fine ash. The fine ash becomes invisible to the radar system for distances greater than 50 km. Hence, the radio waves will not be reflected towards Earth, and might not be detected [11]. Conversely, ash cloud height and depth can be measured through observations generated from ground-based Light Detection and Ranging (LiDAR) optical systems. LiDAR systems typically demonstrate a higher sensitivity to the content of ash clouds as compared to microwave instruments, but counterbalanced by stronger path attenuation effects [12]. The data collection and processing performed by LiDAR systems can be time consuming. LiDAR equipment is also expensive [13].

The GPS is deployed to monitor the ground deformation of a volcano. However, the operational utility of the GPS is limited because it provides a small spatial and temporal coverage [14]. Furthermore, the limitation of the MODIS satellite remote sensing instrument is that MODIS retrieves ash clouds images within a lengthy time frame of fifteen to thirty minutes [6].

With regard to the limitations of nuclear detection systems that are deployed in the atmosphere and space, there are several contextual problems and difficulties related to the grid pattern of the system, the geography, and the site location.

Accordingly, acoustic systems can be affected by some natural phenomena such as volcanic eruptions, tornado, aurora, meteor, earthquake, wind patterns, and noise

background. Moreover, debris sampling methodology can be impacted by previous tests, and patterns of the wind. Furthermore, electromagnetic pulse (EMP) can be affected by atmospheric lightning. In addition, satellites that use instruments to measure radiation from a nuclear detonation include: neutrons, gamma-rays, and x-ray are influenced by cosmic ray showers, solar radiation, and trapped particles. Additionally, atmospheric fluorescence is influenced by lightning and cloud cover. In contrast, radio techniques (VLF, LF, HF, radio sounders, and Riometer) are mainly affected by ionospheric disturbances, polar zone, auroral regions, and the creation of a proper grid pattern in some locations. Additionally, the local noise affects HF, radio sounders, and Riometer among other radio techniques. Another technique, referred to as magnetic-telluric, can be influenced by ionospheric disturbances, auroral disturbance, and magnetic disturbance. Lastly, debris resonance is impacted by previous tests, natural dust, and wind patterns that form at a high altitude that results in unpredictable grid pattern [15].

CHAPTER 5: DESIGN OF THE PROPOSED FRAMEWORK

The proposed framework operates in three steps: preprocessing, training (learning), and testing (classification). The following factors were taken into consideration when the framework was designed and implemented: (1) definition of pattern classes, (2) pattern representation, (3) feature extraction methodologies, (4) classification techniques design and learning, and (5) selection of training and test samples.

5.1 Feature Extraction Approaches

5.1.1 Texture Features: Principal Component Analysis

The Principal Component Analysis (PCA) algorithm is a mathematical approach that projects the high-dimensional data onto a low-dimensional space. The reason for reducing the dimensions is that we can focus on those dimensions where there is a high difference between images in our dataset (i.e., high variance). Hence, in order to represent each sample using the most significant 100 basis vectors, the PCA algorithm is employed. During the preprocessing stage, we resize the color images to 64×64 pixels. Then, each sample (I_i) is converted to 8-bit grayscale vector (Γ_i). Consequently, the PCA steps during training (learning) are as follows [72]:

(1) Obtain images for training phase $I_1, I_2 \cdots I_M$, where $M = 5,327$, and represent each image I_i as a vector Γ_i.

(2) Find the average vector.

(3) Find the mean adjusted vector for every image vector Γ_i, by subtracting the average vector from each sample, and then assemble all data samples in a mean adjusted matrix.

(4) Compute the covariance matrix C.

(5) Calculate the eigenvectors (V) and eigenvalues (λ) of the computed covariance matrix C. After computing the eigenvalues, we will sort the eigenvalues (λ) by magnitude, and we will only keep the highest 100 eigenvalues and discard the rest.

(6) Compute the basis vectors. Thus, from the previous step, we have 100 eigenvectors ($EV_0, \cdots, EV_{99}$). These vectors will be assembled into an eigenvector matrix EV. Then, we will multiply EV by the mean adjusted matrix computed in step 3 to form the basis vectors.

(7) Describe each sample using a linear combination of basis vectors. These basis vectors have a magnitude of 1, and they are mutually orthogonal— meaning that the inner product of any two vectors will produce zero. This also can be described such that there is 90° angle between any two vectors in the eigenspace. These 100 features are invariant in terms of translation, illumination, and scale.

The training dataset contains $5,327$ samples. Hence, after applying the PCA to compute the most significant 100 eigenvectors and the corresponding eigenvalues, dimensions of the 2D training matrix are (5327×100). Figure 5.1 summarizes steps of PCA algorithm during training (learning).
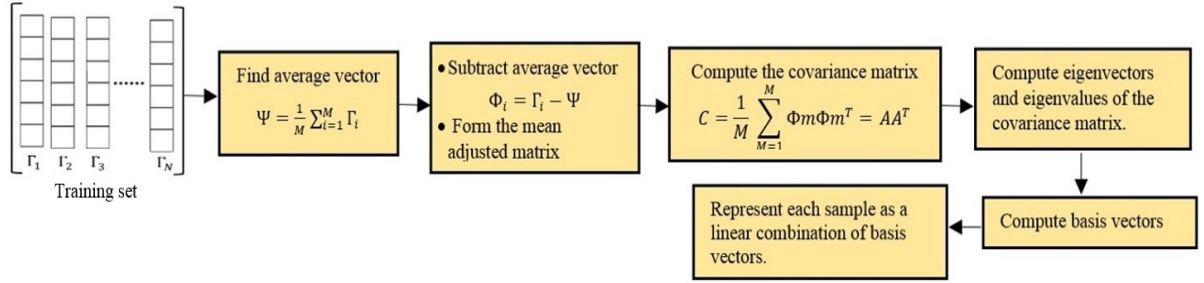
Figure 5.1 Steps of PCA algorithm during training (learning).

During the testing phase, each test image is resized to 64×64 pixels and then converted to a vector of size 4096×1 pixels. After that, the average image from the training process is subtracted from each test sample, resulting in the mean adjusted image. Consequently, the mean adjusted image of each sample gets projected on the eigenspace of 100 significant eigenvectors. As a result, dimensions of the 2D testing matrix are (5327×100).

5.1.2   Amplitude Features: YC_bC_r Color Model

Color is one of the physical properties of explosion and non-explosion phenomena, as the color depends on the temperature and the composition of each phenomenon of the proposed application.

Amplitude (spectral) features in the proposed framework are extracted by linear transformation of bitmap pixel component intensities (R, G, and B) to YC_bC_r color space [73]. YC_bC_r represents color as luminance component Y, and chrominance components C_b, which is blue minus luma ($B - Y$), and C_r, which is red minus luma ($R - Y$). Figure 5.2a depicts an input color image of 64×64 pixels of RGB components [74-78], and Figure 5.2b

illustrates the corresponding YC_bC_r output image of 64×64 pixels for the seven categories of explosion and non-explosions phenomena under consideration.

The choice of the appropriate color model depends on the target application and the effectiveness of the color transformation algorithm. Typically, YC_bC_r is used in the context of digital images such as JPEG images. Furthermore, computing YC_bC_r of an image is more efficient than RGB, because the human eye is more sensitive to change in brightness than change in color. Benoit Payette stated in [79] that red, green, blue, and luma components are in the gamma corrected space. No gamma correction is applied to color difference components C_b and C_r. Accordingly, RGB color space can be described as an illumination dependent color model. Moreover, engineers found that 60% to 70% of luminance (brightness) is in the green component of RGB. In the chrominance part C_b and C_r, the brightness information is removed from the blue and red colors. To overcome this disadvantage of RGB, we employ YC_bC_r.

In our experiments, we resize the RGB color images to 64×64 pixels during the preprocessing phase. For each image, R, G, and B color components are extracted and converted to YC_bC_r. Thus, we implement the following formula that describes the conversion of RGB color space into YC_bC_r color space according to ITU-R BT.601 [73]:

$$\begin{bmatrix} Y \\ C_b \\ C_r \end{bmatrix} = \begin{bmatrix} 16 \\ 128 \\ 128 \end{bmatrix} + \begin{bmatrix} 0.257 & 0.504 & 0.098 \\ -0.148 & -0.291 & 0.439 \\ 0.439 & -0.368 & -0.071 \end{bmatrix} \cdot \begin{bmatrix} R \\ G \\ B \end{bmatrix}, \tag{1}$$

where 8-bit representation of each component of YC_bC_r is specified by the recommendation 601, and $R, G, B \in [0,255]$, $Y \in [16,235]$, and C_b and $C_r \in [16,240]$. Y

has an excursion of 219 and an offset of +16, placing black at code 16 and white at code 235, whereas C_b and C_r have excursions of ± 112 and offset of +128.

	(a)	(b)
Pyroclastic density Current		
Lava fountain		
Lava and tephra fallout		
Nuclear explosion		
Wildfire		
Fireworks		
Sky cloud		
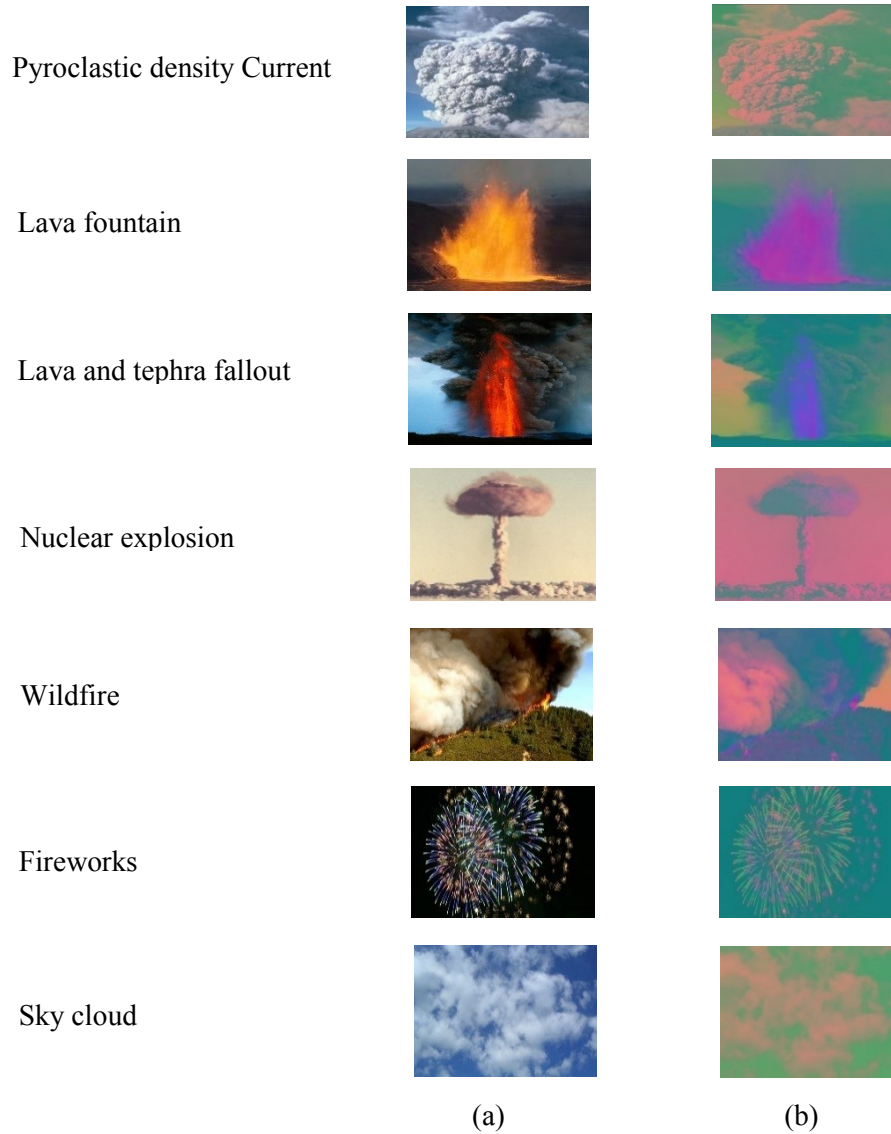
Figure 5.2 (a) Input color image of 64×64 pixels of RGB components; (b) The corresponding YCbCr output image of 64×64 pixels. Pyroclastic density currents: (photo credit: U.S. Geological Survey, Department of the Interior) [74]; Lava fountains: (photo credit: U.S. Geological Survey, U.S. Department of the Interior) [75]; Lava and tephra fallout: (photo credit: Tom Pfeiffer/ www.VolcanoDiscovery.com) [37]; Nuclear explosions: (photo credit: Gregory Walker, Trinity Atomic Web Site) [44]; Wildfires: (photo credit: John Newman, Wikimedia Commons website) [76]; Fireworks: (photo credit: PEXELS blog website) [77]; Sky cloud: (photo credit: Saperaud, Wikimedia Commons website) [78].

After we represent $5,327$ samples of the training set using the YC_bC_r color model, the dimensions of the 2D training matrix will be (5327×12288). Then, we apply PCA to extract the 100 most significant eigenvectors and eigenvalues. The 2D components matrix for the training phase is of dimensions (5327×100), whereas the components matrix for testing $5,327$ samples is of dimensions (5327×100). As seen in Figure 5.3, the block diagram shows the proposed YC_bC_r algorithm in the time domain.
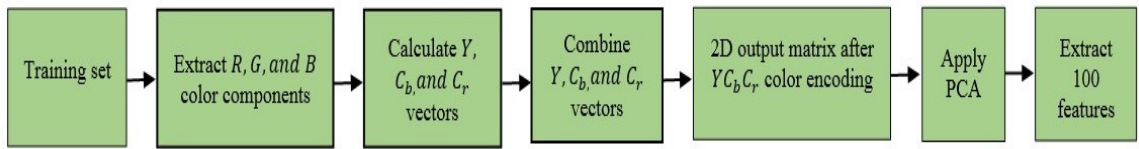
Figure 5.3 Block diagram for extracting the highest 100 eigenvectors after employing time domain YC_bC_r encoding schema.

5.1.3 Frequency Features: Radix-2 Fast Fourier Transform

In the proposed framework, features in the transform domain are calculated using the Radix-2 Fast Fourier Transform (Radix-2 FFT) algorithm. The Radix-2 FFT is a mathematical mechanism used to convert a spatial-domain image representation into a frequency-domain representation. It decomposes the image into a weighted sum of complex exponential functions called spectral components. The weighted terms at each frequency are the complex amplitude and phase. The speed of Radix-2 FFT comes at a cost of complexity at which the total computation is proportional to $N\log_2(N)$, and the discrete definition of Radix-2 FFT is given as follows [1]:

$$X_k = \sum_{m=0}^{N/2-1} x_{2m} e^{-\frac{2\pi i}{N}(2m)^k} + \sum_{m=0}^{N/2-1} x_{2m+1} e^{-\frac{2\pi i}{N}(2m+1)^k}. \qquad (2)$$

Before extracting the frequency features, a preprocessing step is required which is twofold. First, resizing each input color image in the time domain to 64×64 pixels. Second, converting the image (I_i) to a grayscale vector (Γ_i) of 8-bit intensity values. Consequently, The Radix-2 FFT algorithm can be achieved on 2D images by employing the following steps [80-83]:

(1) Perform a time-domain decomposition using a bit-reversal sorting algorithm to transform the input spatial image into a bit-reverse order array, and there are $\log_2 N$ stages needed for this decomposition, for example, a 16-point signal (2^4) requires 4 stages.

(2) A two-dimensional FFT can be executed as two one-dimensional FFT in sequence where 1D FFT is performed across all rows, replacing each row with its transform. Then, 1D FFT is performed across all columns, replacing each column with its transform.

(3) Combine the N frequency spectra in the correct reverse order at which the decomposition in the time domain was achieved. This step involves calculation of the core computational module of base-2-domain FFT algorithm, which is called a butterfly operation.

Figure 5.4a depicts an input color image of 64×64 pixels of RGB components for the seven categories of explosion and non-explosions phenomena under consideration in this research [74-78], Figure 5.4b displays the corresponding gray image of 64×64 pixels that generated during the preprocessing step, and Figure 5.4c illustrates the corresponding log plot for amplitude of Radix-2 FFT output image of size 64×64 pixels.

| | (a) | (b) | (c) |
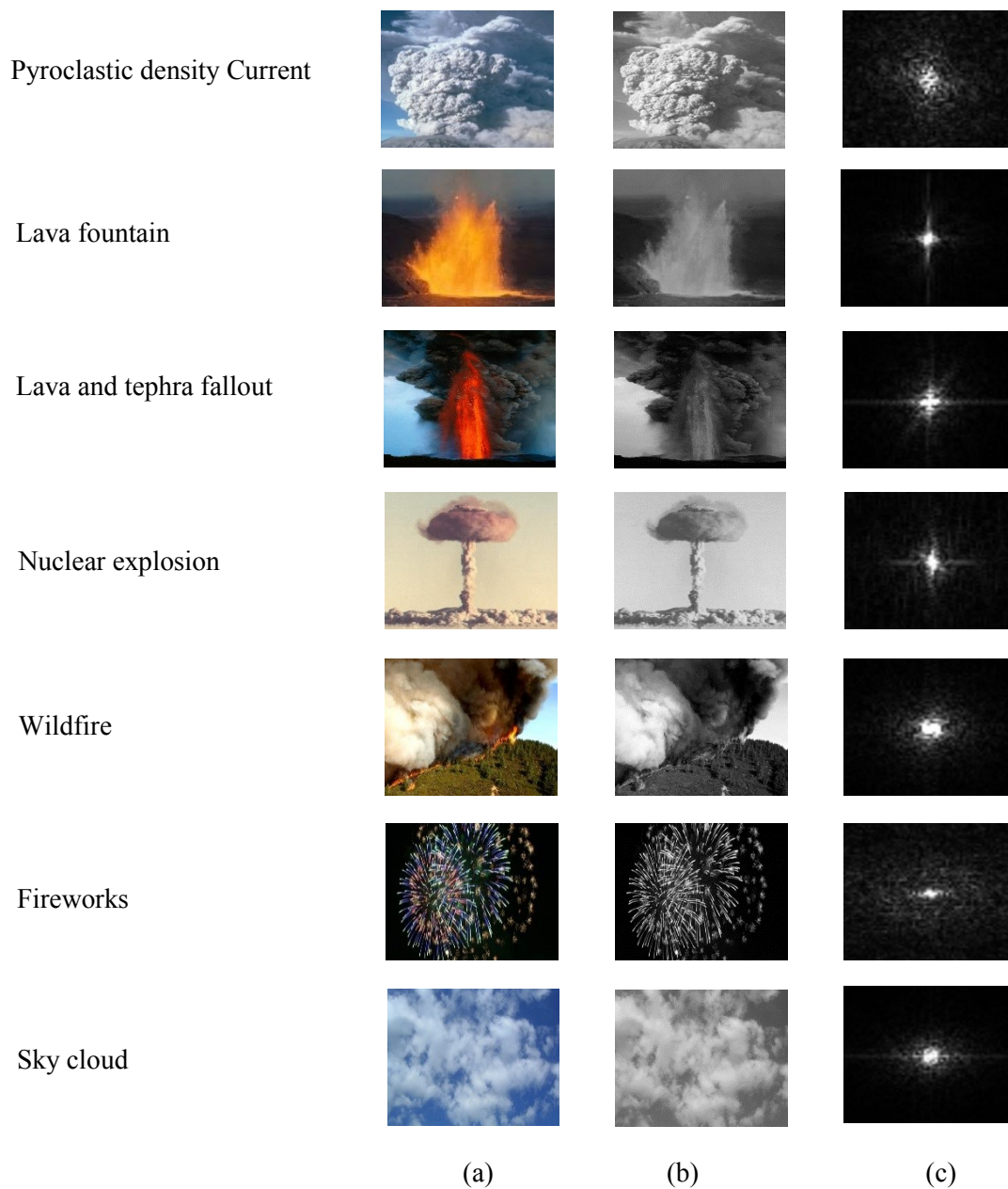
Figure 5.4 (a) Input color image of 64×64 pixels of RGB components; (b) The corresponding gray image of 64×64 pixels; (c) Log plot for amplitude of Radix-2 FFT output image of size 64×64 pixels. Pyroclastic density currents: (photo credit: U.S. Geological Survey, Department of the Interior) [74]; Lava fountains: (photo credit: U.S. Geological Survey, U.S. Department of the Interior) [75]; Lava and tephra fallout: (photo credit: Tom Pfeiffer/ www.VolcanoDiscovery.com) [37]; Nuclear explosions: (photo credit: Gregory Walker, Trinity Atomic Web Site) [44]; Wildfires: (photo credit: John Newman, Wikimedia Commons website) [76]; Fireworks: (photo credit: PEXELS blog website) [77]; Sky cloud: (photo credit: Saperaud, Wikimedia Commons website) [78].

Moreover, computing the frequency features of the image using Radix-2 FFT has the following advantages.

(1) Spectral analysis of the image using Radix-2 FFT reveals a significant amount of information about the geometric structure of 2D spatial images because of the use of orthogonal basis functions. Consequently, representing an image in the transform domain has a larger range than in the spatial domain.

(2) An image can contain high-frequency components if its gray levels (intensity values) are changing rapidly, or low-frequency components if its gray levels are changing slowly over the image space. For detecting such a change, Radix-2 FFT can be efficiently applied.

(3) The frequency spectrum of an image is represented in terms of the sum of sinusoidal waves using the Radix-2 FFT algorithm. These waves are eignfunctions of linear, constant-coefficient, and differential equations. Hence, they preserve their identity in a linear system where they can change the amplitude and the phase of the sinusoids, however, cannot change their basis structure [81].

After converting $5,327$ samples of the training set from the spatial domain into the frequency domain, the dimensions of the 2D training matrix will be (5327×4096). Then, we apply the PCA algorithm to extract the 100 most significant eigenvectors and eigenvalues, hence removing the noise. The components matrix for the training phase is of dimensions (5327×100), and the dimensions of the components matrix for testing $5,327$ samples are (5327×100). Figure 5.5 depicts a block diagram for extracting the 100 highest eigenvectors after employing the Radix-2 FFT algorithm.
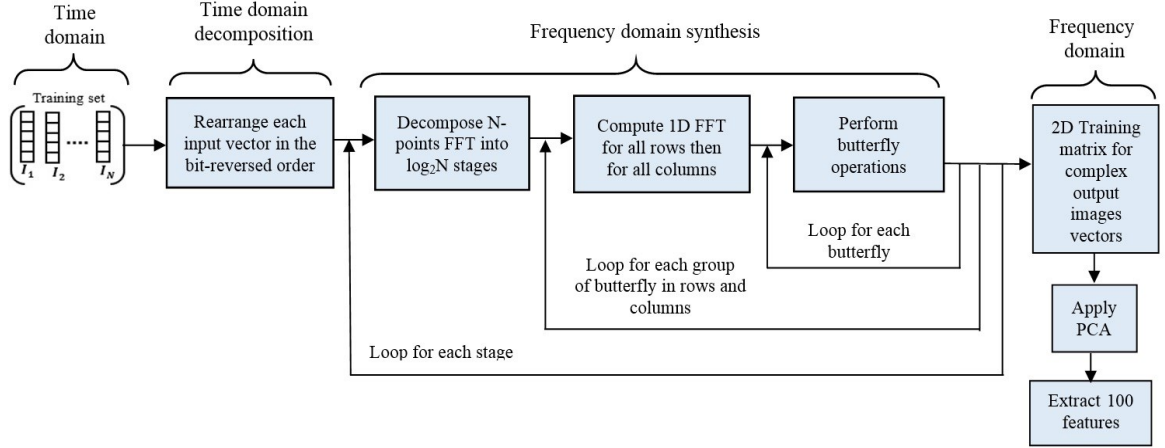
Figure 5.5 Block diagram for extracting the highest 100 eigenvectors after employing Radix-2 FFT algorithm.

5.1.4 Histogram Features: Uniform Local Binary Patterns

The Uniform Local Binary Patterns (ULBP) approach is employed to extract histogram features of the images of our application domain. ULBP is considered a local matching approach for pattern recognition, and it uses a set of local observations obtained from an explosion image to derive a model of a precise explosion pattern, which is subsequently used for classification. Indicating only uniform patterns of the entire image contributes to dimensionality reduction of the features vector length, computational simplicity, and increasing the classifiers performance as the computed histogram features are invariant to image rotation, scaling, illumination, and translation.

Consequently, we resize each input color image to 92×112 pixels, and we convert it into 8-bit gray scale. Then, we divide the gray scale image into 5×5 blocks. The LBP operator creates labels for image pixels in each block through thresholding the eight neighborhoods with the center pixel value. The new value for the center pixel (x_c, y_c) is

45

computed through concatenating all binary numbers in a clockwise direction. The value of the $LBP_{P,R}$ operator of (x_c, y_c) is defined as follows [84]:

$$LBP_{P,R}(x_c, y_c) = \sum_{P=0}^{P-1} f(i_p - i_c)2^p \qquad (3)$$

where the representation (P, R) denotes pixel neighborhoods at which P is the sampling points on a circle that has a radius R, and the symbols i_c and i_p are the values of the gray levels of the central pixel as well as the surrounding pixels. In our implementation $P = 8$, and $R = 1$. Additionally, the function $f(h)$ is given as follows [84]:

$$f(h) = \begin{Bmatrix} 1, & \text{if } h \geq 0 \\ 0, & \text{if } h < 0 \end{Bmatrix} \qquad (4)$$

Figure 5.6 illustrates the basic LBP operator such that the binary number 01111100 is equivalent to 124 decimal number. Therefore, (x_c, y_c) value will be modified to 124. This process is repeated by iterating over the entire block, and keeps updating each pixel value.
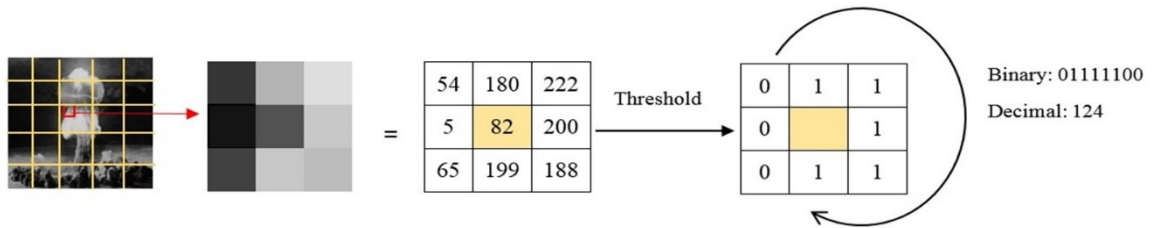
Figure 5.6 An illustration of the basic local binary pattern operator utilizing a nuclear explosion example.

Furthermore, we compute the uniform patterns for the entire image through the following procedure. We generate uniform patterns for each block if there are no more than two bitwise transitions from zero to one or vice versa once the binary bit pattern is circularly traversed. For instance, 00000001 (2 transactions) is a uniform pattern. Whereas,

01000001 (4 transactions) is a non-uniform pattern. As a result, the uniform patterns for the entire block will be within [0-57], and then we concatenate all regional histograms to construct a global description of the nuclear explosion image in our example. Hence, each image is represented by (5×5×58) features. Figure 5.7 depicts this procedure.
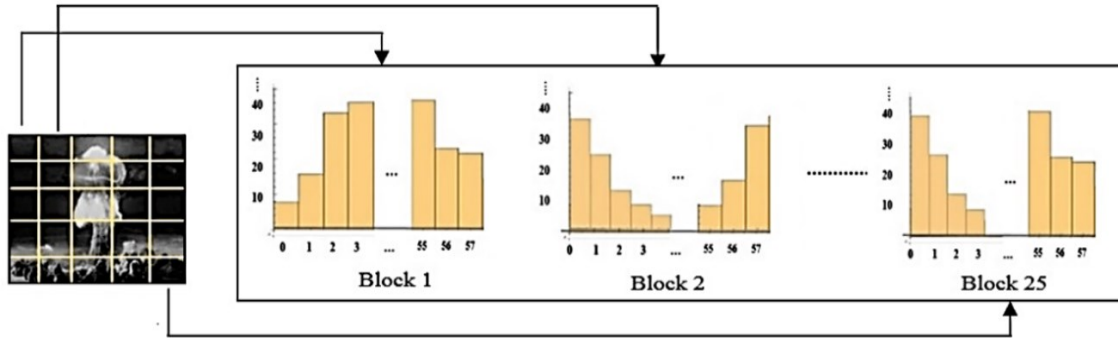
Figure 5.7 A uniform pattern histogram is extracted for each block in the entire image, and then all histograms are concatenated in a single histogram.

After representing $5,327$ samples of training and testing sets using ULBP algorithm, dimensions of the corresponding 2D matrices are (5327×1450). In fact, the background of any image will be preserved using ULBP because most of the pixels typically have the same gray level value within each background region of the same image. In order to overcome this drawback, we compute the most significant 100 eigenvectors and the corresponding eigenvalues using the PCA technique. Therefore, both 2D components matrix for training set as well as for testing set are of dimensions (5327×100).

5.2   Classification Techniques

The supervised learning task is performed in order to map the input data to the desired output data at which both data are labeled. Thus, the space will be separated into

classes or regions. In this section, we discuss the following multiclass classification techniques that we employ in our experiments.

5.2.1 Conventional Statistical Methods

Each example in the learning dataset is represented by a set of four vectors as follows: the first vector (at) consists of 100 texture features calculated using PCA algorithm on image intensity levels. The second vector (bt) comprises 100 amplitude features computed using YC_bC_r + PCA. The third vector (ct) contains 100 frequency features calculated using Radix-2 FFT + PCA, and the fourth vector (dt) includes 100 histogram features measured using ULBP + PCA.

Subsequently, these vectors are combined in one input vector for the training phase called Training Combiner Vector ($TRCV_i$) that has length of 400. Equation 5 summarizes the combination step. Likewise, this procedure will be repeated for each sample (i) in the testing set. As a result, each unknown sample will be presented using a Testing Combiner Vector ($TTCV_i$) during the testing stage.

$$[TRCV_i]_{400 \times 1} = \begin{bmatrix} [at_0, at_1, \cdots, at_{99}] + [bt_0, bt_1, \cdots, bt_{99}] + \\ [ct_0, ct_1, \cdots, ct_{99}] + [dt_0, dt_1, \cdots, dt_{99}] \end{bmatrix}_{400 \times 1} \tag{5}$$

Thus, we apply the following conventional statistical methods.

5.2.1.1 Euclidean Distance

Image vectors are considered points in the feature space. Hence, for each image feature vector $TTCV_i$ in the testing set, the Euclidean distance (ED) is measured with every

image feature vector in the training set TRCV (0,···, n-1), where n = 5, 327. Consequently, the minimum distance is stored, and its corresponding label is calculated. Euclidean distance is defined as follows.

$$ED_{TRCV,TTCV} = \sqrt{\sum_{i=0}^{n-1}(TRCV_i - TTCV_i)^2} \tag{6}$$

5.2.1.2 Correlation

The correlation indicates the strength and direction of the inner relationship between two image feature vectors in the feature space. Hence, for each image feature vector $TTCV_i$ in the testing set, the correlation is measured with every image vector in the training set TRCV $(0, \cdots, n-1)$, where n = 5, 327. Then, the maximum correlation value is stored, and its corresponding label is calculated. Correlation is given as follows.

$$C_{TRCV,TTCV} = \frac{\sum_{i=0}^{n-1}(TRCV_i - \overline{TRCV})(TTCV_i - \overline{TTCV})}{\sqrt{\sum_{i=0}^{n-1}(TRCV_i - \overline{TRCV})^2 \sum_{i=0}^{n-1}(TTCV_i - \overline{TTCV})^2}} \tag{7}$$

5.2.2 Classifiers

The abovementioned feature vectors in the sequence {(at), (bt), (ct), and (dt)} for each sample of the training set were normalized to be within the interval [-1,1]. Hence, for each component of a particular features vector, we subtract the mean (μ), then divide by the standard deviation of that corresponding vector values (σ). Then, these four feature vectors were combined in one input vector of length 400 ($TRCV_i$). Therefore, equation (8) describes a modified version of equation (5) after applying the normalization function.

Moreover, Figure 5.8 depicts the combining procedure of the measured features of the first

input image in the training set where the number of training samples (TS) is $5,327$, and

AddRange is a method in C# language that adds the elements of a normalized vector to the

end of a list.

$$[\text{TRCV}_i]_{400\times1} = \frac{[\text{normalize}([at_0, at_1, \cdots, at_{99}]) + \text{normalize}([bt_0, bt_1, \cdots, bt_{99}]) +}{\text{normalize}([ct_0, ct_1, \cdots, ct_{99}]) + \text{normalize}([dt_0, dt_1, \cdots, dt_{99}])]_{400\times1}} \qquad (8)$$

Similarly, normalization is employed to the computed feature vectors values for

each sample of the testing set before being combined in one input vector (TTCV_i) of length

400. Consequently, we employ the following classifiers.
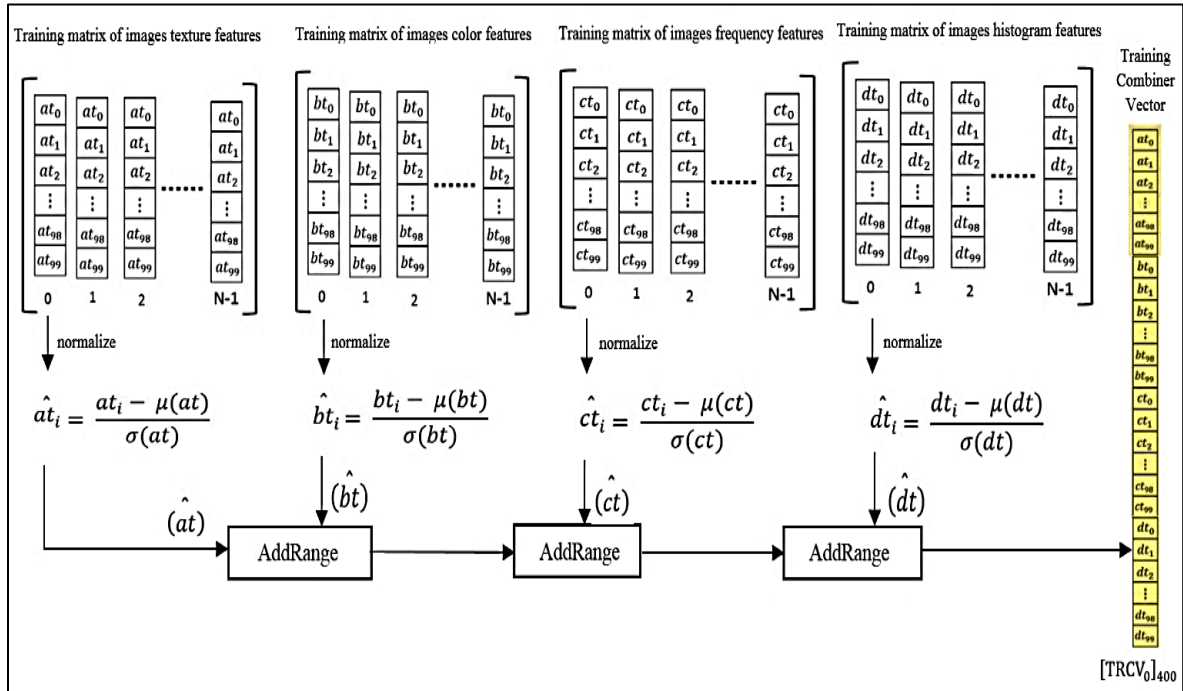
Figure 5.8 A graph for combining features that represents the first image in the training set.

5.2.2.1 K-Nearest Neighbors

K-Nearest Neighbors (KNN) is a non-parametric approach for performing a supervised classification. It aims to determine a predefined value (K) of training samples (TS) closest in terms of distance to a new sample and predict its label among TS. Thus, an unknown test sample is classified as it belongs to the category among its nearest neighbors that has the majority vote [85]. In our work, KNN is tested where K = 1, 3, or 5, TS = $5,327$, the number of output classes (M) = 7, and $[TRCV_i]_{400 \times 1}$ is the corresponding input vector of each sample (i) of TS.

5.2.2.2 One-Against-One Multiclass Support Vector Machine

This technique concurrently decreases the empirical error of the categorization while finding the superlative separating hyperplane which maximizes the margin between the closest points of classes. The margin represents the distance from the hyperplane to the closest data points in the feature space. Data points that are residing along the margin are called "support vector points." Hence, a linear combination of only these data points represents the solution [86].

The effectiveness of the SVM classifier relies on selecting the appropriate kernel function $K(x_i, x_j)$. This step is considered the first and the most important step in applying SVM to real-world data sets, and it is usually declared as the "kernel trick." Accordingly, we employ the most common kernels to map the data points of an input space to a high-

dimensional feature space. Thus, exploring the kernel that leads to generate the highest classification rate. These kernels are [87]:

- Linear kernel, which is given as follows:

$$K(x_i, x_j) = x_i^T x_j \tag{9}$$

- Polynomial kernels of degree 2 ,3, 4, 5, and 6, which is given as follows:

$$K(x_i, x_j) = (\gamma x_i^T x_j + r)^d, \gamma > 0 \tag{10}$$

- Gaussian kernel: Radial Basis Function (RBF), which is given as follows:

$$K(x_i, x_j) = \exp\left(-\gamma \|x_i - x_j\|^2\right), \gamma > 0 \tag{11}$$

- Sigmoid function, which is given as follows:

$$K(x_i, x_j) = \tanh(\gamma x_i^T + r) \tag{12}$$

where d, γ, r are kernel parameters.

Typically, SVM is considered a binary classification technique. However, it is possible to enhance it in order to handle multinomial classification problem through constructing multiple machines. Thus, we employ one-against-one SVM approach to deal with the multiclass problem under consideration. During training process, this approach creates a machine for each pair of categories, producing $K = M(M - 1)/2$ machines, where $M = 7$ target classes, $K = 21$ machines, and TS= 5, 327, and $[TRCV_i]_{400 \times 1}$ is the corresponding input vector of each sample (i) of TS. Furthermore, the Sequential Minimal Optimization (SMO) algorithm is used because it can quickly solve the SVM optimization quadratic problem (QP) to discover the optimal combination of the hyperplane parameters by dividing the problem into lower dimensional sub-problems and solving it without significantly depending on a numerical optimization technique [88].

During the testing phase of the SVM classifier, a new unknown test sample (sa) is categorized as belonging to class l* whose decision function (f_{l*}) generates the maximal value. The equation is provided as follows [1]:

$$l^* = \arg \max_{l=1,\cdots,M} f_1(sa) = \arg \max_{l=1,\cdots,M} \left(w_l^T \varphi(x) + b_l \right) \tag{13}$$

5.2.2.3 Multilayer Perceptron Model

It is a non-linear neural network model that is useful for solving supervised learning problems. MPL approximates a classification function that maps the input vector $[TRCV_i]_{400 \times 1}$ into a particular class. The architecture of the MLP model used in our experiments comprises three layers of nodes as follows: (1) one input layer that is identical in terms of length to the $TRCV_i$ input vector, (2) hidden layers ranging from one to four, and (3) one output layer where the number of the output neurons is seven. Figure 5.9a shows a single layer architecture, whereas Figure 5.9b depicts a multilayer architecture [84].

Furthermore, the sigmoid activation function is employed, and the Mean Square Error (MSE) is used as a criterion of the classification accuracy of the target application.

While training this model, the backpropagation algorithm using Stochastic Gradient Descent (SGD) is employed. The objective of backpropagation training algorithm is to reduce the MSE between the correct target output and the actual output from perceptron. Backpropagation training algorithm operates in the following two main phases [89]:

- The network takes the training input vector $TRCV_i$ that will be allowed to pass forward through various layers in order to calculate the output for each node. Then, these outputs of the neuron nodes in the output layer are compared as opposed to their desired answers or responses to yield the error term.

- A backward pass via neural network during which the proper error signal propagates to each node, as well as the corresponding changes of weights are modified.

During the testing phase of MPL, each unknown input pattern is allowed to propagate through various layers, and it is typically classified as it belongs to the category of the output node that produces a high value, compared with lower values in all other nodes.
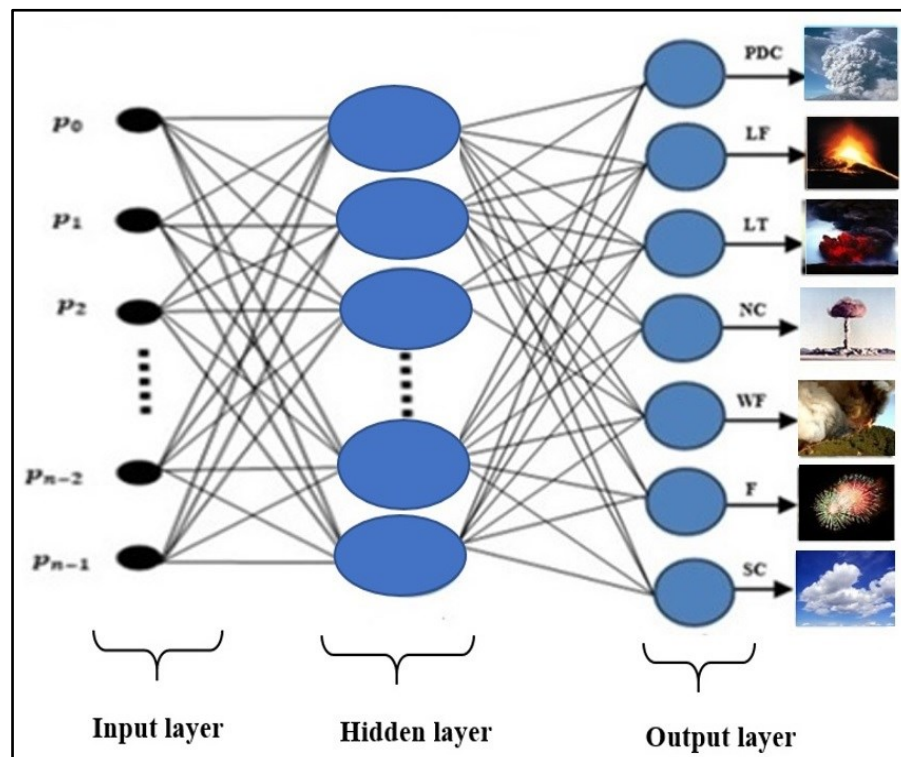
(a)
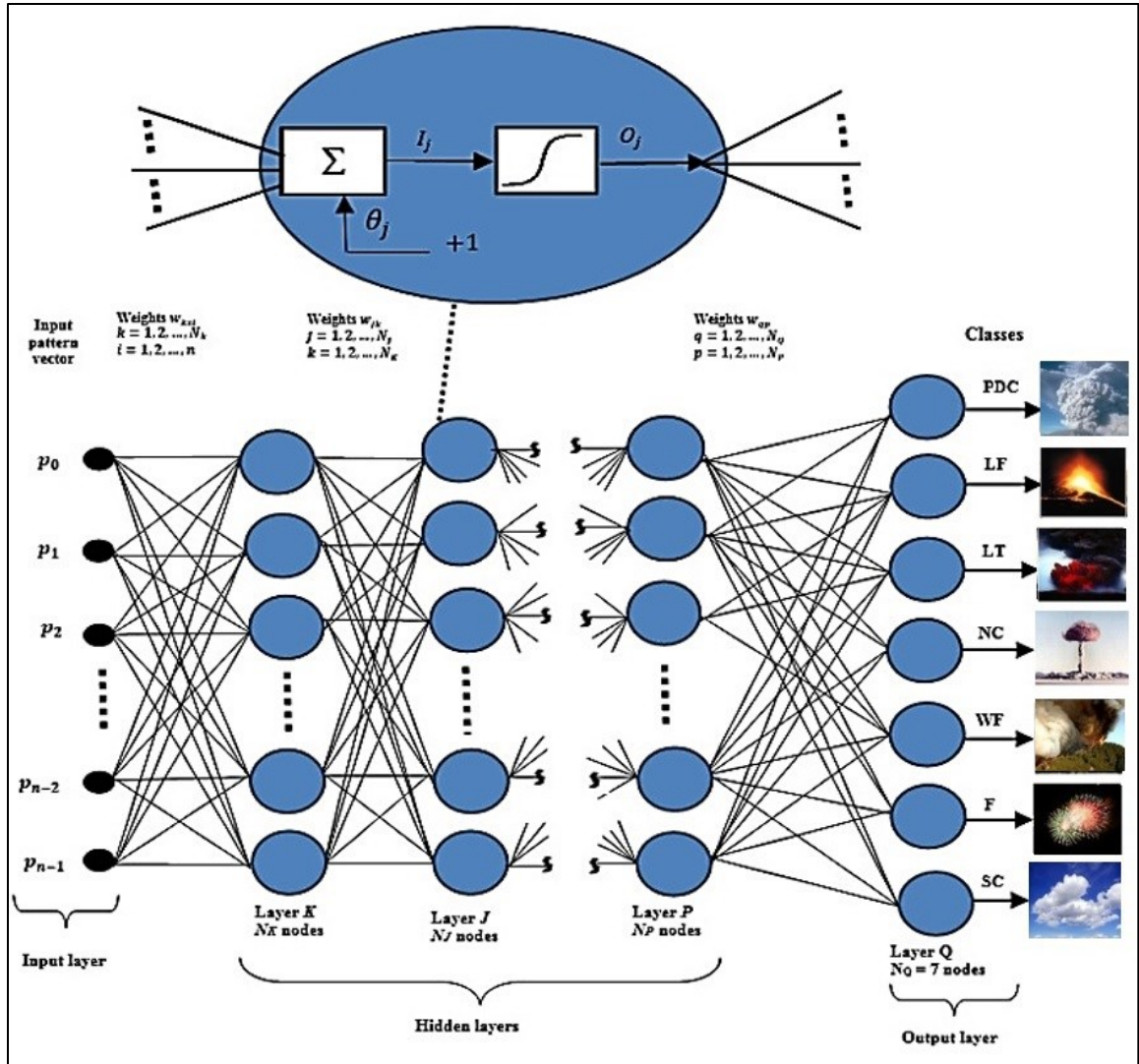
(b)

Figure 5.9 Architectures of MPL. (a) Single layer architecture; (b) Multilayer architecture [84], PDC: (photo credit: U.S. Geological Survey, Department of the Interior) [74], LF: (photo credit: Jeffrey B. Judd, U.S. Geological Survey) [90], LT: (photo credit: Tom Pfeiffer/ Volcano Discovery website) [91], NC: (photo credit: Gregory Walker, Trinity Atomic Web Site) [44], WF: (photo credit: John Newman, Wikimedia Commons website) [76], F: (photo credit: PEXELS blog website) [77], SC: (photo credit: Michael Jastremski, Wikimedia Commons website) [92].

CHAPTER 6: DATASET

Towards the supervised classification goal, there was a need for a large dataset. However, there is a lack of public datasets on explosion phenomena under consideration in this dissertation. Therefore, we had to collect our own dataset. In this section, we provide a description of our dataset that includes: the name that was given to our dataset, who collected the dataset samples, some resources of the dataset images, time frame of collecting the dataset, images type, patterns of the dataset, image editing before performing the preprocessing step by the classification techniques, and the number of images for training and testing phases of the classification task.

6.1 Volcanic and Nuclear Explosions (VNEX) Dataset

Our new dataset of color still images was collected by Sumaya Abusaleh during 2014-2017. In this dissertation, we will abbreviate our dataset as (VNEX) that stands for Volcanic and Nuclear Explosions. Furthermore, images of VNEX dataset were downloaded from different resources. For example, USGS website [93], Wikimedia Commons [94], Volcano Adventures website [95], Volcano Discovery website [96], National Weather Service/ National Oceanic and Atmospheric Administration (NOAA/NGDC) website [97], Exploratorium [98], Trinity Atomic website [44], blogs [77,99], and others.

VNEX dataset consists of $10,654$ color images distributed among 7 classes including 4 classes for explosion phenomena patterns, against 3 classes for non-explosion phenomena patterns. Explosion phenomena classes include: (1) pyroclastic density currents

(PDC), (2) lava fountains (LF), (3) lava and tephra fallout (LT), and (4) nuclear mushroom-shaped clouds (NC). On the other hand, non-explosion phenomena classes include: (1) wildfires (WF), (2) fireworks (F), and (3) sky clouds (SC).

Furthermore, the proposed categorization system works in two stages: training and testing. Tainting and testing images of VNEX are independent. Overall, there are $5,327$ training images and $5,327$ testing images. Table 6.1 illustrates the number of images in each class of training and testing sets.

Since VNEX categories are imbalanced distributions of images per each category, each class of VNEX dataset is divided into 50% images for training and 50% images for testing for consistency. Furthermore, while collecting the images of VNEX, we faced a difficulty on finding a large number of nuclear mushroom-shaped clouds (NC) images and the lava and tephra fallout (LT) images. Therefore, in the scenario where if the VNEX dataset was divided into 30 % for training and 70% for testing per each category, we will have about 913 of PDC samples for training, and 2131 of PDC samples for testing, and this division in this case can be considered sufficient for performing the desired classification task. In contrast, we will have about 236 of NC samples for training, and about 552 NC samples for testing. Similarly, we will have about 208 LT samples for training and about 484 LT samples for testing. Consequently, about 236 of NC training samples and 208 of LT training samples are relatively not enough to learn the classifiers under consideration. As a result, we have found through our experiments that the small number of samples for training will not be enough to learn the best hyperplane (decision surface) that can fit the training input vector properly, and hence have led to low accuracy using multiclass SVMs with different kernels, and MPL that uses the backpropagation training algorithm.

57

Furthermore, an explosion and non-explosion phenomenon may occur during the day or the night. Therefore, VNEX images have different backgrounds. In addition, we crop the area of an explosion or non-explosion of VNEX images manually, and then we save all samples using JPEG file format. Figure 6.1 displays nine random examples from the respective seven classes.

Table 6.1 Categories of VNEX dataset

Category		Number of Images		Total
		Training	Testing	
Explosions	Pyroclastic Density Currents (PDC)	1522	1522	3044
	Lava fountains (LF)	966	966	1932
	Lava and tephra fallout (LT)	346	346	692
	Nuclear mushroom clouds (NC)	394	394	788
Non-explosions	Wildfires (WF)	625	625	1250
	Fireworks (F)	980	980	1960
	Sky clouds (SC)	494	494	988
Total		5327	5327	10654
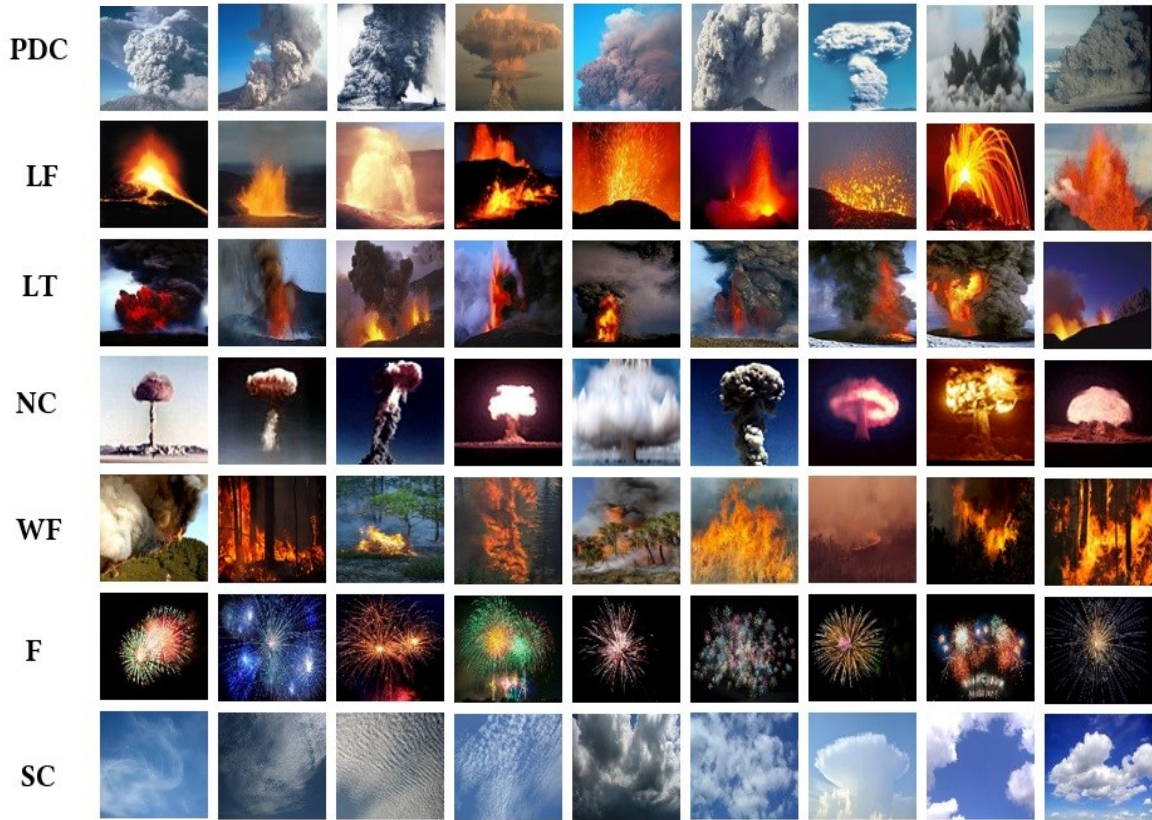
Figure 6.1 Random samples of VNEX dataset. PDC: a-d (photos credit: U.S. Geological Survey, Department of the Interior) [74,100-102], e (photo credit: Dr. Allan Sauter, SCRIPPS, and National Oceanic and Atmospheric Administration, U.S. Department of Commerce, U.S. Office of Ocean Exploration and Research.) [103], f (photo credit: Itu, Wikimedia Commons) [104], g (photo credit: Paginario, Wikimedia Commons) [105], h (photos credit: YouTube website) [31], and i (photo credit: R. Russell, Alaska Department of Fish and Game, U.S. Geological Survey) [106]; LF: a (photo credit: Jeffrey B. Judd, U.S. Geological Survey) [90], b and c (photos credit: U.S. Geological Survey, U.S. Department of the Interior) [75], d (photo credit: Nordic Volcanological Institute, Reykjavik, Iceland, Photographer: Gudmundur E. Sigvaldason, U.S. Geological Survey website) [107], and e-i (photos credit: Tom Pfeiffer/ Volcano Discovery website) [108-111]; LT: a-i (photos credit: Tom Pfeiffer/ Volcano Discovery website) [91,112-114]; NC: a-d, and f-i (photos credit: Gregory Walker, Trinity Atomic Web Site) [44], and e (photo credit: Nevada Field Office, National Nuclear Security Administration) [43]; WF: a (photo credit: John Newman, Wikimedia Commons website) [76], b (photo credit: Tatiana Bulyonkova, Wikimedia Commons website) [115], c (photo credit: Tilo, Wikimedia Commons website) [116], d (photo credit: Evil Saltine, Wikimedia Commons website) [117], e (photo credit: Ramos Keith, Wikimedia Commons website) [118], f (photo credit: U.S. Fish and Wildlife Service, Gerald Vicker, Wikimedia Commons website) [119], g (photo credit: Flip Schulke, U.S. National Archives and Records Administration, Wikimedia Commons website) [120], h (photo credit: US Air Force, Wikimedia Commons website) [121], and i (photo credit: Tatiana Bulyonkova, Wikimedia Commons website) [122]; F: a-i (photos credit: PEXELS blog website) [77]; SC: a-c, and e (photos credit: National Oceanic and Atmospheric Administration, Department of Commerce, National Weather Service) [49], d (photo credit: Simon Eugster, Wikimedia Commons website) [123], f (photo credit: Saperaud, Wikimedia Commons website) [78], g (photo credit: Simon Eugster, Wikimedia Commons website) [124], h (photo credit: Joniprittie, Wikimedia Commons website) [125], and i (photo credit: Michael Jastremski, Wikimedia Commons website) [92].

CHAPTER 7: EXPERIMENTAL RESULTS AND

DISCUSSION

We implemented the classification system using C# language under the Microsoft .Net framework 4.6, and it was operated on a workstation with an Intel(R) Core(TM) i7 CPU at 3.20 GHz, RAM (20.0 GB), and 64-bit OS. Experiments are divided into two main scenarios as follows.

7.1 Results of the VNEX Testing Set

Extensive experiments were conducted to determine the classification model that can achieve the best performance in terms of classification rate of testing instances of VNEX dataset. The classification rate in the proposed framework was computed using the following formula:

$$\text{Accuracy} = \frac{\text{TP+TN}}{\text{TP+FP+TN+FN}} \times 100\%, \tag{14}$$

where TP, TN, FP, and FN are the number of true positive, true negative, false positive, and false negative cases, respectively.

Consequently, the one-against-one multiclass SVM with degree 3 polynomial kernel has a superior classification rate in comparison to other classification methods being applied. It generates the highest accuracy of 79.16% and 90.85% when extracting 300 features (texture, color, and frequency) and 400 features (texture, color, frequency, and histogram), respectively. In addition, results inclusively show that extracting 400 features

performs consistently better when utilizing all multiclass classification techniques under consideration including: Euclidean distance, correlation, KNN, SVM, and MPL, rather than extracting 300 input features with the increase in the number of new testing samples. Table 7.1 demonstrates a performance comparison between different multiclass classification methods under consideration in terms of accuracy when extracting 300 features as opposed to 400 features of VNEX testing dataset.

Devoting to analyzing the behaviors of the multiclass classification systems that we addressed, conventional statistical methods including Euclidean distance (ED) and correlation (C) are not suitable to classify samples of VNEX dataset, because they are complex and in a large-scale space. Hence, giving a preference to predict the output label based on the minimum distance or maximum correlation has produced a poor performance of 77.42% and 78.02% using Euclidean distance and correlation, respectively.

Although KNN demonstrates a short time interval for the training phase, it has two drawbacks as follows: (1) each neighbor is equally important, and (2) the imbalanced training data is more likely to affect the performance of KNN. Thus, classes that have a large number of samples typically have a higher possibility to win. Intuitively, that explains why the KNN accomplished a poor classification rate of 77.42%, 76.70%, 76.22% when the value of k was set to 1, 3, and 5, respectively.

Furthermore, the kernel takes relationships in the data that are normally implicit and makes them explicit. As a result, the patterns classification takes place more easily. This is the reason behind the success of the kernel-based approaches such as SVM [126]. In this context, our results show the impact of selecting the proper kernel as a critical step when employing one-against-one multiclass SVM approach. Accordingly, the polynomial

kernel of degree 3 has led the SVM classifier to produce the highest classification rate of 90.85% for testing VNEX samples of 400 input features vector. Figure 7.1 illustrates the shape of the degree 3 polynomial kernel of a binary SVM model [86]. Hence, the one-against-one multiclass SVM with degree 3 polynomial kernel outperforms the SVM with a linear kernel, the SVM with a RBF kernel, and the SVM with a sigmoid kernel that produced a classification rate of 85.24%, 35.09 %, and 81.72%, respectively. Also, the empirical classification error using SVM increases as higher degree polynomials kernels are employed, which in turn tend to cause overfitting in the training set. Thus, polynomials 4, 5, and 6, generated a classification rate of 83.54%, 28.57%, and 28.57%, respectively.

Table 7.1 Performance comparison of multiclass classification methods when extracting 300 features against 400 features of VNEX testing set (5, 327 samples).

Category		Accuracy (input vector of 300 features)	Accuracy (input vector of 400 features)
ED		77.23%	77.42%
C		77.81%	78.02%
KNN	K value = 1	77.25%	77.42%
	K value = 3	76.42%	76.70%
	K value = 5	76.00%	76.22%
SVM	Linear	73.21 %	85.24%
	Polynomial 2	75.60 %	86.77%
	Polynomial 3	**79.16 %**	**90.85%**
	Polynomial 4	70.87 %	83.54%
	Polynomial 5	24.82 %	28.57%
	Polynomial 6	24.82 %	28.57%
	RBF	32.38%	35.09 %
	Sigmoid	71.92 %	81.72%
MPL		72.24%	82.05%
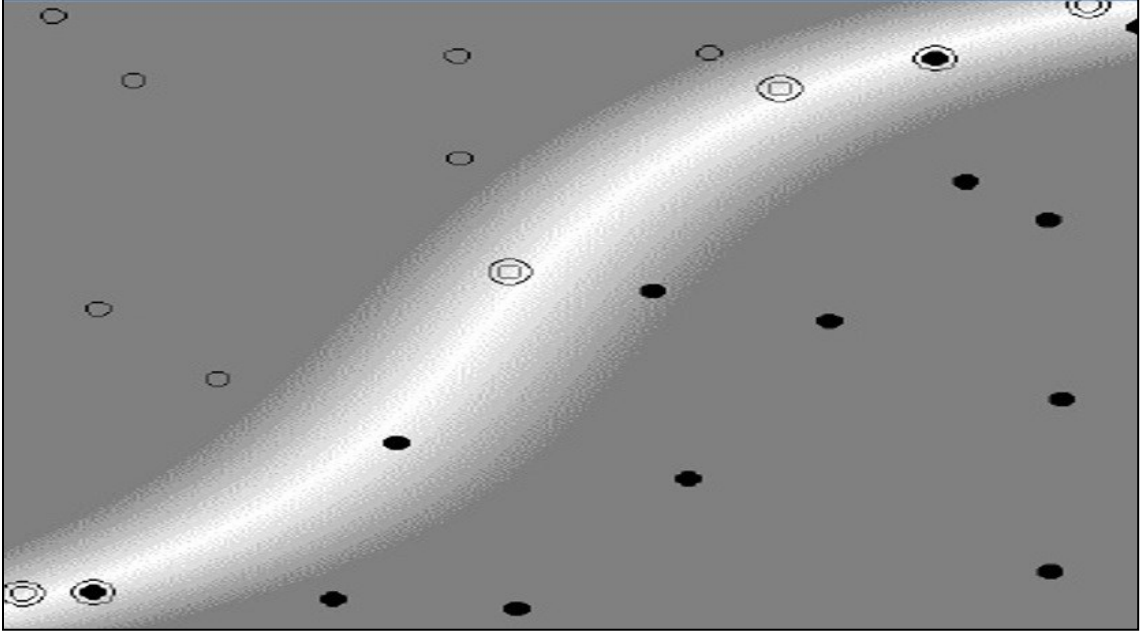
Figure 7.1 The shape of the degree 3 polynomial kernel of a binary SVM model [86].

Consequently, Table 7.2 presents a comparison between various multiclass classification techniques in terms of classified against misclassified images of VNEX testing set of a total $5,327$. The system evaluated two cases as follows. First, when texture, color, and frequency features of the proposed features extraction methodology were collectively accumulated in one input features vector of 300 length. Secondly, when texture, color, frequency, and histogram features of the proposed features extraction methodology, are accumulated in one input vector of 400 length for each sample.

Table 7.2 Classified against misclassified images of VNEX testing set $(5,327 \text{ samples})$ when the input vector length = 300, as compared to the input vector of length 400

Category		Input vector = 300		Input vector = 400	
		Classified	Misclassified	Classified	Misclassified
ED		4114	1213	4124	1203
C		4145	1182	4156	1171
KNN	K value = 1	4115	1212	4124	1203
	K value = 3	4071	1256	4086	1241
	K value = 5	4049	1278	4060	1267
SVM	Linear	3900	1427	4541	786
	Polynomial 2	4027	1300	4622	705
	Polynomial 3	**4270**	**1057**	**4840**	**487**
	Polynomial 4	3775	1552	4450	877
	Polynomial 5	1322	4005	1522	3805
	Polynomial 6	1322	4005	1522	3805
	RBF	1725	3602	1869	3458
	Sigmoid	3831	1496	4353	974
MPL		3848	1479	4371	956

Concerning MPL, we employ many architectures while performing our experiments. However, we only present in this section the architectures of MPL associated with their corresponding parameters that generated the highest classification rates on VNEX data. Accordingly, classification rate of 72.24%, and 82.05% were accomplished, when 300 features were fed into the network (architecture 1), in contrast to feeding an input features vector of length 400 (architecture 2), respectively. Table 7.3 lists the details of both architectures.

Table 7.3 Comparison between two architectures of MPL associated with their corresponding parameters and accuracy when extracting 300 features against 400 features of VNEX testing dataset (5,327 samples).

MPL Architectures and parameters		Accuracy
Architecture 1	Mean Square Error (MSE) = 0.009	72.24%
	Training iterations (epochs) = 17	
	Training rate = 0.0005	
	Error Threshold = 0.01	
	Max iteration = 500	
	Number of training samples = 5327	
	Number of testing samples = 5327	
	Input layer = 300 features vector	
	Hidden layer = 1	
	Hidden neurons (in the hidden layer) = 1000	
	Output layer = 7	
	Activation function: sigmoid	
Architecture 2	Mean Square Error (MSE) = 0.005	**82.05%**
	Training iterations (epochs) = 24	
	Training rate = 0.0005	
	Error Threshold = 0.01	
	Max iteration = 500	
	Number of training samples = 5327	
	Number of testing samples = 5327	
	Input layer = 400 features vector	
	Hidden layer = 1	
	Hidden neurons (in the hidden layer) = 2000	
	Output layer = 7	
	Activation function: sigmoid	

It is worth mentioning that when hidden layers increase while employing MPL, the accuracy decreases. Consequently, providing the aforementioned information of architecture 2 with the change of the numbers of hidden layers and the numbers of neurons per each layer, we have found that multiple hidden layers tend to reduce the accuracy of categorizing VNEX testing samples because of the overfitting. Figure 7.2 depicts a graph for the change of the accomplished classification rate based on the change of the number of hidden layers.
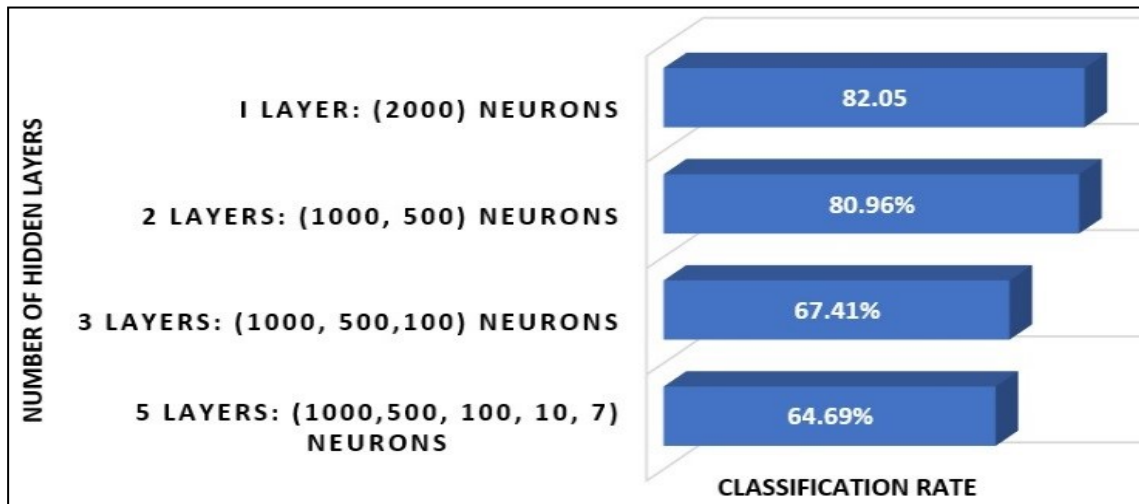
Figure 7.2 Graph illustrates the relationship between the classification rate and the number of hidden layers, where the input vector = 400, the output classes = 7, and using the testing set of VNEX dataset.

Moreover, Figure 7.3 illustrates a chart of classified versus misclassified samples of the VNEX dataset, where the total number of testing samples is $5,327$, input features vector $= 400$, and the classification method is one-against-one multiclass SVM with degree 3 polynomial kernel. Out of 1522 for PDC samples, 966 for LF samples, 346 for LT samples, 394 for NC samples, 625 for WF samples, 980 for F samples, and 494 for SC samples, the number of misclassified samples were 58, 62, 65, 30, 105, 15, and 45, respectively. In this view, the lowest number of misclassified samples attained while categorizing F samples. In contrast, the highest number of misclassified samples obtained while classifying LT samples.
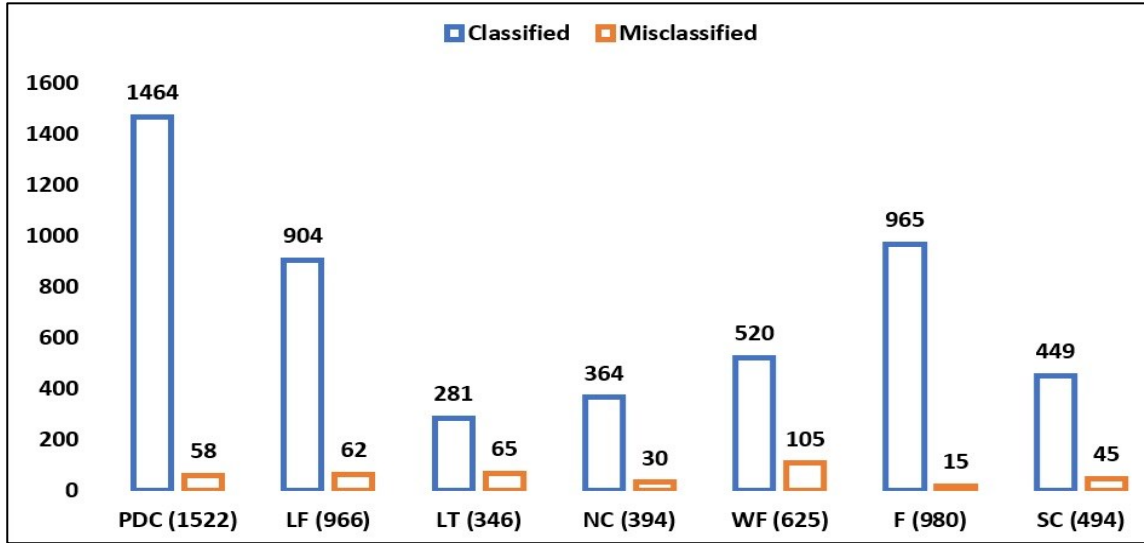
Figure 7.3 Graph of classified as opposed to misclassified images of VNEX testing set using the multiclass SVM with degree 3 polynomial kernel, and the input vector length = 400.

As seen in Table 7.4, the confusion matrix is also used to evaluate the performance of the multiclass SVM classifier with degree 3 polynomial kernel on VNEX dataset, at which the testing set of $5,327$ samples were represented by 400 features, and the number of the output classes (labels) is equal to 7. It illustrates the correctly and incorrectly recognized samples for each class. The fact derived from the confusion matrix is that samples of the VNEX dataset are complex because of the similarity of regions among some still images of the phenomena under consideration. As a result, the average accuracy obtained was 90.85%. Precisely, the highest accuracy of 98.47% accomplished while testing fireworks samples with a few samples misclassified into LT and LF categories, because all three categories have a luminosity property. In contrast, the lowest accuracy of 81.21% achieved while testing LT samples with some samples misclassified into PDC, LF, WF, and F, as the nature of LT phenomena involves the existence of two regions including

67

lava (luminous region) and tephra (non-luminous region) with varied density and color combinations of both regions in the scene during explosive or effusive eruptions. Likewise, WF achieved an accuracy of 83.2% with some of its samples misclassified into PDC, LF, LT, and F because of the presence of either visible flame region (luminous), smoke region (non-luminous) of white or gray to black colors of the smoke with different thickness, or both regions.

Consequently, evaluation results presented in the confusion matrix demonstrate that approximately a classification rate of 96.19%, 93.58%, 92.39%, and 90.89% were achieved for PDC, LF, NC, and SC, respectively. This indicates the effectiveness of the developed system. Nevertheless, the difficulty of the problem is obvious in the following cases. When a PDC phenomenon generated from a steam-driven, boiling-over, and continuous column collapse mechanisms, it may produce white dense clouds, which in turn will increase the possibility of incorrectly classifying some of PDC samples as they belong to SC category. Also, some volcanoes may produce natural mushroom clouds under the gravity force, and thus those PDC samples may be incorrectly predicted by the classifier as NC. Similarly, sky clouds (SC) typically have a white color, some types form at low levels, and have different shapes such as vertical, heap, and fluffy resulting in misclassification for some SC samples as if they belong to PDC. Additionally, some SC samples were misclassified as if they belong to WF at which a dense white smoke appears in some observation during the smoldering stage of the combustion. Moreover, during the time frame of the growth of the nuclear mushroom cloud, a luminous fireball appears that results in misclassification of some samples as LF, LT, and WF. On the other hand, when the fireball is no longer luminous, some dense clouds were misclassified as if they belong to PDC.

Table 7.4 Confusion matrix for the multiclass degree-3 polynomial kernel SVM classifier, with input features vector of length 400.

Actual	Predicted results							Accuarcy
	PDC	LF	LT	NC	WF	F	SC	
PDC (1522)	**1464**	8	24	1	19	0	6	96.19%
LF (966)	28	**904**	8	1	15	10	0	93.58%
LT (346)	30	22	**281**	0	10	3	0	81.21%
NC (394)	14	5	8	**364**	3	0	0	92.39%
WF (625)	32	50	14	0	**520**	9	0	83.2%
F (980)	0	13	2	0	0	**965**	0	98.47%
SC (494)	43	0	0	0	2	0	**449**	90.89%

In addition, we examine the computational time required to categorize one test sample of VNEX dataset during the testing phase. To accomplish this goal, we split the total time frame into the following stages: (1) the time needed for computing 100 texture features using PCA, (2) the time consumed for extracting 100 color features using YC_bC_r + PCA, (3) the time consumed for extracting 100 frequency features using Radix-2 FFT + PCA, (4) the time consumed for extracting 100 histogram features using ULBP + PCA, (5) the time utilized to combine the measured 400 features in an input vector, (6) the time needed to pass the test sample to the SVM, and (7) the categorization time utilized to predict the test sample label. Thus, the total execution time for classifying one test image was nearly 117ms. Table 7.5 provides the execution time related to each stage. As a result, we achieve a trade-off between the computation time and the accuracy while employing our proposed classification system.

Table 7.5 Analysis of the execution time in milliseconds for testing one test sample.

Stage	Execution time
Extracting 100 texture features using PCA	15
Extracting 100 color features using YC_bC_r+ PCA	19
Extracting 100 frequency features using Radix-2 FFT+ PCA	32
Extracting 100 histogram features using ULBP + PCA	21
Combining 400 features in an input vector	11
Passing 1 image to the classifier	1
Categorizing 1 image into a specific category	18
Total time in milliseconds	**117 ms**

Thus, if we processed every fourth frame of a 30fps video, our system can do a near real-time recognition of an explosion.

7.2 Results of a YouTube Video Testing Set

In this section, we used the training set of VNEX dataset that includes $5,327$ samples for training the multiclass degree-3 polynomial kernel SVM classifier. In contrast, for the testing phase of the classification system, we extracted seven videos from multiple videos that were downloaded from the YouTube website [127-131]. The number of retrieved frames of video sequences for each category was 140 frames. Hence, the totality of the testing set is 980 samples. Accordingly, once the one-against-one multiclass degree-3 polynomial kernel SVM model is trained, our goal is to test how this model will behave on a new testing set that differs from VNEX testing set.

Consequently, the extracted videos were saved using MPEG file format, and their resolution was 720×480 pixels at 29 frames per second (fps). These videos were converted to frames and saved using JPEG file format. Since the length of the extracted videos varied,

the max number of test samples for each category was determined based on the length of the shortest video among them for consistency. Accordingly, the first 140 frames of each video were used for testing the proposed classification methodology. These frames were resized to 64×64 pixels. Figure 7.4 displays some of the retrieved video sequences for the seven categories under consideration.
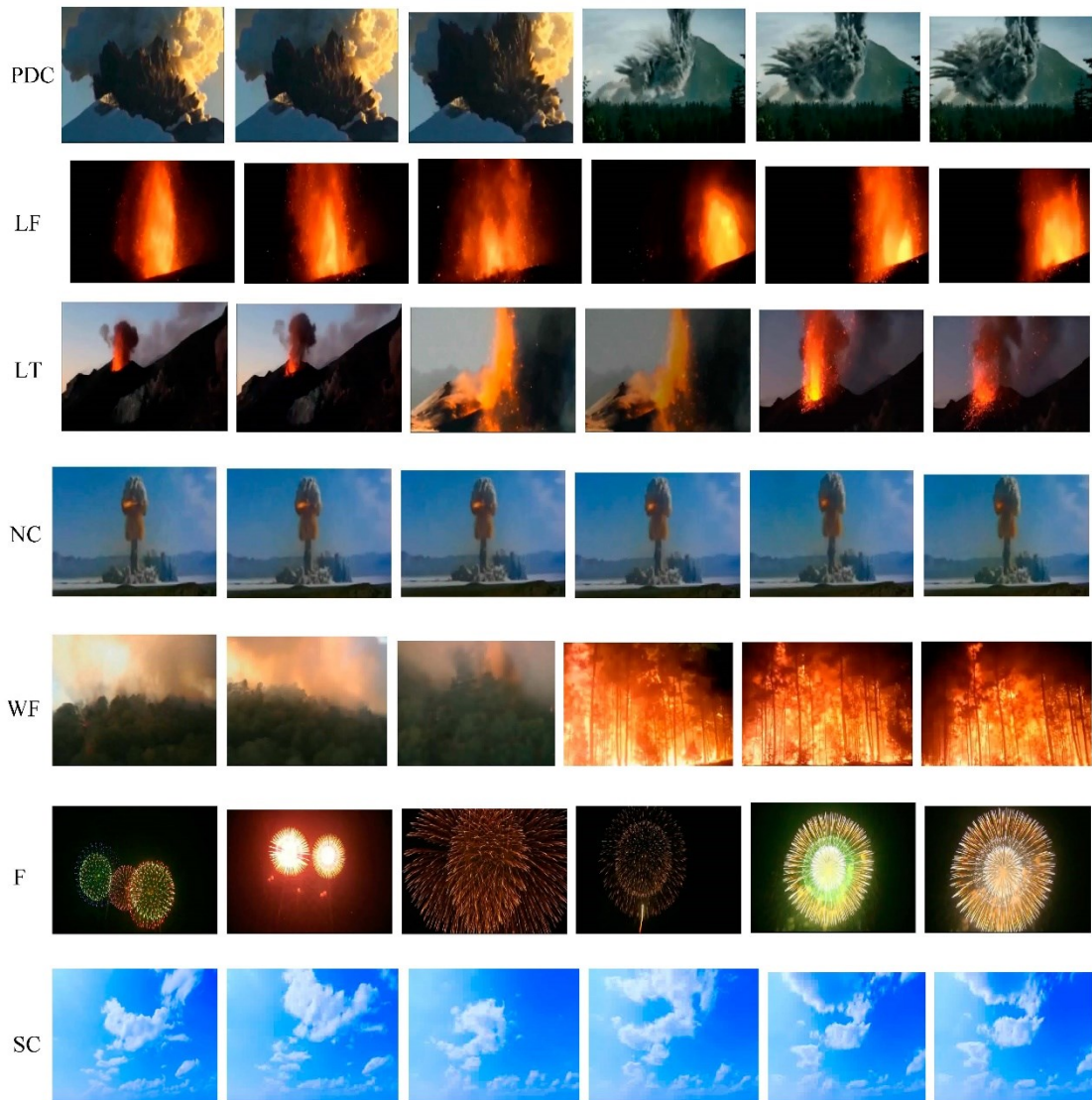
Figure 7.4 Some samples of the retrieved video sequences in the testing set [127-131].

During the testing phase of the classification system, each frame was defined by 100 features after extracting texture features using the PCA algorithm on intensity levels, 100 color features after applying YC_bC_r + PCA, and finally, 100 frequency features after applying Radix-2 FFT + PCA. Furthermore, these 300 features were combined into one input vector, and then passed to a degree-3 polynomial kernel SVM classifier and assigned to a specific category. Table 7.6 illustrates details of videos of the seven classes under consideration as well as a comparison between patterns of the proposed classification system in terms of accuracy (classification rate).

Table 7.6 Comparison between patterns in terms of accuracy.

Category	Frame rate	Resolution of video sequences	Number of retrieved frames for testing	Frames resized during preprocessing	Features input vector	Accuracy
Video 1—PDC	29 fps	720 × 480	140	64 × 64	300	98.57%
Video 2—LF	29 fps	720 × 480	140	64 × 64	300	90.71%
Video 3—LT	29 fps	720 × 480	140	64 × 64	300	83.57%
Video 4—NC	29 fps	720 × 480	140	64 × 64	300	**100%**
Video 5—WF	29 fps	720 × 480	140	64 × 64	300	85.71%
Video 6—F	29 fps	720 × 480	140	64 × 64	300	**100%**
Video 7—SC	29 fps	720 × 480	140	64 × 64	300	**100%**

The proposed explosion categorization system achieved 94.08% accuracy, where NC, F, and SC samples were classified correctly with 100% accuracy, followed by PDC, LF, WF, and LT that achieved 98.57%, 90.71%, 85.71%, and 83.57%, respectively. However, LT and WF phenomena are the complex.

Figure 7.5 depicts a chart of classified versus misclassified input test sets of 140 samples for each category of the proposed application. Out of 140 frames of each testing set, 2, 13, 23, and 20, were misclassified for PDC, LF, LT, and WF, respectively. In contrast, all frames of NC, F, and SC testing sets were classified correctly.
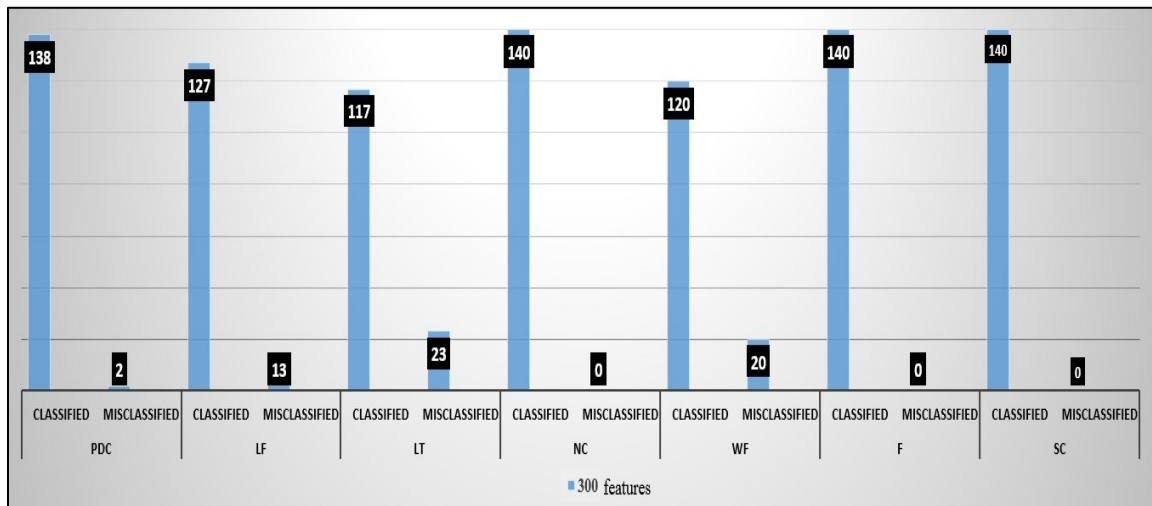
Figure 7.5 Chart of classified versus misclassified samples of the video sequences testing set.

Table 7.7 demonstrates the confusion matrix for multiclass degree-3 polynomial kernel SVM classifier where testing samples of 140 for each category are represented by 300 features. Nevertheless, the data of images are complex. In this view, the LT category is a combination of lava and tephra fallout products that deposited together directly by an effusive eruption in this example. The display of some LT scenes results in misclassified samples among PDC and LF. Likewise, because of the luminous region (lava) which is

similar to the flame, and non-luminous region of the image (tephra) that is similar to the dark smoke, some LT scenes were misclassified as WF.

Moreover, WF is also a complex category; the video we played displays a wildfire that occurred during the day and another during the night. Wildfire produce flames (luminous region) during the flaming stage of the combustion process, and smoke (flameless region) during smoldering combustion (non-flaming stage of fire). Flames of wildfires typically glow red then orange and then transmitting to yellow. Then, hot flaming combustion transfers more fuel (wood) into carbon compounds that formed into tiny elements. These particles absorb light making them appear as gray to black smoke. On the other hand, smoldering combustion typically reflects light, producing a white color appearance from the smoke. Thus, wildfire may generate white smoke. As a result, some of the WF samples were classified as if they belong to PDC, LF, and F.

Table 7.7 Confusion matrix for multiclass degree-3 polynomial kernel SVM classifier, where input vector = 300 features.

Actual	Predicted results						
	PDC	LF	LT	NC	WF	F	SC
PDC (140)	**138**	0	2	0	0	0	0
LF (140)	0	**127**	0	0	0	13	0
LT (140)	10	8	**117**	0	5	0	0
NC (140)	0	0	0	**140**	0	0	0
WF (140)	5	9	0	0	**120**	6	0
F (140)	0	0	0	0	0	**140**	0
SC (140)	0	0	0	0	0	0	**140**

Furthermore, a few PDC samples were misclassified as LT because of the non-luminosity property they both share. Furthermore, some lava samples were classified as if they belong to the fireworks class because of its luminosity property that both categories share. In particular, the video displays a lava fountain that was venting during the night. Luminosity of lava is related to its color (physical property) that indicates the composition and temperature. On the other hand, light from the fireworks is due to the chemical reactions of metal salts. In a consequence, once fireworks are ignited by lighter or a match, the energy absorbed by an atom of a metal salt reorganizes its electrons from the lowest-energy state that is called the ground state, up to a higher-energy state that is called an excited state. The excess energy of the excited state is released as a light that has a specific color to be displayed as ignitable shapes.

In an effort to improve the classification rate of 94.08%, we employed the proposed research methodology on the same video testing set where 140 frames per each class were retrieved. Each frame was defined by using an input vector of 400 in length that combined the texture, color, frequency, and histogram features. Then, the input vector was fed into the multiclass SVM with degree 3 polynomial kernel. As a result, we achieved a significant increase of 4.08% in the average accuracy from 94.08% to 98.16% because of the approximate increase of 1.43 % in PDC precision, 9.29% in LF precision, 8.57% in LT precision, and 9.29 % in WF precision. Figure 7.6 illustrates the comparison between both approaches in terms of the accuracy (classification rate) for the seven classes under consideration.
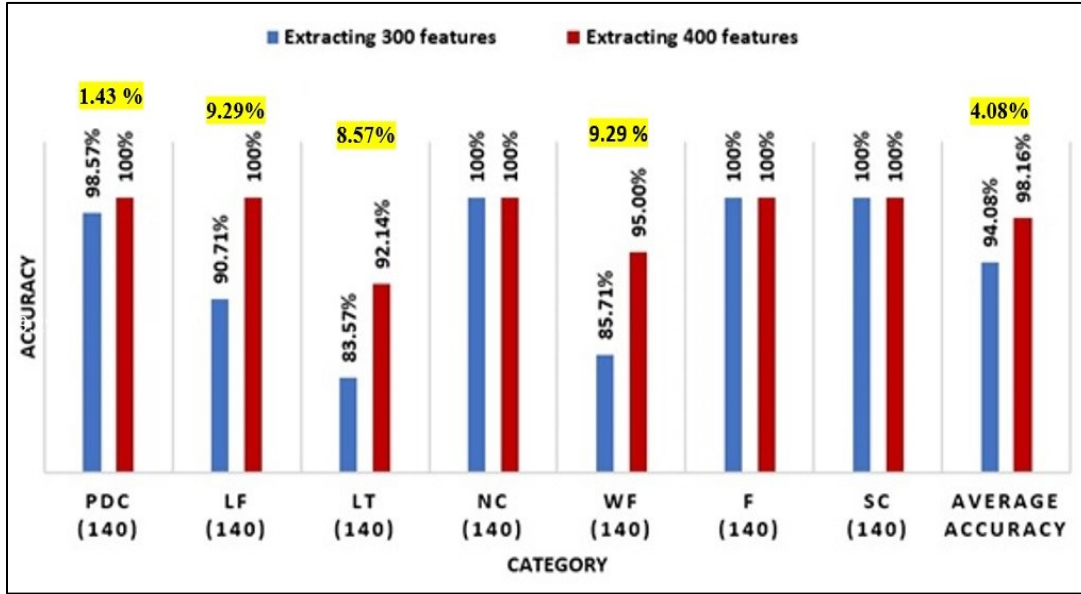
Figure 7.6 Comparison between the accuracy of the multiclass SVM with degree 3 polynomial kernel when the input vector is 300 features as compared to the input vector of 400 features using the video sequence testing set where each class includes 140 frames.

7.3 Results of Video Frames Captured in a Real-Time Environment Using a Drone

Since we had no access to outdoor explosion zones, we were only able to conduct indoor experiments. We performed our indoor experiments using a drone in real-time and the YouTube videos previously mentioned in section 7.2 [127-131].

In reality, drones can access very dangerous locations where explosions occur, which are difficult for humans to explore. Once an active volcano has erupted, the area around the volcano's crater becomes hazardous for a few years and access is restricted to guarantee people's safety. Typically, video cameras are deployed permanently to monitor any volcanic eruptions. Once an eruption occurs, these cameras will be damaged, and the

restricted area around the volcano will make it impossible to replace any of the video cameras. For example, in 1990, approximately all of the camera sensors malfunctioned during the eruption of Mt. Unzen-Fugen in Japan. So, retrieving any volcanic data was difficult. In this scenario, a drone quadcopter would have been a viable option in order to collect observations for the classification purpose.

In addition, drones are increasingly relied upon by military forces to observe nuclear activities. In tactical situations, drones can monitor battlefields. Thus, the need for military personnel is diminished.

Traditionally, a transducer provides inputs for a pattern recognition system in order to gather real-time observations to be classified. In our experiments, the transducer is the camera sensor at the front of the quadcopter, Parrot AR. Drone 2.0. This embedded frontal camera is a CMOS sensor with 90° angle lens. The resolution of the drone's frontal camera is 640 X 360 (360p), and it can capture up to 30fps [132].

Furthermore, we chose to use AR.Drone 2.0 for the following reasons: (1) ready-to-use sensory and control equipment, (2) designed to fly indoor or outdoor, (3) an autonomous Unmanned Aerial Vehicles (UAV) that have the capability to hover in mid-air and can fly in all directions, (4) the availability of open-access control system and a software development kit for a real-time video processing application, and (5) a low cost platform [132]. Figures 7.7a and 7.7b depict a front view of the AR.Drone 2.0 that shows the embedded camera at the front, and a top view of AR.Drone 2.0, respectively.
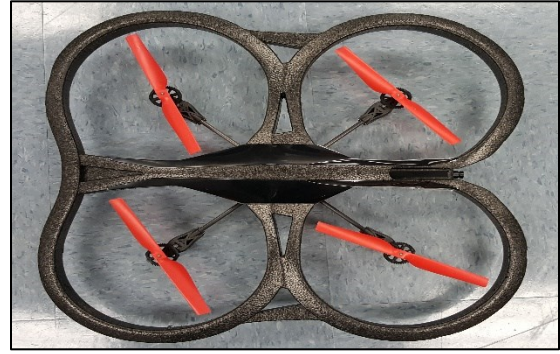
(a)   (b)

Figure 7.7 (a) Front view of AR.Drone 2.0 quadcopter (photo credit: Sumaya Abusaleh, University of Bridgeport); (b) Top view of AR.Drone 2.0 (photo credit as per Figure 7.7a).

In our application, the graphical user interface (GUI) was implemented using the Java Development Kit (JDK) 1.8, and the eclipse IDE. Furthermore, AR.Drone 2.0 was controlled using an open source framework called "Yet another drone." This framework allows developers to build applications for the AR.Drone 2.0 in Java [133]. Figure 7.8 represents a snapshot during the flight of the AR.Drone 2.0 to capture a real-time video streaming of lava fountain activity.

Figure 7.8 A snapshot during the flight of the AR.Drone 2.0 to capture a real-time video streaming of lava fountain activity.

The drone has three degrees of freedom to position the drone and three degrees for orientation (pitch, roll, and yaw) [133]. In order to communicate with the drone from a laptop, the user should first connect to the drone's WiFi. Also, the drone monitors battery voltage that is converted into a battery life percentage. Typically, the drone's battery life provides a flight time of 12 minutes while capturing streaming video in real-time. Figures 7.9a and 7.9b are screen shots for the GUI during the flight of the drone while detecting a nuclear explosion, and a pyroclastic density current, respectively.

(a)
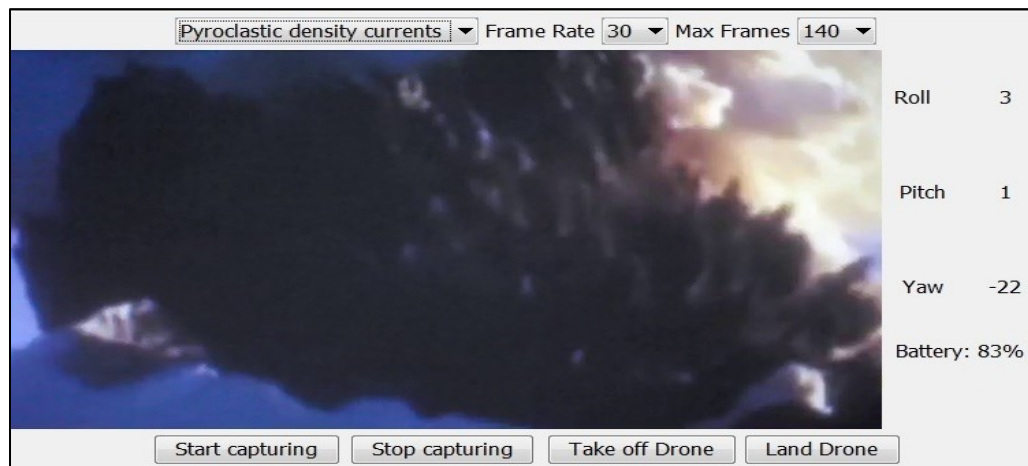
(b)

Figure 7.9 (a) Live video streaming for NC; (b) Live video streaming for PDC.

The number of frames for the testing phase of each experiment can be specified by the user. Hence, the drone will stop capturing automatically once the pre-defined value of the max frame count is reached. Figure 7.10 displays some of the video frames captured by the camera sensor at the front of AR.Drone 2.0, and streamed via WiFi to the laptop.
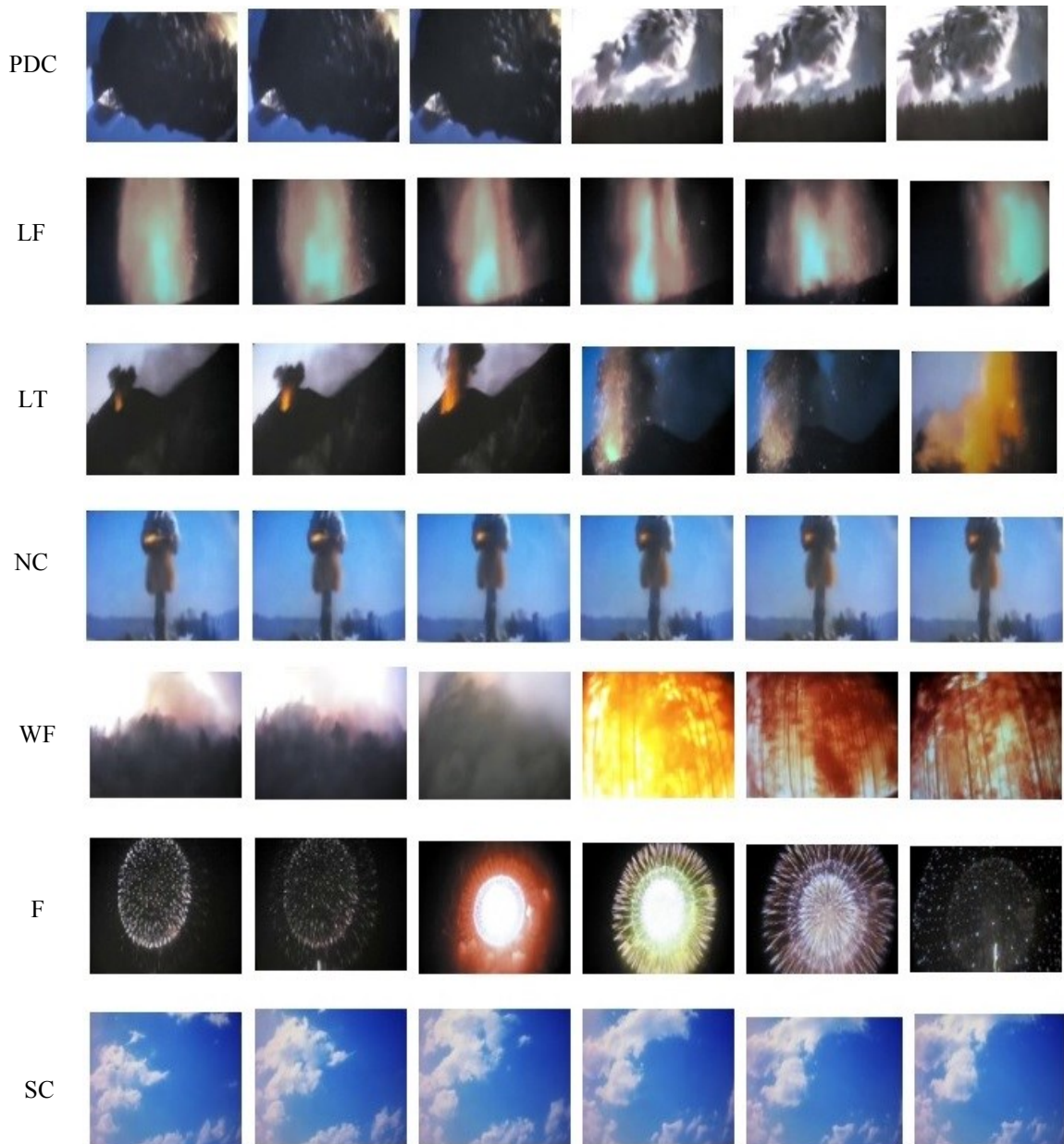
Figure 7.10 Some of the video frames captured by the camera sensor at the front of AR.Drone 2.0

As illustrated in Table 7.8, videos of the seven classes under consideration are listed. The frame rate of the drone's front camera was selected to be 30fps, and the max number of frames was set to 140 for each category for consistency. Furthermore, the resolution of retrieved frames by the drone was 640×360 pixels, and they were saved on the client device using JPEG file format. For the testing phase of the classification system, frames were resized to 64×64 pixels. Each frame was defined using the research methodology of extracting 400 features that were combined in one input vector and fed into the multiclass SVM with degree 3 polynomial kernel. A comparison between patterns of the proposed classification system in terms of accuracy (classification rate) is provided in Table 7.8.

Table 7.8 Comparison between patterns in terms of accuracy after capturing real-time test frames using the front camera of AR.Drone 2.0

Category	Frame rate	Resolution of captured frames	Max frames count	Frames resized during preprocessing	Features input vector	Accuracy
Video 1—PDC	30 fps	640 × 360	140	64 × 64	400	**100%**
Video 2—LF	30 fps	640 × 360	140	64 × 64	400	**100%**
Video 3—LT	30 fps	640 × 360	140	64 × 64	400	91.43%
Video 4—NC	30 fps	640 × 360	140	64 × 64	400	**100%**
Video 5—WF	30 fps	640 × 360	140	64 × 64	400	95.00%
Video 6—F	30 fps	640 × 360	140	64 × 64	400	**100%**
Video 7—SC	30 fps	640 × 360	140	64 × 64	400	**100%**

As a result, an average classification rate of 98.06% was achieved as compared to an average classification rate of 98.16% that were accomplished when video sequences were retrieved from computer folders by the classification system. The small difference in the classification rate, from 98.16% to 98.06% was due to the focal length of the drone's camera and its Field of View (FOV). Hence, PDC, LF, NC, F, and SC samples were classified correctly with 100% accuracy, followed by WF, and LT that accomplished a classification rate of 95.00% and 91.43%, respectively.

Furthermore, Table 7.9 demonstrates the confusion matrix for the multiclass degree-3 polynomial kernel SVM classifier where testing samples of 140 for each category were represented by 400 features. Consequently, WF samples were classified as if they belong to PDC, LF, and F, whereas the display of LT scenes results in misclassified samples among PDC, LF, and WF. Thus, evaluation results show the design of the proposed system is effective and robust.

Table 7.9 Confusion matrix for the multiclass degree-3 polynomial kernel SVM classifier for testing frames that were retrieved using the AR.Drone 2.0

Actual	Predicted results						
	PDC	LF	LT	NC	WF	F	SC
PDC (140)	**140**	0	0	0	0	0	0
LF (140)	0	**140**	0	0	0	0	0
LT (140)	6	4	**128**	0	2	0	0
NC (140)	0	0	0	**140**	0	0	0
WF (140)	4	2	0	0	**133**	1	0
F (140)	0	0	0	0	0	**140**	0
SC (140)	0	0	0	0	0	0	**140**

Typically, the complexity of any classification problem in the real-time outdoor experiments depends on the limitations, characteristics, and hardware complexity of the transducer such as the bandwidth, resolution, sensitivity, latency, distortion, and so forth. Therefore, the indoor environment is constrained, and in order to apply the proposed system in outdoor environments including the battlefield and the locations of volcanoes, powerful drone in terms of their ability to sustain in extreme weather conditions, having high resolution RGB color cameras, having long connectivity range, and having long battery life are needed. In addition, using the proposed research methodology in this dissertation, images were resized to 64×64 regardless of the resolution of the original frames captured by the drone's camera. Therefore, we conclude that the focal length of the drone's camera and its field of view (FOV) may affect the results in a real-time outdoor environment.

7.4 Statistical Power Analysis

In this section, statistical power analysis is performed to estimate the required minimum sample size for the experiment that is sufficient to attain adequate power, and test the alternative hypothesis. From the experimental results, it is concluded that one-against-one multiclass SVM with degree 3 polynomial kernel outperformed one-against-one multiclass SVM with degree 2 polynomial kernel in terms of the classification rate. In this regard, power analysis is used to prove this hypothesis. The power of a statistical test is the probability that the test will reject the null hypothesis when the null hypothesis is false by confirming the alternative hypothesis when the alternative hypothesis is true.

Consequently, the two-tailed test will be used, and the statistical hypothesis is given as follows:

H_0: $\mu_{\text{SVM (degree-3 polynomial kernel)}} = \mu_{\text{SVM (degree-2 polynomial kernel)}}$,

H_a: $\mu_{\text{SVM (degree-3 polynomial kernel)}} > \mu_{\text{SVM (degree-2 polynomial kernel)}}$,

Where $\mu_{\text{SVM (degree-3 polynomial kernel)}}$ is the classification rate of the one-against-one multiclass SVM with degree 3 polynomial kernel classifier, and $\mu_{\text{SVM (degree-2 polynomial kernel)}}$ is the classification rate of the one-against-one multiclass SVM with degree 2 polynomial kernel classifier. In other words, the classification rate of the one-against-one multiclass SVM with degree 3 polynomial kernel classifier is greater than the classification rate of the one-against-one multiclass SVM with degree 2 polynomial kernel classifier.

The significance of an observed difference is determined by the chosen level of significance (α). Commonly, 5% (0.05) or 1% (0.01) are used for α.

In order to determine the required sample size (n), three parameters are used in this decision as follows:

- The level of significance (α) that is used = 5%.
- The required power of the test (p) = 80%.
- The effect size is (d).

Based on the work of Cohen [134] that is illustrated in Table 7.10, we will be using the t-test on Means calculation with the effect size index "d" of a large set. The minimum required sample size is calculated using equation 15.

Table 7.10 Effect size values

	Effect size Index	Small	Medium	Large
t-test on Means	**d**	0.20	0.50	0.80
t-test on Correlations	r	0.10	0.30	0.50
F-test ANOVA	f	0.10	0.25	0.40
F-test regression	f²	0.02	0.15	0.35
Chi-Square Test	w	0.10	0.30	0.50

$$\text{Sample size (n)} = \frac{N \times p(1-p)}{\left[\left[N-1 \times \left(\frac{d^2}{z^2}\right)\right] + p(1-p)\right]} \quad (15)$$

where N= 5327, which is the general population size of all possible requests,

p =80% = 0.8, which is the required power of the test. Thus, p (1-p) = 0.8 (0.2) = 0.16,

d is the level of significance, so d = 5%, d²= (0.05)² = 0.0025, and

z is the t-value of α/2, where α= 5%. To find z α/2, we need to calculate α/2 as follows:

$\frac{\alpha}{2} = \frac{0.05}{2} = 0.025$. Therefore, by looking up the value for z×0.025 in the t-table, we find

that: z×0.025 = 1.96, and $z^2 = 3.842$,

Thus, sample size (*n*) can be calculated as:

$$\text{Sample size (n)} = \frac{5327 \times 0.16}{\left[\left[5326 \times \left(\frac{0.0025}{3.842}\right)\right] + 0.16\right]} = \frac{852.32}{3.47 + 0.16} = \frac{852.32}{3.63} \approx 235$$

Then, the parameters below are computed in order to make the decision of the hypothesis.

$$\text{Mean } (\overline{X}) = \frac{\Sigma x}{n} = 0.9085 \tag{16}$$

$$\text{Variance } (\sigma^2) = \frac{\Sigma(x - \bar{x})^2}{n} = 0.083 \tag{17}$$

$$\text{Standard Deviation } (\sigma) = \sqrt[2]{\sigma^2} = 0.289 \tag{18}$$

$$\text{Degree of freedom } (d.f) = n - 1 = 235 - 1 = 234 \tag{19}$$

$$\text{Confidence Level } (1 - \alpha) = 0.95 \tag{20}$$

$$\text{Significance level } (\alpha) = 0.05 \tag{21}$$

$$\text{Critical t } = \text{TINV } (\alpha, d.f) = \text{TINV } (0.05, 234) = 1.97 \tag{22}$$

$$\text{Standard Error } (Sx) = \frac{\sigma}{\sqrt{n}} = \frac{0.289}{\sqrt{235}} = \frac{0.289}{15.3} = 0.019 \tag{23}$$

$$\text{Lower limit} = \overline{X} - \text{Critical t} \times Sx = 0.9085 - (1.97 \times 0.019) = 0.87 \tag{24}$$

$$\text{Upper limit} = \overline{X} + \text{Critical t} \times Sx = 0.9085 + (1.97 \times 0.019) = 0.95 \tag{25}$$

$$\text{Hypothesis } (Ho) = 50\% \tag{26}$$

$$\text{t Value} = \frac{\overline{X} - Ho}{Sx} = \frac{0.9085 - 0.5}{0.019} = \frac{0.4085}{0.019} = 21.5 \tag{27}$$

To reach our conclusion, the t value and critical t value are used. If the t value is greater than the critical t (probability that Ho is true is low), Ho is rejected. In this test: t value (21.5) > critical t (1.97). This means Ho is rejected and Ha is accepted. Using the power analysis reveals that a sample set of 235 is sufficient to prove that the one-against-one multiclass SVM with degree 3 polynomial kernel classifier has better efficiency than one-against-one multiclass SVM with degree 2 polynomial kernel. The used sample is sufficient to prove the stated hypothesis with a high degree of accuracy and confidence.

CHAPTER 7: CONCLUSION

The safety of citizens during explosion occurrences is the product of collaborative efforts by scientists, experts, governments, military, local agencies, and qualified emergency professionals. Thus, suitable actions and procedures can be initiated to control the explosion risks. In this dissertation, we present a novel taxonomy of explosion phenomena. Consequently, we propose the design of a novel computer vision-based framework for supervised classification of volcanic eruptions and nuclear explosions. Moreover, we collected a new dataset of color images referred to as VNEX. The totality of VNEX is $10,654$ samples that includes the following patterns: pyroclastic density currents, lava fountains, lava and tephra fallout, nuclear explosions, wildfires, fireworks, and sky clouds.

Through our experience and experiments, we determine that VNEX samples are complex. Nevertheless, the one-against-one multiclass SVM with degree 3 polynomial kernel produced the highest classification rate of 90.85% when employed on $5,327$ samples of VNEX testing set, and a reasonable execution time of approximately 117ms was consumed to classify one test sample. This classifier outperformed several multiclass approaches such as Euclidean distance, correlation, KNN, and the MPL classifier. More specifically, we represent the VNEX samples using several feature extraction approaches including: intensity levels, YC_bC_r color model, Radix-2 FFT, and ULBP. Then, we compute the PCA method to calculate the most significant 100 eigenvectors and the corresponding eigenvalues on each feature class. Furthermore, we combine these features

in one input vector of length 400. Hence, these encapsulated features in a single input vector are intuitively invariant in terms of translation, illumination, scale, and rotation providing a meaningful insight into VNEX samples. As a result, these discriminative features have led the multiclass degree-3 polynomial kernel SVM classification model to cast a proper decision to predict the class label for each unknown test sample.

Moreover, the proposed research methodology was evaluated on 980 frames of YouTube video sequences for the seven scenarios of the respective defined classes that were retrieved from computer folders. Results show that a high classification rate of 98.16% was achieved. In addition, we conducted experiments where a drone was flown to collect real-time observations while playing the same YouTube video sequences in an indoor environment. Evaluation results show a classification rate of 98.06% was achieved. Thus, we conclude that the proposed framework is robust and reliable.

7.1 Future Work

The proposed framework is pluggable and scalable. Thus, we discuss the future trends for implementing advanced solutions to improve the classification rate in the context of the seven categories.

Our vision for future improvements involves applying different deep learning architectures to achieve supervised classification of the VNEX dataset. In this context, the autoencoder neural network can be employed. The Autoencoder is a nonlinear model that generalizes the PCA technique. It utilizes an adaptive, multilayer network called "encoder" in order to map the high dimensional data into a lower dimensional code. Furthermore,

there is a similar "decoder" network that performs data recovery from the code [135]. Thus, the autoencoder sets the target values to be equal to the input values. During the learning phase, the autoencoder discovers weights to identify useful low-level features such as edges, primitive shapes, and more complex shapes. Then, the autoencoder combines them into a high feature space, and automatically learn the best nonlinear hyperplane that separate the input data into regions or categories.

Another alternative deep learning architecture that can be applied on the VNEX dataset called the Convolutional Neural Network (CNN). Recently, CNN has accomplished a remarkable performance in the computer vision field and has solved complex problems successfully [136-140]. Typically, the CNN comprises of numerous layers: (1) convolutional layers, (2) pooling layers, and (3) fully-connected layers. By fine-tuning the CNN architecture design, learning a representation of the discriminative features of the domain of our target application can be achieved automatically.

Furthermore, the Recurrent Neural Networks (RNN) using the Long Short-Term Memory (LSTM) architecture can be adopted to perform a supervised sequence learning on a dataset of videos for the respective seven classes. This model can be considered a convenient approach to monitor an explosion activity over time because of its capability on the prediction of time series, and context dependent pattern classification tasks [141-143].

In addition to utilizing color images of VNEX dataset, a classification system based on extracting thermal descriptors from thermal infrared images of the seven classes can be tailored and implemented [144].

REFERENCES

[1] S. Abusaleh, A. Mahmood, K. Elleithy, and S. Patel, "A Novel Vision-Based Classification System for Explosion Phenomena," *In J. Imaging*, vol. 3, no.2, Apr. 2017.

[2] J. Gyakum, and J. Stix, "Natural Disasters," McGill University on edX, Montreal, Canada, Free online course conducted from Jan. 14 – Apr. 11, 2015, Accessed on: Oct. 1, 2017. [Online]. Available: https://courses.edx.org

[3] American Institute of Chemical Engineers (AlChE) Staff, Center for Chemical Process Safety (CCPS) Staff. Guidelines for Evaluating Process Plant Buildings for External Explosions and Fires. Appendix A-Explosion and Fire Phenomena and Effects; American Institute of Chemical Engineers, JohnWiley & Sons, Inc.: Hoboken, NJ, USA, 1996.

[4] P. P. Craig, and J. A. Jungerman, "Nuclear arms race: technology and society," 2nd ed., University of California. Davis. McGraw-Hill. USA, 1990.

[5] H. Habush, and S.C. Rottier, "Expion Attorneys," Accessed on Oct. 1, 2017. [Online] Available: http://www.habush.com/practice-areas/personal-injury/explosion/

[6] M. Blackett, "An Overview of Infrared Remote Sensing of Volcanic Activity," *In J. Imaging*, vol. 3, no. 2, Apr. 2017.

[7] S. Self, "The effects and consequences of very large explosive volcanic eruptions," *In Philos. Trans. R. Soc. Lond. A: Math. Phys. Eng. Sci.*, 364(1845), pp. 2073–2097, 2006.

[8] National Geographic Society, "Volcanic Ash," Accessed on Oct. 1, 2017. [Online]
    Available: https://www.nationalgeographic.org/encyclopedia/volcanic-ash/

[9] U.S. Department of the Interior, U.S. Geological Survey, Volcano Hazards Program,
    "Lava Flows and Their Effects," Modified on May 24, 2010. [Online] Available:
    http://volcanoes.usgs.gov/hazards/lava/ (accessed on24 September 2016).

[10] U.S. Department of the Interior, U.S. Geological Survey, Volcano Hazards Program,
    "Temperatures at the Surface Reflect Temperatures Below the Ground," Modified on:
    Jan. 7, 2016, Accessed on: Oct. 1, 2017. [Online]. Available:
    https://volcanoes.usgs.gov/vhp/thermal.html

[11] F. S. Marzano, M. Lamantea, M. Montopoli, S. Di Fabio, and E. Picciotti, "The
    Eyjafjöll explosive volcanic eruption from a microwave weather radar perspective," *In
    Atmos. Chem. Phys.*, vo.11, no. 18, pp.9503-9518, 2011.

[12] F.S. Marzano, "Remote Sensing of Volcanic Ash Cloud During Explosive Eruptions
    Using Ground-Based Weather Radar Data Processing," *In IEEE Signal Processing
    Magazine*, vol. 28, no. 2, Mar. 2011.

[13] U.S. Department of the Interior, U.S. Geological Survey, Volcano Hazards Program,
    "Using Digital Elevation Models (DEMs) to Map Changes in Topography," Modified
    on: May 30, 2017, Accessed on: Oct. 1, 2017. [Online]. Available:
    https://volcanoes.usgs.gov/volcanoes/st_helens/st_helens_monitoring_109.html

[14] L. Wang, M. J. Alexander, "Global estimates of gravity wave parameters from GPS
    radio occultation temperature data," *In J. Geophys. Res.*, Vol.115, D21122, Nov. 2010.

[15] H. Dickinson, and P. Tamarkin, "Systems for the Detection and Identification of Nuclear Explosions in the Atmosphere and in Space," *In Proc. IEEE 1965*, vol. 53, no. 12, pp.1921–1934, Dec. 1965.

[16] U.S. Department of Labor, "OSHA Fact Sheet- Hazard Alert: Combustible Dust Explosion," DSG 12/2014, Accessed on Oct. 1, 2017. [Online] Available: https://www.osha.gov/OshDoc/data_General_Facts/OSHAcombustibledust.pdf

[17] NASA Safety Center, "System Failure Case Studies," vol. 2, Special Issue, January 2008.

[18] R. Lopes, "The Volcano Adventure Guide," Cambridge University Press: Cambridge, UK, 2005.

[19] F. R. Spellman, "Geography for Nongeographers," Government Institutes, The Scarecrow Press, Inc.: Lanham, Toronto, Plymouth, UK, 2010.

[20] M. J. Branney, and P. Kokelaar, "Pyroclastic Density Currents and the Sedimentation of Ignimbrites," The Geological Society of London, London, UK, 2002.

[21] T. Shea, L. Gurioli, B.F. Houghton, R. Cioni, and K.V. Cashman, "Column collapse and generation of pyroclastic density currents during the A.D. 9 eruption of Vesuvius: The role of pyroclast density," In Geology, 39(7), pp. 695-698, Jul. 2011.

[22] R. Sulpizio, P. Dellino, D. M. Doronzo, and D. Sarocchi, "Pyroclastic density currents: state of the art and perspectives," *In J. Volcanol. Geotherm. Res.*, 283, pp. 36–65, Aug. 2014.

[23] G.E. Bogoyavlenskaya, O.A. Braitseva, I.V. Melekestsev, V.Y. Kiriyanov, and C.D. Miller, "Catastrophic eruptions of the directed-blast type at Mount St. Helens, Bezymianny and Shiveluch volcanoes," In J. Geodyn., 3, pp. 189–218, 1985.

[24] I.A. Nairn, and S. Self, "Explosive eruptions and pyroclastic avalanches from Ngauruhoe in February 1975," *In J. Volcanol. Geother. Res.*, 3, pp. 39–60, Mar. 1978.

[25] Smithsonian Institution. National Museum of Natural History, Global Volcanism Program, "Types and Processes Gallery," Accessed on: Oct. 1, 2017. [Online]. Available: http://volcano.si.edu/learn_galleries.cfm?p=9

[26] N. Lardot, "Pyroclastic flows at Mayon Volcano.jpg," U.S Department of the Interior, U.S. Geological Survey, Uploaded on: Oct. 2006. Accessed on: Oct. 1, 2017. [Online] Available:

https://commons.wikimedia.org/wiki/File:Pyroclastic_flows_at_Mayon_Volcano.jpg

[27] B. Voight. National Science Foundation (NSF), "Soufriere Hills Volcano Erupting," Accessed on Oct. 1, 2017. [Online]. Available:

https://www.nsf.gov/news/mmg/mmg_disp.jsp?med_id=64852&from=img

[28] T. Pfeiffer, Volcano Discovery, "Bromo Volcano (Tengger Caldera), Indonesia," Modified on: Sep. 17, 2004, Accessed on: Oct. 1, 2017.

[Online]. Available:

http://www.decadevolcano.net/volcanoes/indonesia/tengger_caldera/bromo.htm

[29] U.S. Department of the Interior, U.S. Geological Survey, Volcano Hazards Program, "Glossary- Eruption Column," Modified on: Jul. 28, 2015, Accessed on: Oct. 1, 2017.

[Online]. Available: http://volcanoes.usgs.gov/vsc/glossary/eruption_column.html

[30] Volcanic Ashfall Impacts Working Group, U.S Department of the Interior, U.S. Geological Survey, "Volcanic Ash Impacts and Mitigation – Mt St Helens 1980," Modified on: Dec. 17, 2015, Accessed on: Oct. 1, 2017. [Online]. Available: https://volcanoes.usgs.gov/volcanic_ash/mount_st_helens_1980.html

[31] "TVNZ One News—Undersea Volcano Eruption 09 [Tonga]," Uploaded on: Mar. 19, 2009, Accessed on: Oct. 1, 2017. [Online]. Available: https://www.youtube.com/watch?v=B1tjIihHgco

[32] U.S. Department of the Interior, U.S. Geological Survey, Volcano Hazards Program, "Glossary-Effusive Eruption," Modified on: Jul. 10, 2015, Accessed on: Oct. 1, 2017, [Online]. Available: https://volcanoes.usgs.gov/vsc/glossary/effusive_eruption.html

[33] U.S. Department of the Interior, U.S. Geological Survey, Volcano Hazards Program, Hawaiian Volcano Observatory (HVO), "A recap of the Kamoamoa fissure eruption on its third anniversary," Modified on: May 30, 2017, Accessed on: Oct. 1, 2017. [Online]. Available:

https://volcanoes.usgs.gov/observatories/hvo/hvo_volcano_watch.html?vwid=218

[34] U.S. Department of the Interior, U.S. Geological Survey, Volcano Hazards Program, Hawaiian Volcano Observatory, "Puʻu ʻŌʻō and the Current Eruption of Kīlauea," Modified on: May 7, 2017, Accessed on: Oct. 1, 2017. [Online]. Available:

https://volcanoes.usgs.gov/volcanoes/kilauea/geo_hist_1983.html

[35] J. Seach, Volcano Live, "Lava Colour | John Seach," Accessed on: Oct. 1, 2017, [Online]. Available: http://www.volcanolive.com/lava2.html

[36] B. Pipkin, D.D. Trent, R. Hazlett, and P. Bierman, "Geology and the environment," 6th ed., Brooks/Cole- Cengage Learning: Belmont, CA, USA, 2010.

[37] T. Pfeiffer, Volcano Discovery, "ETNA VOLCANO PHOTOS. PART I," Modified on Jan. 21, 2004, Accessed on: Oct. 1, 2017. [Online]. Available:

http://www.decadevolcano.net/photos/etna0701_jpg/etna_2828.jpg

[38] R. Tilling, C. Heliker, and D. Swanson, "Eruptions of Hawaiian Volcanoes – Past, Present, and Future (General Information Product 117)," 2nd ed., Reston, VA, USA: U.S. Department of the Interior, U.S. Geological Survey, 2010.

[39] D. Karnå, Wikimedia Commons, "Eyjafjallajökull major eruption 20100510.jpg," Uploaded on: Jun. 2, 2010, Accessed on: Oct. 1, 2017. [Online]. Available: https://commons.wikimedia.org/wiki/File:Eyjafjallaj%C3%B6kull_major_eruption_20100510.jpg

[40] T. Pfeiffer, Volcano Discovery, "ETNA VOLCANO PHOTOS," Part 2, Modified on Jan. 31, 2004, Accessed on: Oct. 1, 2017. [Online]. Available: http://www.decadevolcano.net/photos/etna1002/etna_28732.jpg

[41] How Volcanoes Work, "Tephra and Pyroclastic Rocks," Accessed on: Oct. 1, 2017, [Online]. Available: http://www.geology.sdsu.edu/how_volcanoes_work/Tephra.html

[42] "Operation Crossroads 1946," Modified on: Dec. 16, 2001, Accessed on: Oct. 21, 2017. [Online]. Available: http://nuclearweaponarchive.org/Usa/Tests/Crossrd.html

[43] The National Security Archive, The George Washington University, "The Atomic Tests at Bikini Atoll, July 1946," 1995-2017, Accessed on: Oct. 1, 2017. [Online]. Available:
http://nsarchive2.gwu.edu/nukevault/ebb553-70th-anniversary-of-Crossroads-atomic-tests/

[44] Trinity Atomic Web Site, Gallery of Test Photos, 1995–2003, Accessed on: Oct. 1, 2017. [Online]. Available: http://www.abomb1.org/testpix/index.html

[45] U.S. Environmental Protection Agency, U.S. Forest Service, U.S. Centers for Disease Control and Prevention, and California Air Resources Board, "Wildfire Smoke – A guide for Public Health Officials," Revised on: May 2016, Accessed on: Oct. 1, 2017. [Online]. Available:

https://www3.epa.gov/airnow/wildfire_may2016.pdf

[46] B.J. Alan Company, "Fireworks University - Fireworks Glossary," Accessed on: Oct. 1, 2017. [Online]. Available:

http://www.fireworks.com/fireworks-university/fireworks-glossary/

[47] The Fireworks Alliance, Glossary of Fireworks Terms, Powered by Accelix. Accessed on: Oct. 1, 2017. [Online]. Available:

http://www.fireworksalliance.org/cgi-bin/viewpage.pl?p=glossary#w

[48] J. A. Conkling, and C.J. Mocella, "Chemistry of Pyrotechnics: Basic Principles and Theory," 2nd ed., 2010, CRC Press. Taylor & Francis Group. Boca Raton. London. New York.

[49] National Aeronautics and Space Administration (NASA), "S'COOL Cloud Identification Chart," EW-2004-10-04-LaRC, Accessed on: Oct. 1, 2017. [Online]. Available: http://science-edu.larc.nasa.gov/SCOOL/pdf/Cloud_ID.pdf

[50] National Weather Service, National Oceanic and Atmospheric Administration, Department of Commerce, "Ten Basic Cloud Types," Updated on: Mar. 14, 2013, Accessed on: Oct. 1, 2017. [Online]. Available:

http://www.srh.noaa.gov/srh/jetstream/clouds/cloudwise/types.html

[51] M. Roth, and R. Guritz, "Visualization of volcanic ash clouds," *In IEEE Computer Graphics and Applications*, vol. 15, no. 4, pp. 34-39, Jul. 1995.

[52] B. Ando, "Let's measure volcanic phenomena," *In IEEE Instrumentation & Measurement Magazine*, vol. 5, no. 4, pp. 65-70, Dec. 2002.

[53] A. Nugroho, and E.Winarko, "Geographical Information System and Web Service Implementation for Volcanic Eruptions Geologic Disasters Surveillance, Monitoring, and Mitigation System," *In IEEE Proceedings of the 2011 International Conference on Electrical Engineering and Informatics*, pp. 1-5, Jul. 2011.

[54] G. Werner-Allen, J. Johnson, M. Ruiz, J. Lees, and M. Welsh, "Monitoring volcanic eruptions with a wireless sensor network," *In Proceedings of the Second European Workshop on Wireless Sensor Networks (EWSN'05)*, pp.108-120, 2005.

[55] G. Werner-Allen, K. Lorincz, M. Welsh, O. Marcillo, J. Johnson, M. Ruiz, and J. Lees, "Deploying a Wireless Sensor Network on an Active Volcano," *In Data-Driven Applications in Sensor Networks (Special Issue) - IEEE Internet Computing. (March/April)*, vol.10, no. 2, pp.18-25, Mar. 2006.

[56] R. Tan, G. Xing, J. Chen, W.Z. Song, and R. Huang, "Fusion-based volcanic earthquake detection and timing in wireless sensor networks," *In ACM Trans. Sens. Netw.*, vol. 9, no. 2, pp. 1–25, Mar. 2013.

[57] M. Jinguuji, and S. Ehara, "Quantitative estimation of erupted volcanic ash by using satellite image," *In IEEE International Geoscience and Remote Sensing Symposium (IGARSS)*, pp. 1345-1347, Jul. 1998.

[58] S&TR Staff, Lawrence Livermore National Laboratory, "Monitoring Earth's Subsurface from Space," pp. 4-11, Apr. 2005.

[59] B. Andò, and E. Pecora, "A measurement tool for investigating the volcanic activity," *In IEEE Instrumentation and Measurement Technology Conference*, pp. 2039-2043, May 2005.

[60] H. Langer, S. Falsaperla, M. Masotti, R. Campanini, S. Spampinato, and A. Messina, "Synopsis of supervised and unsupervised pattern classification techniques applied to volcanic tremor data at Mt Etna, Italy," *In Geophys. J. Int.*, vol. 178, no. 2, pp. 1132–1144, Aug. 2009.

[61] A.S. Iyer, F.M. Ham, and M. A. Garces, "Neural classification of infrasonic signals associated with hazardous volcanic eruptions," *In IEEE International Joint Conference on Neural Networks*, San Jose, CA, USA, pp. 336–341, Jul. 31–Aug. 5, 2011.

[62] M. Picchiani, M. Chini, S. Corradini, L. Merucci, P. Sellitto, F. Del Frate, and S. Stramondo, "Volcanic ash detection and retrievals using MODIS data by means of neural networks," *In Atmos. Meas. Tech.*, 4, pp. 2619–2631, Dec. 2011.

[63] F.S. Marzano, S. Barbieri, G. Vulpiani, and W.I. Rose, "Volcanic Ash Cloud Retrieval by Ground-Based Microwave Weather Radar," *In IEEE Transactions on Geoscience and Remote Sensing*, vol. 44, no. 11, pp. 3235-3246, Oct. 2006.

[64] L. Boccia, G. Di Massa, and I. Venneri, "L-Band array for ground-based remote sensing of volcanic eruptions," *In IET Microwaves, Antennas & Propag.*, vol. 4, no. 12, pp. 2062-2068, Dec. 2010.

[65] N. Lindgen, "Earthquake or explosion? The science of nuclear test detection," *In IEEE Spectr.*, vol. 3, no 8, pp. 66–75, Aug. 1966.

[66] R. Wicander, and J.S. Monroe, "Essentials of Physical Geology," 5th ed., Brooks/Cole-Cengage Learning: Belmont, CA, USA, 2009.

[67] S.C. Moran, J.T. Freymueller, R.G. Lahusen, K.A. Mcgee, M.P. Poland, J.A. Power, D.A. Schmidt, D.J. Schneider, G. Stephens, C.A. Werner, and R. A. White, "Instrumentation Recommendations for Volcano Monitoring at U.S. Volcanoes under the National Volcano Early Warning System," Scientific Investigation Report 2008– 5114, Department of the Interior, U.S. Geological Survey: Reston, VA, USA, 2008.

[68] U.S. Department of the Interior, U.S. Geological Survey, Volcano Hazards Program, "Comprehensive monitoring provides timely warning of volcano reawakening," Modified on: Mar. 17, 2016, Accessed on: Oct. 1, 2017. [Online]. Available: https://volcanoes.usgs.gov/vhp/monitoring.html

[69] U.S. Department of the Interior, U.S. Geological Survey, Volcano Hazards Program, "Movement on the Surface Provides Information About the Subsurface," Modified on: Oct. 27, 2005, Accessed on: Oct. 1, 2017. [Online]. Available: https://volcanoes.usgs.gov/vhp/deformation.html

[70] C.J. Ammon, and T. Lay, "USArray Data Quality," *In Nuclear Test Illuminates, EOS, Transaction American Geophysical Union,* Wiley Online Library, Jan. 23, 2007, vol. 88, no.4, pp.37–52, Accessed on: Oct. 1, 2017. [Online]. Available: http://onlinelibrary.wiley.com/doi/10.1029/2007EO040001/pdf

[71] IRIS Data Management Center, EarthScope, National Science Foundation, "Transportable Array," Accessed on: Oct. 1, 2017. [Online]. Available: http://www.usarray.org/researchers/obs/transportable

[72] M. Turk, and A. Pentland, "Eigenfaces for Recognition," J. Cogn. Neurosci., vol. 3, no. 1, pp. 71–86, 1991.

[73] K. Jack, "Video Demystified: A Handbook for the Digital Engineer," 3rd ed., LLH Technology Publishing: Eagle Rock, VA, USA, 2001.

[74] U.S. Department of the Interior, U.S. Geological Survey, Volcano Hazards Program, "Explosive eruption," Modified on: Aug. 21, 2015, Accessed on: Oct. 1, 2017. [Online]. Available: https://volcanoes.usgs.gov/vsc/glossary/explosive_eruption.html

[75] U.S. Department of the Interior, U.S. Geological Survey, Volcano Hazards Program, "1959 Kīlauea Iki Eruption," Modified on: Apr. 13, 2017, Accessed on: Oct. 1, 2017. [Online]. Available: https://volcanoes.usgs.gov/volcanoes/kilauea/geo_hist_kilauea_iki.html

[76] J. Newman, Wikimedia Commons, "File:Zaca3.jpg," Uploaded on: Oct. 17, 2007, Accessed on: Oct. 1, 2017. [Online]. Available: https://commons.wikimedia.org/wiki/File:Zaca3.jpg

[77] PEXELS Blog, Accessed on: Oct. 1, 2017. [Online]. Available: https://www.pexels.com/

[78] Saperaud, Wikimedia Commons, "File:Sc 2.jpg," Uploaded on: Sep. 3, 2004, Accessed on Oct. 1, 2017. [Online]. Available:
https://commons.wikimedia.org/wiki/File:Sc_2.jpg

[79] B. Payette, "Color Space Convertor: R'G'B' to Y'CbCr," Xilinx, XAPP637 (v1.0), Sep. 2002, Accessed on: Oct. 1, 2017. [Online]. Available:
http://application-notes.digchip.com/077/77-42796.pdf

[80] S.W. Smith, "The Scientist and Engineer's Guide to Digital Signal Processing. Chapter 12: The Fast Fourier Transform," 1997-2011, California Technical Publishing: San Diego. CA. USA, Accessed on: Oct. 1, 2017, [Online]. Available: http://www.dspguide.com/ch12.htm

[81] S. Rapuano, and F.J. Harris, "An Introduction to FFT and Time Domain Windows," *In IEEE Instrumentation & Measurement Magazine*, 10 (6). Dec. 2007, pp. 32-44.

[82] S. Nagabhushana, "Computer Vision and Image Processing," 1st ed., New Age International (P) Ltd.: New Delhi, India, 2005.

[83] J.G. Proakis, D.G. Manolakis, "Digital Signal Processing: Principles, Algorithms, and Applications," 3rd ed., Prentice Hall, Inc: Upper Saddle River, NJ, USA, 1996.

[84] D. Huang, C. Shan, M. Ardabilian, Y. Wang, and L. Chen, "Local Binary Patterns and Its Application to Facial Image Analysis: A Survey," *In IEEE Transactions on Systems, Man, and Cybernetics, Part C: Applications and Reviews*, vol. 41, no. 6, pp. 765-781, Nov. 2011.

[85] L. Ali, T. Kasetkasem, F. G. Khan, T. Chanwimaluang, and H. Nakahara, "Identification of inpainted satellite images using evalutionary artificial neural network (EANN) and k-nearest neighbor (KNN) algorithm," *In 2017 8th International Conference of Information and Communication Technology for Embedded Systems (IC-ICTES)*, May 2017.

[86] C.J.C. Burges, "A Tutorial on Support Vector Machines for Pattern Recognition," *In Data Mining and Knowledge Discovery*, Kluwer Academic Publishers: Hingham, MA, USA, vol. 2, no. 2, Jun. 1998, pp. 121–167.

[87] C.W. Hsu, C.C. Chang, and C.J. Lin, "A Practical Guide to Support Vector Classification," 2010, Accessed on: Oct. 1, 2017. [Online]. Available: http://www.csie.ntu.edu.tw/~cjlin/papers/guide/guide.pdf

[88] J.C. Platt, "Fast Training of Support Vector Machines Using Sequential Minimal Optimization," *In Advances in Kernel Methods—Support Vector Learning*, B.

Scholkopf, C.J.C. Burges, and A.J. Smola. Eds., MIT Press. Cambridge, MA, USA, 1998.

[89] R.C. Gonzalez, and R.E. Woods, "Digital Image Processing," 3rd ed., 2008, Prentice Hall. Upper Saddle River. NJ.

[90] J.B. Judd, USGS, Updated on: May 1, 1997, Accessed on: Oct. 1, 2017. [Online]. Available: https://pubs.usgs.gov/gip/hawaii/page29.html

[91] T. Pfeiffer, Volcano Discovery, "ETNA VOLCANO PHOTOS," PART I, Accessed on: Oct. 1, 2017. [Online]. Available:

http://www.decadevolcano.net/photos/etna0701_jpg/etna_2834.jpg

[92] M. Jastremski, Wikimedia Commons, "File:Cumulus clouds in fair weather.jpeg," Uploaded on: Jul. 10, 2005, Accessed on: Oct. 1, 2017. [Online]. Available:

https://commons.wikimedia.org/wiki/File:Cumulus_clouds_in_fair_weather.jpeg

[93] U.S. Geological Survey, Accessed on: Oct. 1, 2017. [Online]. Available: https://www.usgs.gov/

[94] Wikimedia Commons, Accessed on: Oct. 1, 2017. [Online]. Available: https://commons.wikimedia.org/wiki/Main_Page

[95] T. Pfeiffer, Volcano Adventures, Accessed on: Oct. 1, 2017. [Online]. Available: https://www.volcano-adventures.com/es/about_us.html

[96] T. Pfeiffer, Volcano Discovery, Accessed on: Oct. 1, 2017. [Online]. Available: http://www.decadevolcano.net/index.htm

[97] Department of Commerce, National Oceanic and Atmospheric Administration, and National Weather Service, "Clouds-Introduction to clouds," Accessed on: Oct. 1, 2017. [Online]. Available: http://www.weather.gov/

[98] R. Hipschman, "Exploratorium," Full-Spectrum Science with Ron Hipschman: Fireworks. Accessed on: Oct. 1, 2017. [Online]. Available: http://www.exploratorium.edu/visit/calendar/fullspectrum-science-ron-hipschman-fireworks-june-22-2014

[99] Onet.Blog. Copyright 1996-2016. Accessed on: Oct. 1, 2017. [Online]. Available: http://wulkany-niszczycielska-sila.blog.onet.pl/page/2/

[100] U.S. Department of the Interior, U.S. Geological Survey, Volcano Hazards Program, "Pyroclastic flows move fast and destroy everything in their path," Modified on: Feb. 12, 2016, Accessed on: Oct. 1, 2017. [Online]. Available: https://volcanoes.usgs.gov/vhp/pyroclastic_flows.html

[101] U.S. Department of the Interior, U.S. Geological Survey, Volcano Hazards Program, "Explosive eruptions produce multiple hazards," Modified on: May 10, 2017, Accessed on: Oct. 1, 2017. [Online]. Available: https://volcanoes.usgs.gov/observatories/hvo/hawaii_explosive_eruptions.html

[102] R. Clucas, U.S. Department of the Interior, U.S. Geological Survey, "Volcanoes of the Wrangell Mountains and Cook Inlet Region, Alaska-Selected Photographs–Album," Photograph was taken on Apr. 21, 1990, Accessed on: Oct. 1, 2017. [Online]. Available: http://web.archive.org/web/20051111095409/http://wrgis.wr.usgs.gov/dds/dds-39/album.html

[103] A. Sauter, OCEAN EXPLORER, U.S. Office of Ocean Exploration and Research, National Oceanic and Atmospheric Administration, U.S. Department of Commerce,

Revised on Aug. 26, 2010. Accessed on: Oct. 1, 2017. [Online]. Available: http://oceanexplorer.noaa.gov/explorations/03fire/logs/anatahan/media/fig1.html

[104] Itu, Wikimedia Commons, "File:Calbuco (17071015700).jpg," Uploaded on Apr. 25, 2015, Accessed on: Oct. 1, 2017. [Online]. Available: https://commons.wikimedia.org/wiki/File:Calbuco_(17071015700).jpg

[105] Paginario, Wikimedia Commons, "File:Erupcion guagua rgb.jpg," Uploaded on: Sep. 21, 2009, Accessed on: Oct. 1, 2017. [Online]. Available:

https://commons.wikimedia.org/wiki/File:Erupcion_guagua_rgb.jpg

[106] R. Russell, Alaska Volcano Observatory, U.S. Geological Survey, "IMAGE 428," Modified on: Dec. 2, 2016, Accessed on: Oct. 1, 2017. [Online]. Available: https://avo.alaska.edu/images/image.php?id=428

[107] G.E. Sigvaldason, Nordic Volcanological Institute, Reykjavik, Iceland, "USGS - Lava fountains," Modified on: May 5, 1999, Accessed on: Oct. 1, 2017. [Online]. Available: https://pubs.usgs.gov/gip/dynamic/Krafla.html

[108] T. Pfeiffer, Volcano Discovery, "Erta Ale volcano Nov 2010: lava fountains," Accessed on: Oct. 1, 2017. [Online]. Available:

https://www.volcanodiscovery.com/photos/erta-ale/nov10/lava-fountains.html

[109] T. Pfeiffer, Volcano Discovery, "STROMBOLI TREKKING," Accessed on: Oct. 1, 2017. [Online]. Available:

https://www.volcanodiscovery.com/stromboli/climbing/tour.html

[110] T. Pfeiffer, Volcano Discovery, "KILAUEA VOLCANO SPECIAL," Accessed on: Accessed on: Oct. 1, 2017. [Online]. Available:

https://www.volcanodiscovery.com/es/hawaii/kilauea_volcano_special.html

[111] T. Pfeiffer, Volcano Discovery, "Photos of volcanoes- Bárdarbunga," Accessed on:

Oct. 1, 2017. [Online]. Available:

https://www.volcanodiscovery.com/photos/volcanoes.html

[112] T. Pfeiffer, Volcano Discovery, "ETNA VOLCANO PHOTOS," Part 1, Accessed

on: Oct. 1, 2017. [Online]. Available:

http://www.decadevolcano.net/photos/etna1002_1.htm

[113] T. Pfeiffer, Volcano Discovery, "ETNA VOLCANO PHOTOS," Part 3, Accessed

on: Oct. 1, 2017. [Online]. Available:

http://www.decadevolcano.net/photos/etna1002_3.htm

[114] T. Pfeiffer, Volcano Discovery, "ETNA VOLCANO PHOTOS," Part 2, Accessed

on: Oct. 1, 2017. [Online]. Available: http://www.decadevolcano.net/photos/etna1002_2.htm

[115] T. Bulyonkova, Wikimedia Commons, "File:Yugansky nature reserve fire

(7938021666).jpg," Uploaded on: Aug. 19, 2013, Accessed on:

Oct. 1, 2017. [Online]. Available:

https://commons.wikimedia.org/wiki/File:Yugansky_nature_reserve_fire_(7938021666).jpg

[116] Tilo, Wikimedia Commons, "File:Waldbrand-Bodenfeuer.jpg," Uploaded on: Aug.

1, 2005, Accessed on: Oct. 1, 2017. [Online].

Available:https://commons.wikimedia.org/wiki/File:Waldbrand-Bodenfeuer.jpg

[117] E. Saltine, Wikimedia Commons, "File:Wildfire.jpg," Uploaded on: Oct. 30, 2003,

Accessed on: Oct. 1, 2017, [Online]. Available:

https://commons.wikimedia.org/wiki/File:Wildfire.jpg

[118] R. Keith, Wikimedia Commons, "File:A large fire in tropical forest trees in the

fire.jpg," Uploaded on: Mar. 1, 2013, Accessed on: Oct. 1, 2017, [Online]. Available:

https://commons.wikimedia.org/wiki/File:A_large_fire_in_tropical_forest_trees_in_t
he_fire.jpg

[119] G. Vicker, Wikimedia Commons, "File:Big fire burning big fire flames.jpg," U.S.
Fish and Wildlife Service, Uploaded on: Mar. 1, 2013, Accessed on: Oct. 1, 2017.
[Online]. Available:

https://commons.wikimedia.org/wiki/File:Big_fire_burning_big_fire_flames.jpg

[120] F. Schulke, Wikimedia Commons, "File:FOREST FIRE IN THE EVERGLADES,
COLLIER COUNTY. FIRES ARE FAIRLY COMMON IN THE EVERGLADES IN
DRY SEASONS OR DRY YEARS.... - NARA - 548591.jpg," U.S. National Archives
and Records Administration, Accessed on: Oct. 1, 2017. [Online]. Available:
https://commons.wikimedia.org/wiki/File:FOREST_FIRE_IN_THE_EVERGLADES,
_COLLIER_COUNTY._FIRES_ARE_FAIRLY_COMMON_IN_THE_EVERGLAD
ES_IN_DRY_SEASONS_OR_DRY_YEARS...._-_NARA_-_548591.jpg

[121] US Air Force, Wikimedia Commons, "File:High Park fire.jpg," Uploaded on: Aug.
4, 2014, Accessed on: Oct. 1, 2017. [Online]. Available:
https://commons.wikimedia.org/wiki/File:High_Park_fire.jpg

[122] T. Bulyonkova, Wikimedia Commons, "File:Yugansky nature reserve fire
(7938012202).jpg," Uploaded on: Aug. 19, 2013, Accessed on:
Oct. 1, 2017. [Online]. Available:
https://commons.wikimedia.org/wiki/File:Yugansky_nature_reserve_fire_(7938012202).jpg

[123] S. Eugster, Wikimedia Commons, "File:Cirrocumulus to Altocumulus.JPG,"
Uploaded on: Apr. 7, 2005, Accessed on: Oct. 1, 2017. [Online]. Available:
https://commons.wikimedia.org/wiki/File:Cirrocumulus_to_Altocumulus.JPG

[124] S. Eugster, Wikimedia Commons, "File:Big Cumulonimbus.JPG," Uploaded on: Sep. 10, 2015, Accessed on: Oct. 1, 2017. [Online]. Available: https://commons.wikimedia.org/wiki/File:Big_Cumulonimbus.JPG

[125] Joniprittie, Wikimedia Commons, "File:Brightbluesky.jpg," Uploaded on: Dec. 15, 2009, Accessed on: Oct. 1, 2017. [Online]. Available: https://commons.wikimedia.org/wiki/File:Brightbluesky.jpg

[126] L. Diosan, M. Oltean, A. Rogozan, and J.P. Pecuchet, "Genetically Designed Multiple-Kernels for Improving the SVM Performance," *In Proceedings of the 9th Annual Conference on Genetic and Evolutionary Computation (GECCO'07)*, London, UK, Jul. 2007, p. 1873.

[127] "Storm (HQ) Volcano Eruption (Vivaldi Techno) Vanessa Mae Violin Full HD Music Song Vídeo Remix 2013," Published on Apr. 7, 2013, Accessed on: Oct. 1, 2017. [Online]. Available: https://www.youtube.com/watch?v=lj6ZGGBy-R8

[128] "The Nuclear Cannon (Upshot-Knothole—Grable)," Published on Feb. 1, 2013, Accessed on: Oct. 1, 2017. [Online]. Available: https://www.youtube.com/watch?v=BECOQuQC0vQ

[129] "Texas Wildfires 2011 (Worst in TX History)," Uploaded on Sep. 7, 2011, Accessed on: Oct. 1, 2017. [Online]. Available: https://www.youtube.com/watch?v=pqr2DNaMLiQ

[130] "The Worst Neighbors from Hell Presents the Best Fireworks Display July 4th, 2016," Published on Jul. 4, 2016, Accessed on: Oct. 1, 2017. [Online]. Available: https://www.youtube.com/watch?v=6qO6TFUp5C0

[131] "Deep Blue Sky—Clouds Timelapse—Free Footage—Full HD 1080p," Published on Apr. 18, 2016, Accessed on: Oct. 1, 2017. [Online]. Available: https://www.youtube.com/watch?v=3pD88QLP1AM

[132] S. Piskorski, N. Brulez, P. Eline, and F. D'Haeyer, "Parrot AR.Drone Developer Guide," SDK 2.0, approved on Dec. 19, 2012.

[133] YADRONE, Accessed on: Oct. 1, 2017. [Online]. Available: https://vsis-www.informatik.uni-hamburg.de/oldServer/teaching//projects/yadrone/

[134] J. Cohen, "Statistical power analysis for the behavioral sciences," 2nd ed., Lawrence Erlbaum Associates, Inc., Hillsdale, NJ, USA, 1988.

[135] A. Ng, "CS294A Lecture notes–Sparse autoencoder," Stanford Univ., Stanford, CA, USA, Tech. Rep., pp. 1-19, 2011. Accessed on: Oct. 1, 2017. [Online]. Available: https://web.stanford.edu/class/cs294a/sparseAutoencoder_2011new.pdf

[136] A. Esteva, B. Kuprel, R.A. Novoa, J. Ko, S.M. Swetter, H.M. Blau, and S. Thrun, "Dermatologist-Level Classification of Skin Cancer with Deep Neural Networks," *In Nature 542*, pp. 115–118, Feb. 2, 2017.

[137] A. Krizhevsky, I. Sutskever, and G. E. Hinton, "ImageNet Classification with Deep Convolutional Neural Networks," *In Advances in Neural Information Processing Systems 25*, pp. 1106 —1114, 2012.

[138] Y. Liu, E. Racah, J. Correa, A. Khosrowshahi, D. Lavers, K. Kunkel, M. Wehner, and W. Collins, "Application of Deep Convolutional Neural Networks for Detecting Extreme Weather in Climate Datasets," 2016, arXiv:1605.01156.

[139] A. Conneau, H. Schwenk, L. Barrault, and Y. LeCun, "Very Deep Convolutional Networks for Text Classification," 2017, arXiv:1606.01781.

[140] C. Farabet, C. Couprie, L. Najman, and Y. LeCun, "Learning Hierarchical Features for Scene Labeling," *In IEEE Trans. Pattern Anal. Mach. Intell.*, vol. 35, no. 8, pp. 1915–1929, Oct. 2013.

[141] A. Graves, A. Mohamed, and G. Hinton, "Speech Recognition with Deep Recurrent Neural Networks," *In IEEE International Conference on Acoustics, Speech and Signal Processing*, pp. 6645 – 6649, May 2013.

[142] A. Karpathy, J. Johnson, and L. Fei-Fei, "Visualizing and Understanding Recurrent Networks," 2015, arXiv 2015, arXiv:1506.02078.

[143] A. ElSaid, B. Wild, F. El Jamiy, J. Higgins, and T. Desell, "Optimizing LSTM RNNs using ACO to predict turbine engine vibration," *In Proceedings of the Genetic and Evolutionary Computation Conference Companion (GECCO '17)*, Berlin, Germany, ACM 2017, pp. 21-22, Jul. 15-19, 2017.

[144] V. Pérez-Rosas, A. Narvaez, M. Burzo, and R. Mihalcea, "Thermal imaging for affect detection," *In Proceedings of the 6th International Conference on PErvasive Technologies Related to Assistive Environments (PETRA '13)*, Rhodes, Greece, ACM 2013, pp.1-4, May 29 - 31, 2013.